

2

APOSR-TR. 91 0565

Report F49620-86-C-0123

CENTER FOR THIN FILM STUDIES

AD-A237 457



Robert R. Shannon
Optical Sciences Center
University of Arizona
Tucson, Arizona 85721

DTIC
ELECTE
JUL 02 1991
S C D

AIR FORCE
SCIENTIFIC RESEARCH
PROGRAM
OFFICE OF
MANAGEMENT
AND
TECHNOLOGY
SERVICES
DISTRIBUTION STATEMENT
UNCLASSIFIED
15

22 January 1991

Final Report for the Period
1 October 1986 to 1 June 1990

APPROVED FOR PUBLIC RELEASE;
DISTRIBUTION UNLIMITED

Prepared for
AIR FORCE OFFICE OF SCIENTIFIC RESEARCH
University Research Initiative Program
Building 410
Bolling AFB, Washington, DC 20332-6448

ONRRR
Bandolier Hall West Rm. 223
University of New Mexico
Albuquerque, NM 87131

Accession For	
NTIS GRA&I	<input checked="" type="checkbox"/>
DTIC TAB	<input type="checkbox"/>
Unannounced	<input type="checkbox"/>
Justification	
By _____	
Distribution/	
Availability Codes	
Dist	Avail and/or Special
A-1	



91-03825



91 01 005

REPORT DOCUMENTATION PAGE				Form Approved OMB No. 0704-0188	
1a. REPORT SECURITY CLASSIFICATION UNCLASSIFIED		1b. RESTRICTIVE MARKINGS			
2a. SECURITY CLASSIFICATION AUTHORITY		3. DISTRIBUTION / AVAILABILITY OF REPORT Approved for public release; distribution unlimited.			
2b. DECLASSIFICATION / DOWNGRADING SCHEDULE					
4. PERFORMING ORGANIZATION REPORT NUMBER(S)		5. MONITORING ORGANIZATION REPORT NUMBER(S)			
6a. NAME OF PERFORMING ORGANIZATION Optical Sciences Center		6b. OFFICE SYMBOL (if applicable)	7a. NAME OF MONITORING ORGANIZATION ONRRR <i>Same as 8a</i>		
6c. ADDRESS (City, State, and ZIP Code) University of Arizona Tucson, Arizona 85721		7b. ADDRESS (City, State, and ZIP Code) <i>Same as 8c</i>			
8a. NAME OF FUNDING / SPONSORING ORGANIZATION USAF, AFSC		8b. OFFICE SYMBOL (if applicable) F08671 <i>NE</i>	9. PROCUREMENT INSTRUMENT IDENTIFICATION NUMBER F49620-86-C-0123		
8c. ADDRESS (City, State, and ZIP Code) Air Force Office of Scientific Research Building 410 Bolling AFB, Washington, DC 20332-6448		10. SOURCE OF FUNDING NUMBERS			
		PROGRAM ELEMENT NO. <i>101103D</i>	PROJECT NO. <i>3484</i>	TASK NO. <i>A3</i>	WORK UNIT ACCESSION NO.
11. TITLE (Include Security Classification) Center for Thin Film Studies (Unclassified)					
12. PERSONAL AUTHOR(S) Robert R. Shannon, Ursula J. Gibson, et al.					
13a. TYPE OF REPORT FINAL		13b. TIME COVERED FROM <i>10/1/86</i> TO <i>6/1/90</i>	14. DATE OF REPORT (Year, Month, Day) 1/22/91		15. PAGE COUNT 142
16. SUPPLEMENTARY NOTATION					
17. COSATI CODES			18. SUBJECT TERMS (Continue on reverse if necessary and identify by block number)		
FIELD	GROUP	SUB-GROUP			
19. ABSTRACT (Continue on reverse if necessary and identify by block number)					
<p>This report is for the entire term of operation of the URI Thin Film Center, including the six-month no-cost extension of the subject contract, and contains a summary of the research performed under this umbrella grant. Sections of this report address work on growth and characterization of thin films by various methods; modeling of thin film growth; and preparation and characterization of substrates for film growth.</p>					
20. DISTRIBUTION / AVAILABILITY OF ABSTRACT <input checked="" type="checkbox"/> UNCLASSIFIED/UNLIMITED <input type="checkbox"/> SAME AS RPT <input type="checkbox"/> DTIC USERS			21. ABSTRACT SECURITY CLASSIFICATION UNCLASSIFIED		
22a. NAME OF RESPONSIBLE INDIVIDUAL S. L. Singer <i>May P. Mrenke</i>			22b. TELEPHONE (Include Area Code) <i>202 767-4931</i>		22c. OFFICE SYMBOL <i>NE</i>

TABLE OF CONTENTS

INTRODUCTION	1
SUPPLEMENT TO THIRD ANNUAL REPORT	3
NUCLEATION AND GROWTH STUDIES	3
ION-ASSISTED DEPOSITION	4
ION-BEAM ANALYSIS OF THIN FILMS	5
FINAL REPORT	7
NUCLEATION AND GROWTH STUDIES	7
ION-ASSISTED DEPOSITION	13
STRUCTURE MODIFICATION BY ION-ASSISTED DEPOSITION (ION-BEAM ANALYSIS OF THIN FILMS)	17
A NOVEL TECHNIQUE FOR QUANTIFYING THE MECHANICAL PROPERTIES OF THIN FILMS	21
STUDIES OF SURFACE ROUGHNESS HEALING	27
CHARACTERIZATION FACILITY	31
MICRO SCANNING SCATTEROMETER AND POLISHING STUDIES	33
BIBLIOGRAPHY	35
SELECTED PUBLICATIONS AND PREPRINTS	
Appendix A	Nd:YAG Laser Ablation of BaTiO ₃ Thin Films
Appendix B	Optical and Microstructural Properties of Hafnium Dioxide Thin Films
Appendix C	Cross Sections for 170.5° Backscattering of ⁴ He from Oxygen for ⁴ He Energies Between 1.8 and 5.0 MeV
Appendix D	Non-Rutherford ⁴ He Cross Sections for Ion Beam Analysis
Appendix E	Preparation of YBaCuO Thin Films by Multilayer Deposition
Appendix F	Multilayer Mirrors for 182Å

INTRODUCTION

This report is divided into two sections: a supplement to the third annual report, giving specific information on work performed during the six-month no-cost extension, and a summary final report, providing an overview of work performed under this contract over the three and a half years since its inception.

The Center for Thin Film Studies covered a wide range of research topics, from fundamental studies of growth to applications of processing methods. Also developed were new and improved analysis tools, such as Brillouin spectroscopy, Rutherford backscattering spectrometry, microreflectometry, and surface probes such as scanning tunneling microscopy. Practical properties of interest such as scattering and absorptive losses, surface roughness, and optical properties for a variety of materials have also been reported. The attached summary highlights the important advances of the three-and-a-half-year effort; for further details, the reader is referred to the bibliography and the articles listed therein.

SUPPLEMENT TO THIRD ANNUAL REPORT

NUCLEATION AND GROWTH STUDIES

U. J. Gibson

During the extension of this contract, work continued in three areas: 1) preparation of Si substrates for ALE growth of ZnS; 2) the study of Si regrowth as a precursor to MBE growth of ZnS; and 3) the investigation of laser ablation of thin BaTiO₃ films.

H₂S treatment of Si wafers was shown to play an important role in the removal of residual oxygen impurities. This process improves the quality of the first layer, which is critical to the growth of high-quality ZnS. Even with a smooth first monolayer, however, the ALE process, using Zn and H₂S, does not promote smooth monolayer-by-monolayer growth, as was predicted. Films for which multiple exposures of Zn and H₂S were made exhibit oscillations in Zn coverage, and a clear evolution to the growth of islands (see Figs. 1 and 2).

We also investigated the regrowth of Si on Si wafers as a method of preparation for ZnS growth, and attained good reconstructed surfaces. Time, however, did not permit investigation of ZnS growth on these surfaces.

U. Gibson relocated to Dartmouth College in March of 1990, terminating experimental work under the aegis of this contract. Subsequently appearing publications are listed below.

PUBLICATIONS

J. K. Watanabe and U. J. Gibson, "Angle-Resolved X-Ray Photoelectron Spectroscopy Studies for Preparation Techniques for deposition of Atomic Layer Epitaxy ZnS on Si," accepted for publication in *J. Vac. Sci. Technol.* (1990).

B. Williams, "Study of the Growth and Nucleation of ZnS on Si(100)," Master's Report, University of Arizona (1990).

U. J. Gibson, J. A. Ruffner, J. J. McNally, and G. A. Peterson, "Nd:YAG Laser Ablation of BaTiO₃ Thin Films," *Materials Research Society Symposium Proceedings* (1990).

Supplement to Third Annual Report

ION-ASSISTED DEPOSITION

H. A. Macleod, B. G. Bovard, and M. R. Jacobson

Late in the contract period we investigated the post-deposition stress behavior of zirconia. Here, an increase in the temperature to 300°C, in air, produced large, irreversible changes in stress levels that seemed to arise from phase changes within the films. Ion-assisted deposition reduced the magnitude of the irreversible changes, although it did not eliminate those changes. Films fabricated by IAD also exhibited a slightly more complex pattern of behavior during that portion of the cycle over which the temperature rises. Although this was not the major focus of our investigation, it illustrated the significance of a film's crystalline microstructure in determining its mechanical properties. Work continues on this topic.

ION BEAM ANALYSIS OF THIN FILMS

J. A. Leavitt and L. C. McIntyre

Mr. Zhongtian Lin was supported on URI funds between October 1989 and June 1990. During this period he:

- participated in the analysis of films provided by Optical Sciences Center scientists and collaborators.
- wrote a computer program for the simulation of RBS spectra.
- wrote computer programs for calculating non-Rutherford elastic scattering cross sections for ^4He incident on ^{12}C and ^{16}O using semi-empirical dispersion theory; he included the effect of wide as well as of narrow resonances and compared the results with our C and O data.
- used ^4He and ^1H analysis beams to compare depth profiles of F and P in massive materials produced by (α, p) and (p, γ) nuclear reaction techniques.

Mr. Dezfouly-Arjomandy's salary was *not* paid by the Center during October 1989 through June 1990. His research on the development of the Penning Source and hydrogen depth profiling was supported by the Center (recall that Center funds were used to purchase a portion of the source assembly). An example of the hydrogen depth profiling technique using $^{15}\text{N}^{++}$ beams is shown in Fig. 1, with results of the analysis given in Table 1.

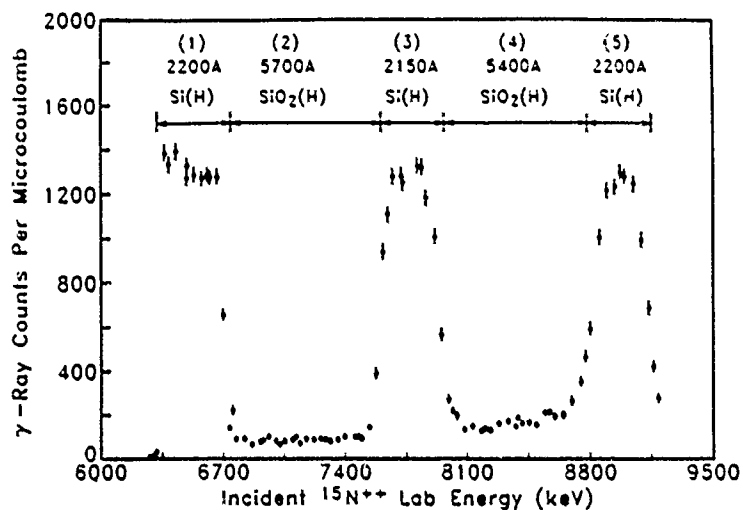


Figure 1. Nuclear reaction analysis data for depth profiling of hydrogen in a five-layer film consisting of alternate layers of hydrogenated Si and SiO₂. Approximate layer thicknesses are indicated. Results of the analysis of these data are given in Table 1.

Supplement to Third Annual Report

Table 1. Results of the Nuclear Reaction Analysis of Five-Layer Film

Layer	Element	*(Nt)	Atomic %
1	Si	1100 ± 120	73.3 ± 2.0
	H	400 ± 120	26.7 ± 2.0
2	Si	1250 ± 230	33
	O	2510 ± 450	66
	H	65 ± 9	1.7 ± 0.2
3	Si	1070 ± 120	73.6 ± 2.0
	H	384 ± 30	26.4 ± 2.0
4	Si	1190 ± 180	32
	O	2380 ± 360	64
	H	118 ± 12	3.2 ± 0.3
5	Si	1100 ± 120	73.9 ± 2.0
	H	390 ± 30	26.1 ± 2.0

*(Nt) = areal density in 10^{15} atoms/cm²

PUBLICATIONS

L. C. McIntyre, Jr., J. A. Leavitt, M. D. Ashbaugh, B. Dezfouly-Arjomandy, Z. Lin, J. Oder, R. F. C. Farrow, and S. S. Parkin, "Detection and Depth Profiling of ¹⁹F Using Resonances in the ¹⁹F(α ,p)²²Ne Reaction," accepted by Nucl. Sci. Tech. (China).

J. A. Leavitt and L. C. McIntyre, Jr., "Non-Rutherford ⁴He Cross Sections for Ion-Beam Analysis," Bull. Am. Phys. Soc. 35, 1695 (1990), submitted to Nucl. Instr. Meth.

FINAL REPORT

NUCLEATION AND GROWTH STUDIES

U. J. Gibson

OBJECTIVES

The primary goal of this task was to elucidate the growth mechanisms of thin films and to relate the nucleation process to film structure and roughness. Materials studied included ZnS, Ni, and BaTiO₃. Techniques used to study film structure included reflection high-energy electron diffraction (RHEED), x-ray photoelectron spectroscopy (XPS), waveguide loss measurements, second harmonic generation, scanning tunneling microscopy (STM), transmission and scanning electron microscopy (TEM and SEM), Rutherford backscattering spectroscopy, and x-ray diffraction. The materials chosen allowed us to examine a wide range of structural properties of thin films.

ACCOMPLISHMENTS

ZnS

We investigated zinc sulfide films produced by conventional thermal evaporation, molecular beam epitaxy (MBE), and atomic layer evaporation (ALE). The effects of background gases, ion bombardment, deposition temperature, and deposition method were studied. Important results included the following.

Reduction of waveguide losses from 25 dB/cm to less than 1 dB/cm, by reducing substrate temperature and minimizing film stress levels. As the substrate temperature was reduced, grain growth was quenched by -50°C, and the stress went through zero from compressive to tensile at that temperature. Waveguide losses reached a minimum at this point, then increased dramatically as the stress level rose in films deposited at colder temperatures.

Development of second harmonic generation as a technique for evaluation of anisotropy in thin films. In the case of a film with a completely homogeneous structure, second harmonic light should only be generated at the interfaces, where the symmetry of the film is broken by its termination. Real films are non-ideal, however, and include internal voids and columns that reduce the symmetry of the films and allow second harmonic generation. These structural imperfections, then can be studied by

characterizing the signal generated at 2ω by an intense laser pulse at ω . This characterization can be done non-destructively.

Column-induced anisotropy has been observed in Al_2O_3 films deposited with incidence angles as small as 3 degrees from normal by this technique, as compared with 30° angles normally required for anisotropy observation. We have applied the technique to investigations of columnar structure in ZnS. We found that reducing the substrate temperature to -50°C caused quenching of columnar growth (quenched columnar growth?). In addition, we were able to observe a large anisotropy induced by ion bombardment during growth with an ion incidence angle of 30° ; smaller-angle bombardment should be easily resolvable.

This technique is valuable for assessing the quality of thin films, and may also be useful for predicting coating failure at high laser frequencies. Since the second-harmonic light generated within the coating interacts more strongly with the absorbing defects, reduction of internal structure associated with SHG should be an important goal.

Columnar structure in Al_2O_3 and ZnS films has been measured using second harmonic generation of light. In ZnS, quenching of the columnar structure was observed as the substrate temperature was decreased. In addition, the texture induced by ion bombardment at a 30° angle of incidence during growth was observed. This technique should prove useful for evaluating coatings for high-energy laser applications, where second harmonic light generated by the laser-film interaction may give rise to absorbing defects, and to subsequent failure of the film.

Observation of three-dimensional (cluster) growth of films of ZnS produced by MBE. Cluster growth may be partially responsible for the high density of electronic defects in this material, because antisite defects are more likely to occur during 3-D growth. Structural defects were confirmed by Brillouin scattering (see the report by Stegeman).

Observation of the strong dependence of ALE ZnS growth on Si substrate preparation conditions. In particular, the improvement of initial layer growth with H_2S treatment of the substrate prior to deposition. With this treatment, initial layers grew layer by layer, as desired, but some subsequent cluster growth was observed in ALE growth from $\text{Zn} + \text{H}_2\text{S}$. H_2S treatment serves as a cleaning method, removing residual oxygen through an exchange reaction. Figure 1 shows the Zn:Si ratio as a function of electron takeoff angle in the x-ray photoelectron spectrometer. The data points accurately

follow the predicted curve for a smooth film one to two monolayers thick, with no evidence of patchy (three-dimensional) growth. After five cycles, as shown in Fig. 2, the data deviate from the theory, indicative of cluster-type growth of the films.

Ni

Thin layers of Ni were deposited onto highly oriented pyrolytic graphite (HOPG) for detailed studies of nucleation and of the development of surface roughness. Using a shadowing technique, we were able to study film nucleation and surface roughness as a function of thickness and arrival rate; other deposition parameters were kept identical. The diffusion energy of Ni on the HOPG surface was determined to be 0.127 eV. This is a relatively small value compared to other systems that have been studied, but the weak interplanar bonds in the graphite system give rise to a low interaction strength between Ni and the substrate. We studied thick deposits, using optical heterodyne interferometry and STM to determine surface roughness. STM, with its higher lateral resolution, yielded much higher values for RMS roughness, emphasizing the importance of matching the resolution of the probe to the corresponding scale of surface roughness. Figure 3 shows the surface roughness for Ni on SiO₂ as a function of temperature for a fixed deposition angle. The STM shows the predicted increase in roughness, whereas the interferometer does not. Related studies are presented in the report by Falco.

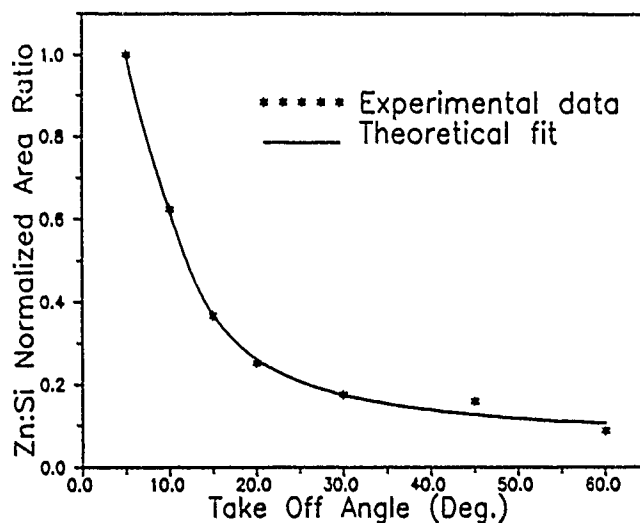


Figure 1. Zn:Si ratio as function of electron takeoff angle for ALE growth of ZnS on Si.

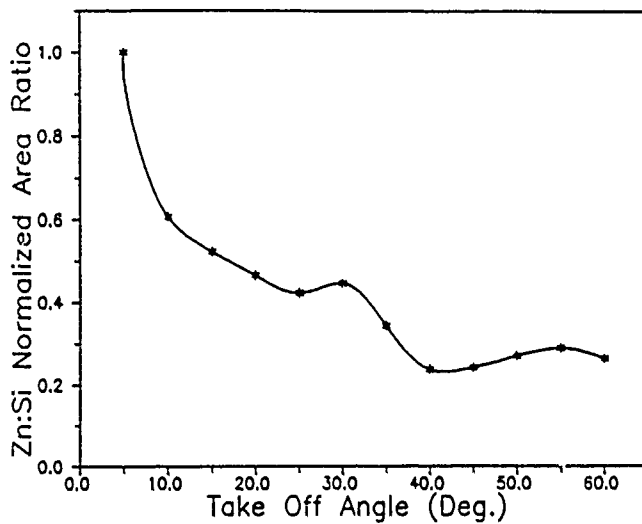


Figure 2. Zn:Si ratio after five cycles.

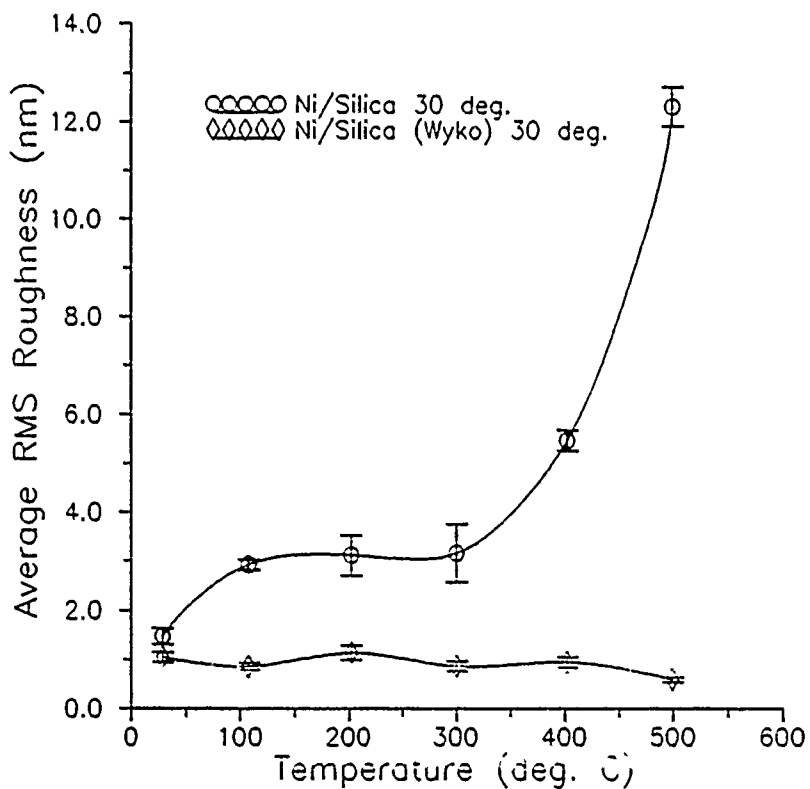


Figure 3. Temperature dependence of the roughness of nickel films on fused silica as measured with the Wyko interferometer and the STM, showing uncertainty.

BaTiO₃

U. Gibson worked half-time for a year at the F. J. Seiler Research Laboratory at the USAF Academy in Colorado Springs. There she initiated laser ablation of BaTiO₃ films. Because capabilities for analysis at the Academy were limited, personnel and facilities at the Thin Films Center were essential in the determination of the structure and chemistry of the deposited films. Picosecond and nanosecond pulses in the IR, VIS and UV were used to ablate films of BaTiO₃ onto Si, SiO₂ and MgO substrates. CO₂ heating of MgO substrates, and the use of UV nanosecond ablation pulses, permitted deposition of epitaxial BaTiO₃ films with smooth surfaces, suitable for signal processing experiments. This was the first report of epitaxial films with smooth surfaces to date.

Figure 4 shows the experimental arrangement for the deposition of the films, and x-ray diffraction analysis of a BaTiO₃ film deposited onto LiF. Only the (100) peak of BaTiO₃ appears, indicating epitaxial alignment of the film with the substrate.

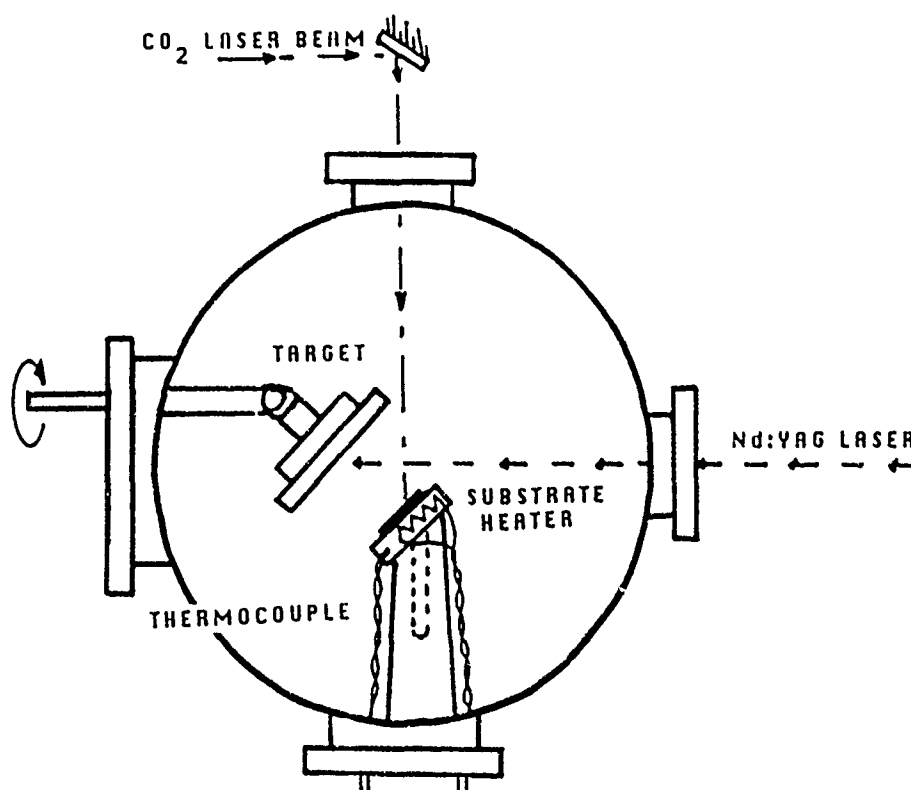


Figure 4a. Experimental arrangement for deposition of BaTiO₃ films by laser ablation.

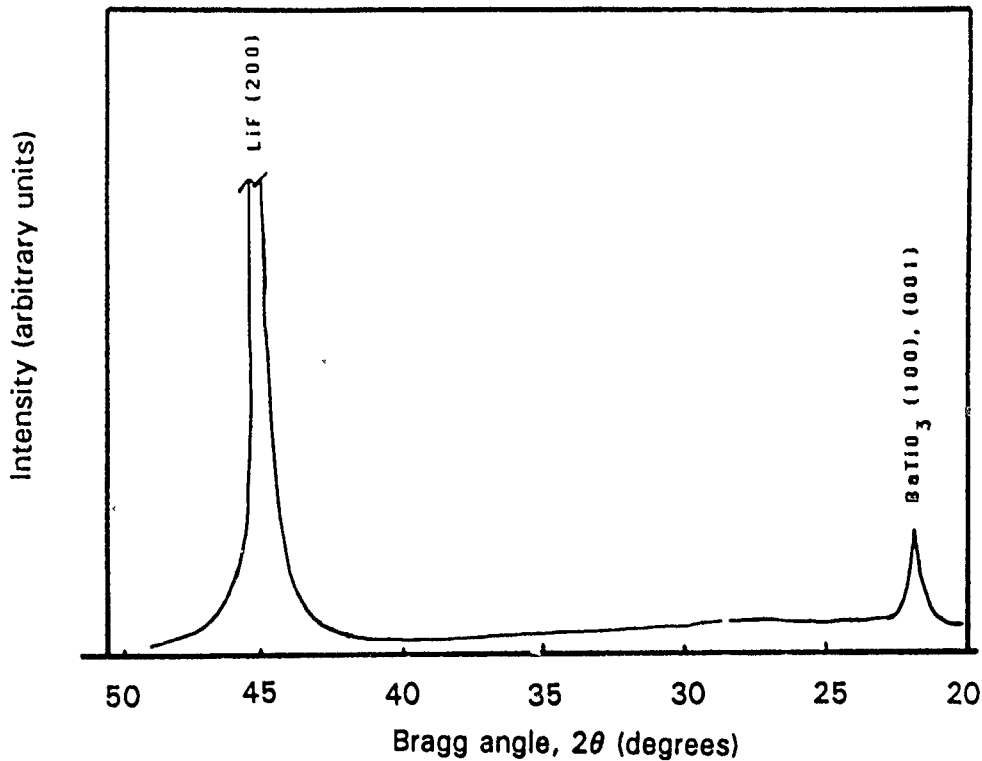


Figure 4b. X-ray diffraction of BaTiO₃/LiF.

PERSONNEL

U. J. Gibson
M. Himel
M. F. Kelley
J. K. Watanabe
B. Williams

DEGREE RECIPIENTS

M. F. Kelley, M.S., 1989, "Scanning Tunneling Microscope Characterization of Nickel Thin Film Nucleation and Growth."

B. Williams, M.S., 1990, "Study of the Growth and Nucleation of ZnS on Si(100)."

M. Himel, Ph.D., 1988 (partial support), "Microstructure Effects on Light Propagation in Zinc Sulfide Thin Film Waveguides."

J. K. Watanabe, Ph.D. anticipated in 1991, "Atomic Layer Epitaxy and Substrate Effects in ZnS/Si growth."

ION-ASSISTED DEPOSITION

H. A. Macleod, B. G. Bovard, and M. R. Jacobson

OBJECTIVES

The major objective of our research was to explore the use of ion-assisted deposition in the fabrication of thin films. Because the changes that ion-assisted deposition induces in thermally evaporated films were an important focus, for comparison we studied thin films deposited through conventional thermal evaporation in some detail.

ACCOMPLISHMENTS

Classic ion-assisted deposition is thermal evaporation coupled with ion bombardment of the growing film. Ion bombardment brings with it several largely beneficial effects. First, it increases the packing density of the film. Because many disappointing differences between the properties of bulk material and of thin films are attributed to low packing density, the increase in packing density attributed to ion bombardment is a promising aspect of the ion-assisted deposition process. A higher packing density (implies) greater resistance to mechanical disturbances such as abrasion. Second, the reactivity of the bombarding ions can be increased, leading to the production of useful materials that are virtually impossible to produce by conventional thermal evaporation. Third, the ion-bombardment process modifies a thin film's mechanical and chemical properties. A film's intrinsic stress is related to the degree of bombardment (tensile stress decreases continually, and compressive stress increases continually with increasing bombardment), so this process is unique in that it offers complete stress control. In addition, a film's chemical resistance is much improved.

To achieve the optimum effects of ion-assisted deposition, bombardment must take place during deposition, and the ion energy should be in excess of 50 eV. In most of our URI work, ion energies were several hundred electron volts.

Fluorides

Early in the contract we concentrated on the fluorides, in particular on magnesium fluoride. With magnesium fluoride bombardment must be by inert ions, because magnesium fluoride films are prone to decomposition. Fluorine is readily sputtered from the growing film, leaving vacancies that tend to be filled by oxygen. Small amounts of oxygen can be tolerated, but greater amounts lead to the formation of less durable and optically inferior oxyfluorides. It was necessary to control the bombardment process

closely but, provided the correct dose was used, films with bulk-like densities could be grown, with stoichiometries corresponding to conventionally deposited films. Baking at elevated temperatures caused a much more rapid exchange of fluorine for oxygen in conventional films than in the films fabricated by ion-assisted deposition. We then turned our attention to the fluorides of lanthanum and the lanthanides. This series is unique in its wide range of transparency, from the extreme ultraviolet through the far infrared. Little systematic study, however, has been performed on the series. These films exhibit very high intrinsic tensile stress. When these films are of any reasonable thickness, they are subject to tensile cracking, and this may have been a major barrier to their use in coatings. Because greater stress control (in particular the reduction of tensile stress) is possible with ion-assisted deposition, use of IAD to harness the advantages of the lanthanide fluorides was particularly attractive. We studied virtually the entire series in detail, and identified a number of new, potentially useful, film materials. We found that the films' extreme ultraviolet properties were improved with a small degree of bombardment. Tensile stress cracking was eliminated in thicker films for the infrared range. Our work on lanthanum fluoride confirmed that momentum transfer is the dominant process in the densification brought about by ion bombardment.

Our work also revealed a feature of thin films which seems curious at first glance: low substrate temperatures during deposition leads to a predominance of the high-temperature form of the film material, while higher substrate temperatures contribute to an increase in low-temperature phases. In fact, thin films are complicated mixtures of phases. Many of these phases are metastable high-temperature forms, and their transformation into more stable forms can be triggered by a disturbance such as an increase in temperature or mechanical shock. Even a modest increase in temperature can cause this transformation. Recent work in stress measurement reveal some of these effects. Observed changes contribute to a change in stress and strain energy, sometimes leading to film rupture.

Oxynitrides

The increased reactivity of the bombarding ions was integral to two areas of the study. In the deposition of refractory oxide materials by ion-assisted deposition, the usual loss of oxygen could be balanced by a supply of oxygen in the bombarding beam. Alumina and titania were investigated, as was zirconia later in the project. Many nitrides are attractive for use as optical materials. While they have

Ion-Assisted Deposition

good regions of transparency and are exceptionally rugged, however, nitrides are not good candidates for evaporative deposition. Nitrogen is not sufficiently active to permit the reactive evaporation process normally used for the deposition of oxides. Nitrides have not, therefore, been used much in conventional optical coatings. Ion-assisted deposition makes deposition of nitrides possible, through evaporation of the metal and bombardment with nitrogen ions. We concentrated on aluminum nitride, and demonstrated its usefulness in multilayers of aluminum nitride, oxynitride and oxide, all of which could be produced by evaporating aluminum under different bombardment conditions. Using nitrogen bombardment during deposition of aluminum in a slight background of oxygen, we were able to produce rugate structures. The only process variable was the degree of nitrogen bombardment during deposition. During the closing stages of the contract, we extended our investigation to boron nitride, which exhibits useful infrared transparency, with a pronounced narrow reststrahlen band in the far infrared. We successfully deposited and optically characterized this nitride, but microstructural characterization was no longer feasible.

Metals

Metals are important optical thin-film materials. Ion-assisted deposition of metals did not, however, prove to be as clearly beneficial as IAD of dielectric materials. Indeed, in general the films' optical properties were found to deteriorate slightly; the refractive index increased and the extinction coefficient of the metal decreased. These findings correlate well with the momentum transferred to the film from the bombarding ions. DC resistivity was affected in virtually the same manner as were the optical properties, and should be a useful characterization technique. The small changes in the optical constants of the metals were taken by a surface plasmon resonance technique. This technique was developed to such a high degree that it became our method of choice for the metals, even for those with high losses.

Detailed discussions of the topics addressed above are found in the dissertations prepared under this contract, as listed below.

PERSONNEL

H. A. Macleod
B. G. Bovard
M. R. Jacobson
C. K. Hwangbo
J. P. Lehan
L. J. Lingg
Y. Mao
D. Olinger
J. Targove

DEGREE RECIPIENTS

J. Targove, Ph.D., 1987, "The ion-assisted deposition of optical thin films."

C. K. Hwangbo, Ph.D., 1988, "Optical thin films by ion-assisted and ultrasound-assisted deposition."

J. P. Lehan, Ph.D., 1990, "Microstructural investigations of optical coatings by backscattering spectrometry, electron diffraction and spectrophotometry."

L. J. Lingg, Ph.D., 1990, "Lanthanide trifluoride thin films: structure, composition, and optical properties."

Y. Mao, Ph.D., 1990, "Environmental and thermomechanical stability of thin films for optical applications."

D. Olinger, Ph.D. expected in 1991, Dissertation on the subject of boron nitride.

STRUCTURE MODIFICATION BY ION-ASSISTED DEPOSITION (ION BEAM ANALYSIS OF THIN FILMS)

J. A. Leavitt and L. C. McIntyre, Jr.

OBJECTIVES

Our objectives were three-fold: 1) to characterize thin films by MeV ion beam analysis (IBA); 2) to improve existing IBS techniques and to develop new techniques; and 3) to expand the capabilities of the IBA facility itself.

ACCOMPLISHMENTS

We used $^4\text{He}^+$ analysis beams from a 5.5-MeV Van de Graff accelerator, with energies in the 1.5 MeV to 5.0 MeV range, to determine film thickness, stoichiometry, concentration profiles and crystalline structure by means of Rutherford backscattering, channeling and nuclear reaction analysis. We installed a new accelerator source to provide $^{15}\text{N}^{++}$ analysis beams with energies ranging from 6 MeV to 10 MeV for depth profiling hydrogen in thin films with the 6.385-MeV resonance in the nuclear reaction $^1\text{H}(^{15}\text{N}, \alpha\gamma)^{12}\text{C}$.

Film Characterization

Over the course of the project, we provided accurate characterization of thin films in support of studies of:

- ion-assisted modification of film structure
- MBE film deposition
- atomic layer deposition
- surface roughness.

We also provided film characterization in collaborative studies of high T_c superconducting films, x-ray mirrors, depth profiles of F in films, and heat treatment of In and Se films.

Technique Development

Efforts to improve characterization techniques included the following.

- accurate ($\pm 2\%$) detailed measurements of non-Rutherford cross sections for 170°

backscattering of ^4He by carbon and oxygen in the 1.5 MeV to 5.0 MeV range. We fitted these data with semi-empirical dispersion theory so that others may effectively use our measured results at backscattering angles other than 170° . The measured cross sections allow the use of higher-than-usual analysis beam energies, and reduce the overlap of signals from different elements, improving the accuracy of measured stoichiometry.

- development of hydrogen depth profiling techniques using:
 - elastic recoil detection (ERD) of protons "knocked on" at 30° from the direction of the incident ^4He beam for profiling ^1H with about 700\AA depth resolution.
 - the strong isolated resonance in the $^1\text{H}(^{15}\text{N},\alpha\gamma)^{12}\text{C}$ nuclear reaction cross section at $^{15}\text{N}^{++}$ beam energy of 6.385 MeV for profiling ^1H with about 100\AA near-surface depth resolution.
- development of techniques for depth profiling carbon and oxygen in more massive materials, using strong non-Rutherford resonances at 4.26 MeV and 3.05 MeV in the $^4\text{He}-^{12}\text{C}$ and $^4\text{He}-^{16}\text{O}$ elastic backscattering cross sections.
- development of techniques for depth profiling of fluorine and phosphorous in more massive materials using (α,p) and $(p,\alpha\gamma)$ nuclear reactions.
- development of reliable procedures for determining stoichiometry and measuring relative film thickness over large areas (3" wafers) with accuracies of better than $\pm 1/2\%$.
- use of heavier-than- ^4He analysis beams in an attempt to improve the mass and depth resolution provided by ^4He backscattering spectrometry. We concluded that use of the heavier beams provided no significant improvement if a silicon surface barrier detector is used.

Facility Development

The most significant facility improvement was the replacement of the rf ion source in the 5.5-MeV Van de Graff terminal with a Penning source assembly. The new source provides stable $^{15}\text{N}^{++}$ beams for depth profiling of hydrogen, as well as $^4\text{He}^+$ beams for backscattering analysis and $^1\text{H}^+$ beams for particle-induced x-ray (PIXE) analysis. The new source has operated for periods of more than 500 hours without maintenance.

PERSONNEL

J. A. Leavitt
L. C. McIntyre
M. D. Ashbaugh
J. G. Oder
Z. Lin
B. Dezfoley-Arjomandy

DEGREE RECIPIENTS

J. G. Oder, M.S., 1989.

B. Dezfoley-Arjomandy, Ph.D., 1990, "Hydrogen Depth Profiling Using the 6.385 MeV Resonance in the $^1\text{H}(^{15}\text{N},\alpha\gamma)^{12}\text{C}$ Nuclear Reaction."

Leavitt

A NOVEL TECHNIQUE FOR QUANTIFYING THE MECHANICAL PROPERTIES OF THIN FILMS

G. I. Stegeman

OBJECTIVES

Our initial objective was to develop Brillouin scattering as a technique for measuring the elastic properties of thin films and interfaces. Later, we investigated second harmonic generation (SHG) as a tool for characterizing thin films. Our research into SHG was supported primarily through other sources.

ACCOMPLISHMENTS

We studied ZnS samples, including their Brillouin spectra, and characterized them by SHG. We also studied Langmuir-Blodgett (LB) films in some detail. The study of rough surfaces was also undertaken. Finally, we examined conducting ionic materials to study the effects of conducting ions on elastic properties.

Brillouin Scattering From ZnS Films

ZnS films were examined, and it was found experimentally that the presence of a Rayleigh wave could not be detected by light scattering in a sample with microcracks. The Rayleigh mode, as expected, was heavily damped by rough surfaces. Brillouin scattering measurements were also performed on samples of ZnS films on Si substrates, to examine the effects of different buffer layers between the substrate and film. Phonon dispersion curves were calculated for both an isotropic ZnS film on a Si substrate, and for an isotropic ZnS film separated from the Si substrate by an isotropic SiO₂ film. The calculated curves did not reveal any changes within the resolution of the Brillouin spectroscopy technique. This finding was confirmed by experimental data taken for three samples, each with its substrate cleaned by a different method. The cleaning method used did not have any observable effect on the acoustic phonon spectrum.

Brillouin Scattering From Gratings on Si Substrates

As a first step in understanding the effects of surface roughness on the mechanical properties of thin films and surfaces, we investigated Brillouin scattering of acoustic phonons on gratings etched in Si. Measurements of the velocities of sound on its surface yield a film's elastic constants. While sample characterization revealed evidence of gratings, we observed only the Rayleigh mode that corresponds to

a bare Si surface. This observation contradicted preliminary findings, which indicated splitting of acoustic modes, zone boundaries, and other evidence of gratings. On further investigation we discovered that residues of photoresist material on the gratings melted when incident light was focused onto them. The slight shifts observed in the Rayleigh-mode velocity may not, therefore, have been meaningful. It appears we were melting the surface of the silicon, eliminating the gratings under investigation.

We improved our techniques for collecting Brillouin scattered light. With the circular aperture we used initially, the scattering wave vector was spread significantly, causing the Brillouin peaks to become broader, particularly at low angles of incidence. We solved this problem by passing the scattered light through a rectangular slit prior to analysis with a Fabry-Perot interferometer. This method yielded Rayleigh wave velocities that are in excellent agreement with theory.

Brillouin Scattering From Langmuir-Blodgett Films

In one series of experiments, we investigated the dependence of the elastic properties of L-B films on the conditions of the water surface in the Langmuir trough. Films of 22-tricosenoic acid (developed as a high-resolution photoresist material) were prepared with increasing water surface pressures, and their Brillouin spectra were measured. The Rayleigh wave and first Sezawa mode velocities increased with increasing surface pressure, indicating a corresponding increase in the shear elastic constant. Brillouin spectra also revealed in-plane asymmetry in the elastic constants. Detailed analysis of the data for one surface pressure yielded the film elastic constants.

A second series of experiments was carried out on films of GD10 L-B molecules. Using Brillouin spectroscopy to probe the phonon modes in the a-c and a-b planes, and to identify spectra attributable to longitudinal guided waves, the *complete* set of elastic constants was determined for a L-B film for the first time. As observed for 22-tricosenoic acid, the ratio of the shear to the longitudinal elastic constants was approximately 1:10.

We continued our experiments on artificial multilayered films, in particular on polymeric uniaxial LB films that are multilayer assemblies of preformed polymers. These new LB materials have attracted considerable interest because they possess improved thermal and mechanical stability. In researching ways to overcome the fragile nature of LB films, we performed Brillouin scattering experiments on ODF/ODM LB films. These experiments showed that, upon polymerization, the LB films can be hardened unless microcracks form.

A Novel Technique

Another way to overcome the fragile nature of LB materials is to deposit preformed polymers directly onto substrates. We studied this approach during the past year. Polyglutamates with long alkyl side chains were employed in this project. Molecules were found to orient parallel to the dipping direction during transfer to the Mo substrate, and the resulting film was found to have hexagonal symmetry with the c-axis parallel to the surface. This geometry enabled us to obtain more information about the LB materials than we could before. Previously, molecules of the LB materials were aligned perpendicular to the surface, yielding films with hexagonal structures, with the c-axis normal to the surface.

An interesting feature of the Brillouin spectra obtained from a series of samples with different numbers of monolayers is the existence of a longitudinal guided acoustic phonon mode, in addition to the usual Rayleigh and Sezawa modes. Furthermore, a resonant enhancement of the scattering cross section for some Sezawa modes, arising from an additional bulk coupling mechanism of the scattered light to the film modes, was observed and verified by computer simulation. By probing the acoustic phonons travelling parallel and perpendicular to the dipping direction, the complete set of elastic constants, as well as the refractive indices, were determined for the first time. This set of elastic constants accounted for all Brillouin spectra for all samples up to 10000 Å thick. In addition, the elastic constants are stable, even in lieu of special storage conditions, indicate that the mechanical stability of the films is very good.

To deduce the elastic constants for one set of polyglutamate LB films, two additional series of samples were investigated. Each series has side chains with different lengths, with the length of the rod-like backbone kept constant. Hence, each series of films has a different bilayer thickness. We found that the longitudinal elastic constants increase by more than 10% as the bilayer thickness decreases by 6%. This is the first time such correlations have been possible.

Double-Enhanced Surface Brillouin Scattering

We performed surface Brillouin scattering measurements on eighteen monolayers of cadmium arachidate (CdA) LB films deposited on a silver film. By using the Kretschmann ATR geometry, the incident light can couple into the surface plasmons, allowing us to dramatically enhance the cross section of scattered light from the surface acoustic waves. If the Brillouin scattered light is also coupled into surface plasmons, this enhancement is even more dramatic.

With appropriate powers for the incident light, we have observed a maximum in the cross section of the Brillouin signals when the ATR reflectivity reaches the minimum, corresponding to the surface

plasmon resonance condition. When the angle of incidence is tuned to the resonance condition, the electromagnetic field at the surface of the metal film can be orders of magnitude greater than that of the incident light. Unless care is taken, the dielectric layer on the metal film can melt.

In such a Brillouin spectrum, two signals are observed. One signal corresponds to scattering from the Rayleigh wave travelling along the silver film, which is renormalized because of a dielectric layer of eight layers of CdA LB films. The other signal corresponds to scattering from one of the Sezawa waves. By performing theoretical calculations of the mode profiles of possible surface and film guided modes, we could identify this Sezawa mode as the third Sezawa wave of the LB film-Ag film system. That the first two Sezawa modes were not observed in this scattering geometry indicates that the surface plasmons couple effectively only to the acoustic surface modes whose energy is localized at the interface between the metal film and another dielectric layer.

Brillouin Scattering Studies on " β "-alumina

" β "-alumina has a layered structure, and various ions can be inserted into the *conduction* planes between layers. Because these highly mobile ions give rise to significant conductivity, there has been great interest in this material for use as a solid electrolyte in batteries, as well as for use in optical devices. Because the distance between the layers is a function of the ions present in the planes, it is expected that the elastic properties of the crystal, which reflect the local interatomic forces, will change if different ions are used. Although this problem did not fit neatly within the scope of this contract, it represented an interesting opportunity, especially since the samples were provided by another group.

From the Brillouin spectra, with three peaks attributable to scattering from one longitudinal and two transverse bulk phonons, the elastic constants were determined for samples with Na⁺ and with K⁺ ions.

We developed computer programs to fit all elements of the elastic constant tensor for arbitrary crystal symmetry and arbitrary crystal direction. Until now, it was necessary to have a high symmetry direction in the sample plane. Using these programs, we have determined the complete set of elastic constants for this trigonal ($\bar{r}3m$) crystal, one of the lowest symmetry crystal systems studied to date by Brillouin spectroscopy.

The principle result was the following. By exchanging the Na⁺ ions for K⁺ ions, the elastic constants c_{33} increased by 16%, and the other elastic constant showed a slight increase, reflecting the increase in the size of the conducting ions.

SHG Investigations of Thin Films

Second harmonic generation was used as a diagnostic tool for assessing the structure of ZnS thin films. In particular, the SHG signal is sensitive to the existence of columnar microstructure and crystallinity in the film. The SHG results on ZnS showed that cooling the substrate during deposition substantially reduces the formation of columns and crystallites in the film.

We continued our investigation into the microstructure of LB monolayer films using SHG. This is a collaborative project with W. Knoll at the Max Planck Institute for Polymer Research.

We demonstrated that SHG could be an effective means of studying the influence of the precise deposition technique on the resulting film microstructure. This work was carried out with an aggregate-forming cyanine dye, referred to as S120. The elliptical aggregates were shown to partly orient during the isothermal compression phase of the deposition. Furthermore, it was possible to deduce the crystal structure of the aggregates with SHG.

In a continuation of this work, it was shown that an S120-Arachidic acid mixture, which produces rounder aggregates, leads to an increase in the isotropy of the SHG signal, as one would expect based on our analysis. Conversely, we have been working on a technique for totally orienting the aggregates by first depositing them on crystalline gypsum [H. Kuhn, *Pure and App. Chem.* **53** 2105, (1981)], to facilitate further study. This difficult process is still under development in our laboratory. An important step in achieving this goal, and for the studies of monolayer films in general, has been the successful development of a means of obtaining light microscope photographs of the actual aggregate structures, using Nomarski optics. We have also been sent a variant of the S120 by Kodak for comparative study.

With a more device-oriented focus, we have obtained and studied material from Dr. I. Ledoux's group at CNET in France. This group has been studying organic Azo dyes, as these are a class of materials that hold promise for $\chi^{(2)}$ -based applications, and which are most conveniently studied in LB form. While the CNET group has the facilities to measure the $\chi^{(2)}$ of a LB film using SHG, they lack the technique for interpreting their results in terms of film microstructure. Their published data [I. Ledoux, et al., *Europhysics Letters* **3**, 803 (1987)] had suggested some anomalous behavior, which they were willing to have us try to resolve. After depositing and studying (with SHG) some of the material they provided, it became clear that the problem was that of difficulty in obtaining a suitable film microstructure. Here, then, SHG was used not only to determine a material's nonlinear response for device purposes, but also to screen for suitability in a pure materials fabrication sense.

PERSONNEL

G. I. Stegeman
J. A. Bell
J. R. Dutcher
B. Hillebrands
S. M. Lee
G. McLaughlin
F. Nizzoli
R. Zanoni

STUDIES OF SURFACE ROUGHNESS HEALING

C. M. Falco

OBJECTIVES

Our goal was to develop techniques for determining, and reducing, the roughness of substrate surfaces. Scanning tunneling microscopy (STM), optical interferometry and other techniques were developed to study the roughness of surfaces on scales from angstroms to millimeters. In combination with these studies, sputtering and molecular beam epitaxy (MBE) techniques were developed to deposit buffer layers as a means to reduce surface roughness.

ACCOMPLISHMENTS

We improved our ability to characterize films and substrates using the Nanoscope-II scanning tunneling microscope. Several substrate materials, of interest for electronics and optics applications, were characterized. We also characterized thin-film surfaces to study the relationship between substrate roughness and interface roughness. Optical interferometry, reflection high-energy electron diffraction (RHEED), and low-energy electron diffraction (LEED) were used to determine surface roughness. Various techniques for reducing roughness were developed and tested.

Substrate Preparation

We deposited Si films by sputtering on a variety of substrates, and characterized surface roughness using techniques described below. The substrates studied to date include diamond-turned aluminum, float glass, and polished, semiconductor-grade Si wafers. These substrate materials are important for future thin-film work in visible and XUV optics, electronics, and magnetism.

Substrate surfaces were characterized with a scanning tunneling microscope and a WYKO phase-shifting interferometer, both before and after deposition of Si films by sputtering. The STM and the WYKO interferometer have comparable vertical resolutions: 1 Å for the STM, and 3 Å for the interferometer. However, the devices' horizontal resolutions differ by a factor of 10^4 . Horizontal resolution for the STM is ≈ 1 Å; for the interferometer it is ≈ 2 μm. The WYKO interferometer measurement determines the "waviness" of the surface, while the STM, with its atomic resolution, measures roughness within dimensions that have significant effects on the physical properties of many thin films and multilayers.

STM surface profiles of a diamond-turned aluminum flat revealed a small periodic ripple in the surface before deposition. This ripple was presumed to be an artifact of the diamond turning process. Measurements of the auto-correlation function of the surface after deposition of the buffer layer showed the surface to be much more random. Analysis of many such measurements leads us to conclude that the Si buffer layer succeeds in randomizing the surface, but has little effect on the root-mean-square (RMS) roughness. For the polished Si and float glass substrates, the deposition of a Si buffer layer improved neither the RMS roughness nor the randomness of the surface.

Si wafers and float glass were treated with three commonly used cleaning procedures to determine their effects on roughness. Simple detergent cleaning, a three-step acid cleaning procedure and a twenty-two-step acid cleaning procedure were used to prepare Si wafers for growth of films by molecular beam epitaxy (MBE). Interferometer measurements were performed on the substrates before and after the cleaning procedures. The three-step acid etch was found to leave a clean but otherwise unmodified surface. The detergent method left rough patches, while the twenty-two-step acid cleaning procedure increased the roughness of the polished wafers over the entire area sampled.

We concentrated our MBE effort on Si used as a spacer and substrate material. Using *in situ* RHEED and LEED, we studied the deposition of buffer layers of Si onto polished, semiconductor-grade Si wafers. We found a dramatic improvement in the surface roughness and surface crystal structure with the deposition of as little as 10 Å of Si at a substrate temperature of 800°C. This improvement is particularly noticeable in the RHEED pattern, which reveals a decrease in background and an improvement in the spot pattern. The final spot pattern is characteristic of a surface which is absolutely flat except for atomic steps separated by several hundred angstroms. To obtain the most perfect substrate surface possible, the deposition of a 100-Å Si buffer layer at 800°C has become our standard substrate pretreatment for all samples.

Epitaxial Molybdenum Disilicide

Several metal silicides have a reasonably close lattice match with silicon, and therefore are potential materials for epitaxial growth. Because they are good conductors, metal silicides show potential for use as gates and contacts in integrated circuits. Their optical constants in the soft x-ray region makes them potential candidates for use as absorber layers in multilayer x-ray reflectors. In each of these applications

it would be most advantageous to be able to produce smooth, epitaxial, single-crystal layers of the silicides.

MoSi₂ films were prepared by simple codeposition of Mo and Si onto a heated Si (111) substrate in the MBE system. X-ray diffraction and STM characterization showed that a film codeposited at 600°C was composed of epitaxial islands, ranging from 500 nm to 1000 nm across, with heights of tens of nanometers, and with fine polycrystalline grains. Films codeposited at lower temperatures were much smoother, but lacked the epitaxial component. We conclude that MoSi₂ epitaxy on Si (111) has been achieved, but this particular technique leads to island formation and, therefore, to rough films. These results led us to investigate the template growth technique.

Templates are thin layers of silicide, 3 Å to 10 Å thick, grown by MBE on single-crystal Si substrates. The template is formed by depositing the Mo at near room temperature, then heating to induce a solid-state reaction. The template becomes the substrate on which the rest of the structure is grown. LEED, performed in the MBE system, shows that the MoSi₂ templates formed on Si (111) at 500°C to 600 °C are epitaxial, but somewhat disordered. STM scans of silicide layers grown on these templates show a series of parallel depressions, which may be grain boundaries that form to relieve the strain associated with the lattice mismatch between the Si substrate and the template. Thin layers (< 10 Å) of good quality MoSi₂ were formed using the template technique. The growth of thicker layers of the same quality, however, proved impossible.

Roughness of Multilayer Films

STM characterization of two x-ray mirrors revealed the surface roughness over a range of horizontal scales covering more than three orders of magnitude. The Mo/Si multilayer mirrors were grown in the MBE system on single-crystal Si substrates. The only difference in the fabrication of the two mirrors was the substrate temperature: one was produced at 40°C and the other at 200°C. For both samples, the roughness varied from 1(±0.3) Å for the smallest area, 10 Å on a side, to a saturation value of 7(±0.3) Å for squares larger than 800 Å on a side. One interpretation of this behavior is as follows. When the scan size is much greater than the crystallite size, the roughness is calculated over grain boundaries and facets. When the scan size is much smaller than the crystallites, however, most of the samples are taken on a single-crystal surface, yielding an atomic rms roughness. That both samples have the same top-

.. surface roughness implies that differences in the performance of these mirrors is related to interdiffusion and reaction at the interfaces rather than to the scale of roughness measured by the STM. We have also obtained cross-sectional images of multilayers that show the periodic modulation of the layering.

PERSONNEL

C. M. Falco
M. K. Burkland
J. M. Slaughter

CHARACTERIZATION FACILITY

U. J. Gibson

PROJECT STATUS

Over the three-year period of the contract, a state-of-the-art microscopy and specimen preparation center was established. Facilities included:

JEOL 2000FX TEM/STEM with video camera

JEOL 5200 SEM with backscatter detector and high resolution CRT

Olympus Nomarski microscope with video camera system

ion thinner with liquid nitrogen cooled stage

sputter coater

dimpler

coring drill

miscellaneous sample preparation equipment

WYKO heterodyne interferometer surface profiler (on loan from U.S.A.F.)

This equipment was maintained and staffed from the central budget of the URI. At the conclusion of the three-year contract, the equipment was transferred to the Arizona Research Laboratories, where it continues to support thin-films research.

Gibson

MICRO SCANNING SCATTEROMETER AND POLISHING STUDIES

W. L. Wolfe

The scanning microreflectometer, illustrated in Fig. 1, was moved into W. L. Wolfe's laboratory after completion of developmental work. Dr. Wolfe's group was available to take measurements, and maintained the instrument. The instrument was used to obtain data on samples provided by K. Stowell, Air Force Weapons Lab, Kirtland Air Force Base, New Mexico.

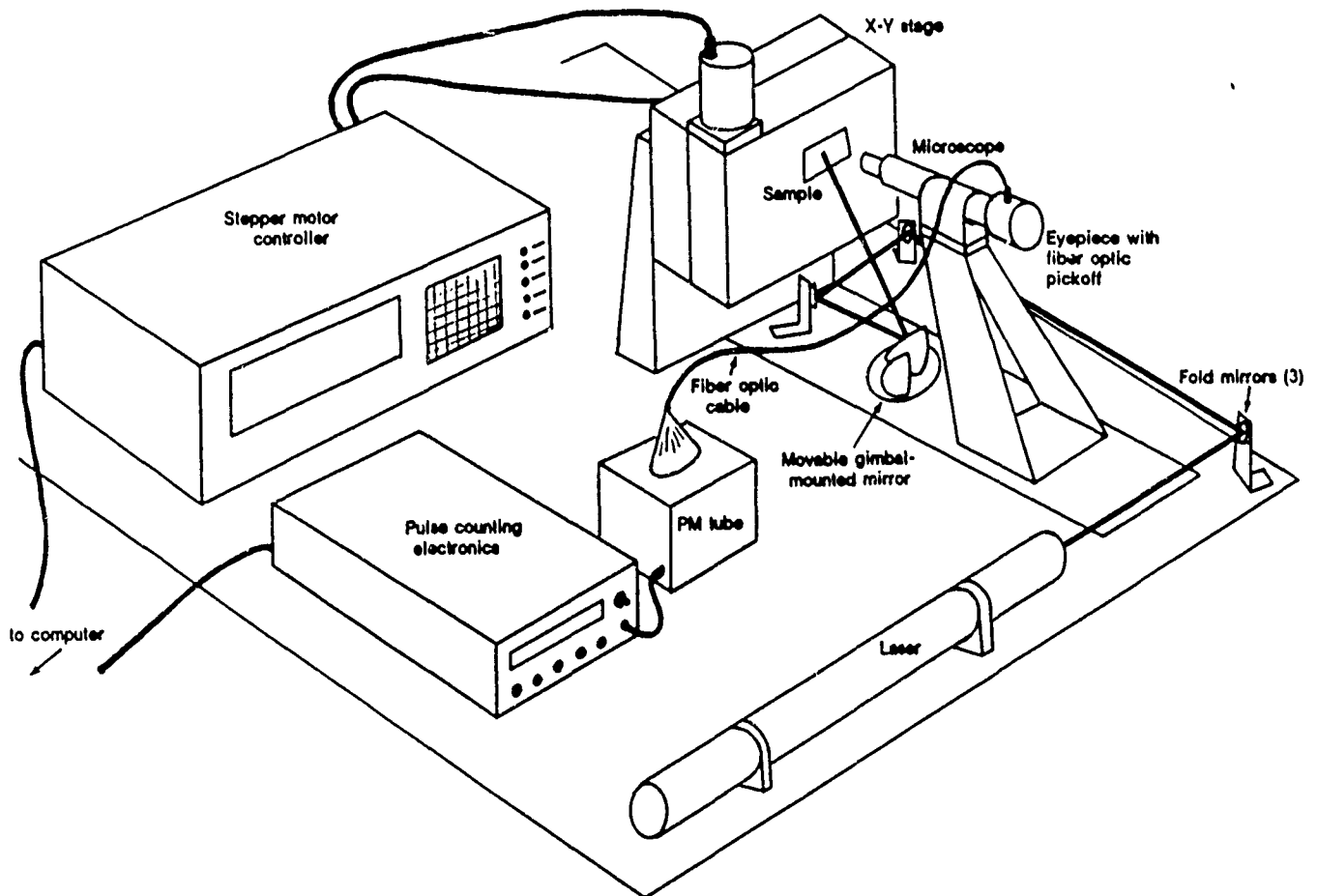


Figure 1. Scanning microreflectometer.

PERSONNEL

W. L. Wolfe
D. Eklund
G. Videen
R. E. Parks

BIBLIOGRAPHY

The following publications and presentations, listed by Principal Investigator, represent work supported under the Center for Thin Film Studies/University Research Initiative Program.

U. J. GIBSON

Publications

- U. Gibson, Optical Sciences Center, University of Arizona, Tucson, AZ 85721, "Center for Thin Film Studies," Annual Report, October 1987. Project Task: URI; Program Manager: Kevin J. Malloy.
- V. Mizrahi, F. Suits, J. E. Sipe, U. J. Gibson, and G. I. Stegeman, "New probe of thin-film microstructure," *Appl. Phys. Lett.* **51**(6), (1987).
- U. Gibson, Optical Sciences Center, University of Arizona, Tucson, AZ 85721, "Center for Thin Film Studies," Annual Report, October 1988. Project Task: URI; Program Manager: Cole Litton.
- M. D. Himel, J. A. Ruffner, and U. J. Gibson, "Stress modification and reduced waveguide losses in ZnS thin films," *Appl. Opt.* **27**, 2810 (1988).
- M. D. Himel, J. A. Ruffner, and U. J. Gibson, "Microstructure effects on light propagation in ZnS waveguides," in *Optical Interference Coatings*, 1988 Technical Digest Series, Vol. 6, p. 32 (Optical Society of America, Washington DC, 1988).
- F. Suits and U. J. Gibson, "Optical response of a composite medium consisting of metal particles in a nonlinear dielectric host," in *Optical Interference Coatings*, 1988 Technical Digest Series, Vol. 6, p. 32 (Optical Society of America, Washington DC, 1988).
- F. Suits and U. J. Gibson, "Optical response of a composite medium consisting of metal particles in a nonlinear dielectric host," *J. Opt. Soc. B* (1989).
- M. F. Kelley, Scanning tunneling microscope characterization of nickel thin film nucleation and growth," MS thesis, University of Arizona, 1989.
- Z. Milanovic, M. A. Voelker, M. F. Kelley, K. O. Powers, and C. M. Falco, "Surface roughness healing of substrates for XUV multilayer coating," *Proc. SPIE*.
- G. I. Stegeman, J. A. Bell, W. R. Bennett, G. Duda, C. M. Falco, U. J. Gibson, B. Hillebrands, W. Knoll, L. A. Laxhuber, S. Lee, J. Makous, F. Nizzoli, C. T. Seaton, J. D. Sweten, G. Wegner, and R. Zanoni, "Brillouin scattering from thin films," *Proc. Workshop on Scattering of Electromagnetic Radiation*, in press.
- J. A. Ruffner, M. D. Himel, V. Mizrahi, G. I. Stegeman, and U. J. Gibson, "Effects of low temperature and ion-assisted deposition on composition, optical properties and stress of ZnS thin films," *Appl. Opt.* 1989.

Presentations

- J. K. Watanabe, A. J. Stentz, and U. J. Gibson, "XPS and RHEED studies of preparation of silicon for ZnS growth," AUS Meeting.
- J. K. Watanabe, A. J. Stentz, and U. J. Gibson, "XPS studies of preparation of silicon for ZnS growth," presented at the 10th Symposium on Applied Surface Analysis, Denver, 1988.
- J. K. Watanabe and U. J. Gibson, "Preparation studies of Si(100) for growth of atomic layer epitaxy ZnS," presented at the 36th National Symposium of the American Vacuum Society, Boston, 1989.

H. A. MACLEOD AND B. G. BOVARD

- J. D. Targove, L. J. Lingg, J. P. Lehan, C. K. Hwangbo, H. A. Macleod, J. A. Leavitt, and L. C. McIntyre, Jr., "Preparation of aluminum nitride and oxynitride thin films by ion-assisted deposition," MRS Symposia Proceedings 93, 311 (1987).
- B. G. Bovard, "Fourier transform technique applied to quarterwave optical coatings," *Appl. Opt.* 27, 3062 (1988).
- C. K. Hwangbo, L. J. Lingg, J. P. Lehan, M. R. Jacobson, H. A. Macleod, J. L. Makous, and S. Y. Kim, "Ion-assisted deposition on the crystallinity of samarium fluoride films," in *Optical Interference Coatings*, 1988 Technical Digest Series, Vol. 6, p. 32 (Optical Society of America, Washington DC, 1988).
- L. G. Lingg, C. K. Hwangbo, B. G. Bovard, J. P. Lehan, and H. A. Macleod, "Effect of Ion-assisted deposition on the crystallinity of samarium fluoride films," in *Optical Interference Coatings*, 1988 Technical Digest Series, Vol. 6, p. 32 (Optical Society of America, Washington DC, 1988).
- J. D. Targove, L. J. Lingg, J. P. Lehan, and H. A. Macleod, "Effect of oxygen incorporation on the structure of ion beam-assisted LaF₃ thin films," in *Optical Interference Coatings*, 1988 Technical Digest Series, Vol. 6, p. 32 (Optical Society of America, Washington DC, 1988).
- J. D. Targove, L. J. Lingg, J. P. Lehan, and H. A. Macleod, "The effect of oxygen incorporation on the structure of metal fluoride thin films," in *Optical Interference Coatings*, 1988 Technical Digest Series, Vol. 6, p. 32 (Optical Society of America, Washington DC, 1988).
- J. D. Targove, L. J. Lingg, and H. A. Macleod, "Verification of momentum transfer as the dominant densifying mechanism in ion-assisted deposition," in *Optical Interference Coatings*, 1988 Technical Digest Series, Vol. 6, p. 32 (Optical Society of America, Washington DC, 1988).
- J. D. Targove, L. J. Lingg, J. P. Lehan, and H. A. Macleod, "Effect of oxygen incorporation on the structure of ion-beam-assisted LaF₃ thin films," *Appl. Opt.* 27, 213-215 (1988).
- B. G. Bovard and H. A. Macleod, "Thermal model of a switching Fabry-Perot etalon," *Proc. SPIE* 821 187-197 (1988).

- R. B. Sargent and H. A. Macleod, "Computer simulation of the growth of two-element films," Proc. SPIE 821, 113-119 (1988).
- R. B. Sargent, D.-Y. Song, and H. A. Macleod, "Computer simulation of substrate defect propagation in thin films," Proc. SPIE 821, 133-140 (1988).
- J. D. Targove, B. G. Bovard, L. J. Lingg, and H. A. Macleod, "Densification of aluminum fluoride thin films by ion-assisted deposition," Thin Solid Films 159, L57-L59 (1988).
- B. G. Bovard and H. A. Macleod, "Nonlinear behavior of optical coatings subjected to intense laser irradiation," J. Mod. Opt. 35, 1151-1168 (1988).
- J. D. Targove and H. A. Macleod, "Verification of momentum transfer as the dominant densifying mechanism in ion-assisted deposition," Appl. Opt. 27, 3779-3781 (1988).
- C. K. Hwangbo, "Optical thin films prepared by ion-assisted and ultrasound-assisted deposition," PhD dissertation, University of Arizona, 1988.
- C. K. Hwangbo, L. J. Lingg, J. P. Lehan, H. A. Macleod, J. L. Makous, and S. Y. Kim, "Ion-assisted deposition of thermally evaporated Ag and Al films," Appl. Opt. 28, 2769-2773 (1989).
- C. K. Hwangbo, L. J. Lingg, J. P. Lehan, H. A. Macleod, and F. Suits, "Reactive ion-assisted deposition of aluminum oxynitride thin films," Appl. Opt. 28, 2779-2784 (1989).
- B. G. Bovard and H. A. Macleod, "Nonlinear behavior of optical coatings subjected to intense laser irradiation," submitted to J. Mod. Opt.
- C. K. Hwangbo, L. J. Lingg, J. P. Lehan, and H. A. Macleod, J. L. Makous, and S. Y. Kim, "Ion-assisted deposition of thermally evaporated Ag and Al films," submitted to Appl. Opt.

Presentations

- Y. Mao, B. G. Bovard, J. P. Lehan, T. Zhao, D. Oliyev, and H. A. Macleod, "Thermal stress in Zirconium Dioxide Thin Films," presented at 1989 OSA Annual Meeting, Orlando, Florida.

J. A. LEAVITT and L. C. McINTYRE, Jr.

Publications

- L. C. McIntyre, Jr., M. D. Ashbaugh, and J. A. Leavitt, "Limits on the accuracy of stoichiometry determined by Rutherford backscattering using computer peak fitting," MRS Symposia Proceedings 93, 311 (1987).
- J. A. Leavitt, "MeV ion beam analysis of thin films," National Technical University Research Seminar video tape, available from Microcampus, University of Arizona, Oct. 27, 1987.

- J. L. Makous, J. A. Leavitt, L. C. McIntyre, Jr., R. Maritato, A. M. Cucolo, and C. M. Falco, "Superconducting superlattice structures," *Proc. Mat. Res. Soc.* **103**, 287 (1987).
- T. H. Allen, J. P. Lehan, and L. C. McIntyre, "Ion beam sputtered magnesium fluoride," in *Optical Interference Coatings*, 1988 Technical Digest Series, Vol. 6, p. 32 (Optical Society of America, Washington DC, 1988).
- J. A. Leavitt, L. C. McIntyre, Jr., M. D. Ashbaugh, and J. G. Oder, "Characterization of optical coatings with backscattering spectrometry," in *Optical Interference Coatings*, 1988 Technical Digest Series, Vol. 6, p. 32 (Optical Society of America, Washington DC, 1988).
- J. A. Leavitt, L. C. McIntyre, Jr., P. Stoss, M. D. Ashbaugh, B. Dezfouly-Arjomandy, M. F. Hinedi, and G. Van Zijill, "Backscattering spectrometry with ^4He , ^{12}C , ^{14}N , ^{40}Ar , and ^{34}Kr analysis beams with energies 1.5 to 5.0 MeV," *Nucl. Instr. and Meth. B* **35**, 333 (1988).
- L. C. McIntyre, Jr., J. A. Leavitt, B. Dezfouly-Arjomandy, and J. Oder, "Depth profiling of phosphorus using resonances in the $^{31}\text{P}(\alpha, p)^{34}\text{S}$ reaction," *Nucl. Instr. Meth. B* **35**, 446 (1988).
- J. P. Cronin, T. J. Gudgel, L. Zanotto, B. Dutta, G. P. Rajendran, G. Dale, E. D. Zanotto, E. V. Uhlmann, G. L. Smith, M. Denesuk, B. D. Fabes, D. R. Uhlmann, J. A. Leavitt, and J. R. Martin, "Wet chemistry-driven barrier layers for ceramic superconductor films," in *Ceramic Superconductors II*, M. F. Yan, ed. (The American Ceramic Society, Inc., Westerville, Ohio, 1989), pp. 511-523.
- J. A. Leavitt, L. C. McIntyre, Jr., M. D. Ashbaugh, B. Dezfouly-Arjomandy, and J. G. Oder, "Characterization of optical coatings with backscattering spectrometry," *Appl. Opt.* **28**, 2762 (1989).
- J. A. Leavitt and L. C. McIntyre, Jr., "MeV ion beam analysis of high T_c superconducting films," *Nuclear Instruments and Methods B* **40/41**, 797 (1989).
- J. A. Leavitt, L. C. McIntyre, Jr., J. G. Oder, P. Stoss, M. D. Ashbaugh, B. Dezfouly-Arjomandy, Z. Lin, and Z.-M. Yang, "Cross sections for 170° backscattering of ^4He from carbon for ^4He energies between 1.8 and 5.0 MeV," *Nuclear Instruments and Methods B* **40/41**, 776 (1989).
- J. A. Leavitt, L. C. McIntyre, Jr., M. D. Ashbaugh, J. G. Oder, Z. Lin, and B. Dezfouly-Arjomandy, "Cross sections for 170.5° backscattering of ^4He from oxygen for ^4He energies between 1.8 and 5.0 MeV," *Nucl. Instr. Meth. B* **44**, 260 (1990).
- J. A. Leavitt, and L. C. McIntyre, Jr., "High energy ^4He backscattering," in *High-Energy and Heavy Ion Beams in Materials Analysis*, J. R. Tesma, C. J. Maggiore, M. Nastasi, J. C. Barbous, and J. W. Mayer, eds. (Materials Research Society, Pittsburgh, 1990), pp. 129-138.
- L. C. McIntyre, J. A. Leavitt, M. D. Ashbaugh, B. Dezfouly-Arjomandy, Z. Lin, J. Oder, R. F. C. Farrow, and S. S. P. Parkin, "Detection and depth profiling of ^{19}F using resonances in the $^{19}\text{F}(\alpha, p)^{22}\text{Ne}$ reaction," *Proc. Int. Symp. on Application of Nuclear Techniques*, Shanghai, China, May 22-26, 1989).

V. Garcia-Vazquez, K. D. Powers, J. A. Leavitt, L. C. McIntyre, Jr., and C. M. Falco, "Preparation of YBaCuO thin films by multilayer deposition," *Mod. Phys. Lett. B* **3**, 1039 (1989).

G. I. STEGEMAN and C. T. SEATON

V. Mizrahi, F. Suits, J. E. Sipe, U. J. Gibson, and G. I. Stegeman, "New probe of thin-film microstructure," *Appl. Phys. Lett.* **51**(6), (1987).

S. Lee, B. Hillebrands, G. I. Stegeman, H. Cheng, J. E. Potts, and F. Nizzoli, "Elastic properties of epitaxial ZnSe(001) films on GaAs measured by Brillouin spectroscopy," *J. Appl. Phys.* **63**, 1914 (1988).

B. Hillebrands, S. Lee, G. I. Stegeman, H. Cheng, J. E. Potts, and F. Nizzoli, "Observation of a guided longitudinal acoustic phonon in epitaxial ZnSe films on GaAs," *Phys. Rev. Lett.* **60**, 832 (1988).

J. A. Bell, W. R. Bennett, R. Zanoni, G. I. Stegeman, C. M. Falco, and C. T. Seaton, "Elastic constants of, and Stonely waves in molybdenum films measured by Brillouin scattering," *Appl. Phys. Lett.* **52**, 610 (1988).

J. A. Bell, W. R. Bennett, R. Zanoni, G. I. Stegeman, C. M. Falco, and C. T. Seaton, "Elastic constants of Cu/Nb superlattices," *Solid State Commun.* **64**, 1339 (1988).

C. M. Falco, J. L. Makous, J. A. Bell, W. R. Bennett, R. Zanoni, G. I. Stegeman, and C. T. Seaton, "Competing interactions in metallic superlattices," *Proc. of CMS Workshop*, R. LeSar, A. Bishop, and R. Heffner, eds. (Springer-Verlag, Berlin, 1988), pp. 139-145.

D. G. Gleed, B. Hillebrands, S. Lee, G. I. Stegeman, J. R. Sambles, and N. J. Geddes, "Brillouin spectra from Langmuir-Blodgett films of 22-Tricosenoic acid," *J. Phys. Condensed Matter* **1**, 3663 (1989).

D. G. Gleed, B. Hillebrands, S. Lee, G. I. Stegeman, and J. R. Sambles, "The angular dependence of surface-enhanced Brillouin scattering from silver (double resonance effect)," *Solid State Commun.* **70**, 237 (1989).

S. Lee, B. Hillebrands, G. I. Stegeman, B. Dunn, L. A. Momoda, and F. Nizzoli, "Elastic properties of Na⁺β"-alumina measured by Brillouin spectroscopy," *Solid State Commun.* **70**, 14-18 (1989).

F. Nizzoli, S. Lee, W. Knoll, and G. I. Stegeman, "Determination of the whole set of elastic constants of a Langmuir-Blodgett film by Brillouin spectroscopy," *Phys. Rev. B* **40**, 3323 (1989).

V. Mizrahi, G. I. Stegeman, and W. Knoll, "Anisotropic orientation distribution in polycrystalline Langmuir-Blodgett monolayers as revealed by second-harmonic generation," *Chem. Phys. Lett.* **156**, 92 (1989).

V. Mizrahi, G. I. Stegeman, and W. Knoll, "Microstructure of J-band forming cyanine dye monolayer probed by second-harmonic generation," *Phys. Rev. A* **39**, 3555 (1989).

- B. Hillebrands, S. Lee, G. I. Stegeman, H. Cheng, J. E. Potts, and F. Nizzoli, "Evidence for the existence of guided longitudinal acoustic phonons in ZnSe films on GaAs."
- G. I. Stegeman, J. A. Bell, W. R. Bennett, G. Duda, C. M. Falco, U. J. Gibson, B. Hillebrands, W. Knoll, L. A. Laxhuber, S. M. Lee, J. Makous, F. Nizzoli, C. T. Seaton, J. D. Swalen, G. Wegner, and R. Zanoni, "Brillouin scattering from thin films," Proc. of Workshop on Scattering of Electromagnetic Radiation, in press.
- B. Hillebrands, A. Boufelfel, C. M. Falco, P. Baumgart, G. Güntherodt, E. Zirngiebl, and J. D. Thompson, J. Appl. Phys., in press.
- A. Boufelfel, B. Hillebrands, G. I. Stegeman, L. A. Laxhuber, and J. D. Swalen, "Elastic properties of unpolymerized and polymerized ODF and ODM Langmuir-Blodgett films determined by Brillouin scattering," J. Chem. Phys., in press.
- V. Mizrahi, G. I. Stegeman, and W. Knoll, "Second-harmonic generation as a probe of thin film and monolayer microstructure," Proceedings of Trends in Quantum Electronics 88, in press.
- J. A. Ruffner, M. D. Himel, V. Mizrahi, G. I. Stegeman, and U. J. Gibson, "Effects of low substrate temperature and ion-assisted deposition on composition, optical properties and stress of ZnS thin films," Appl. Opt., to be published.
- S. Lee, B. Hillebrands, J. Dutcher, G. I. Stegeman, W. Knoll, and F. Nizzoli, "Dispersion and localization of acoustic guided modes in a Langmuir-Blodgett film studied by surface-polariton-enhanced Brillouin scattering," Phys. Rev. B, submitted.
- V. Mizrahi, G. I. Stegeman, and W. Knoll, "Anisotropic orientation distribution in polycrystalline Langmuir-Blodgett monolayers revealed by second-harmonic generation," Phys. Rev. Lett., submitted.
- J. A. Bell, R. J. Zanoni, C. T. Seaton, and G. I. Stegeman, W. Bennett, and C. M. Falco, "Brillouin scattering from Love waves in Cu/Nb metallic superlattices," Appl. Phys. Lett. submitted.

S. LICHTER

- A. J. Bernoff and S. Lichter, "A continuum model of thin film deposition and growth," submitted to Phys. Rev. B

C. FALCO

- B. Hillebrands, P. Baumgart, G. Güntherodt, E. Zirngiebl, and J. D. Thompson, "Brillouin scattering from collective spin waves in magnetic superlattices," J. Appl. Phys. **63**, 3880 (1988) Invited.
- F. E. Fernandez, C. Riedel, A. Smith, B. Edwards, B. Lai, F. Cerrina, M. G. Lagally, M. J. Carr, A. D. Romig, Jr., J. Corno, L. Nevot, B. Pardo, J. M. Slaughter, and C. M. Falco, " Monolithic Fabry-Perot Structure for soft x rays," Proc. SPIE 984, (1988).

- P. A. Kearney, J. M. Slaughter, K. D. Powers, and C. M. Falco, "Soft x-ray multilayers produced by sputtering and molecular beam epitaxy (MBE): substrate and interfacial roughness," Proc. SPIE 984 (1984).
- Z. Milanovic, M. A. Voelker, M. F. Kelley, K. D. Powers, and C. M. Falco, "Surface roughness healing of substrates for XUV multilayer coatings," Proc. SPIE 984 (1988).
- D. Schulze, J. M. Slaughter, and C. M. Falco, "Molecular beam epitaxy for multilayer fabrication," Proc. SPIE 984 (1988).
- J. M. Slaughter, M. K. Burkland, P. A. Kearney, A. R. Lampis, Z. Milanovic, D. W. Schulze, J. R. Roberts, J. Kerner, E. B. Saloman, and C. M. Falco, "Multilayer mirrors for 182 Å," Proc. SPIE 1160, 235-244 (1989).
- M. K. Burkland, J. M. Slaughter, and C. M. Falco, "Ex situ characterization of MBE-grown molybdenum silicide thin films," The 8th Annual Symposium of the Arizona Chapter of The American Vacuum Society, Tucson, Arizona, April 6&7, 1989.
- V. Garcia-Vazquez, K. D. Powers, J. A. Leavitt, L. McIntyre, and C. M. Falco, "Preparation of YBaCuO thin films by multilayer deposition," Mod. Phys. Lett. B 3, 1039 (1989).

Nd: YAG LASER ABLATION OF BaTiO₃ THIN FILMS

*URSULA J. GIBSON, **J.A. RUFFNER,***J.J. MCNALLY and ****G. PETERSON,
*Thayer School of Engineering, Dartmouth College, Hanover, NH 03755
**Optical Sciences Center, University of Arizona, Tucson, AZ
*** Physics Department, United States Airforce Academy, CO
****Physics Dept., University of New Mexico, Albuquerque, Mexico

ABSTRACT

We have deposited thin films of barium titanate onto a variety of substrates, using picosecond and nanosecond pulsed Nd: YAG lasers. The films were deposited from a hot-pressed target onto substrates that were heated by either CO₂ laser or conventional means, in a partial pressure of oxygen. Highly oriented films resulted from depositions onto MgO and LiF substrates held at temperatures greater than 600C.

INTRODUCTION

There has been a dramatic increase in laser ablation of thin films in recent years, due largely to the success of this technique in the production of high T_c superconductors [1-4]. The highly non-equilibrium nature of the technique allows congruent vaporization of oxides with complex stoichiometries. More recently, the technique has been applied to the production of thin films of optical materials, such as BaTiO₃ and glasses [5-7]. This study involves the exploration of pulselength and wavelength behavior for the deposition of BaTiO₃, and the use of CO₂ laser for substrate heating in an oxidizing environment. Others have suggested that shorter ablation wavelengths result in smoother, more uniform films [8,9]. Our results agree with the previous work, and suggest that shorter pulses (30psec vs 20nsec) result in much rougher films.

EXPERIMENT

The experimental setup for the deposition of BaTiO₃ films is shown in fig. 1. A metal-sealed chamber was equipped to permit rotation of the target, which was illuminated by the ablating pulses at a variable angle of 30-45 degrees. The substrate and heater assembly were mounted on an adjustable stage, permitting variation of the target-substrate distance over a range of 2-10 cm. A shutter was placed so that the Nd: YAG laser could be aligned on the target without exposing the substrate to the ablated material. An antireflection-coated ZnSe window was mounted opposite the substrate stage, to permit CO₂ laser illumination of the substrate during deposition. The system was cryopumped, with the pump throttled down when oxygen was admitted through a variable leak valve.

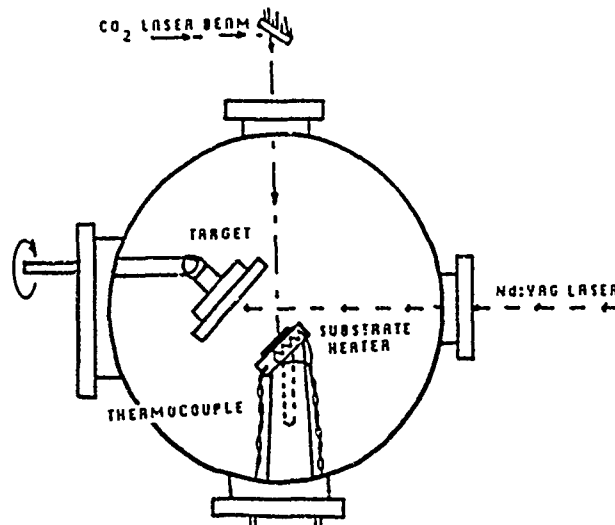


Figure 1 Schematic of experimental setup

Substrates were prepared by various means; single crystal NaCl and LiF were cleaved in air and placed directly in the chamber with no additional preparation, polished MgO substrates were either cleaned in methanol and placed into the chamber, or etched in nitric acid and rinsed in H₂O and methanol before mounting. Silicon wafers and silica substrates were cleaned in acetone and methanol. The substrates were mounted on a stainless steel block which could be radiatively heated from behind by Kanthal wire wrapped around a high temperature silica form. An Iron-Constantan thermocouple was mounted directly into the side of the stainless block, and for the conventionally heated films, the nominal substrate temperature is taken from these readings. In addition, substrates could be heated by exposure to 10.6 μ radiation from a modulated 25W rf excited CO₂ laser. For films heated with the CO₂ laser, two methods were used to determine the substrate temperature. Initially, power settings determined in a calibration run where a thermocouple was sandwiched between two pieces of MgO were used. For later runs, we used an optical pyrometer focussed on the center of the CO₂ spot, but the substrate temperatures of interest were at the extreme low end of the pyrometer's range. Neither method is believed to be accurate to better than 10%, especially in light of the temperature gradient from the center of the spot to the edge of the substrate.

The target was a commercially obtained hot-pressed disk of stoichiometric BaTiO₃, 2" in diameter. It was mounted in a stainless steel holder that was rotated in front of the ablating beam at 0.5 Hz. The angle of the target with respect to the impinging beam could be varied by 15 degrees; most films were deposited with the target normal at 40-45 degrees relative to the laser path. The target-substrate distance was 5cm. Significant erosion and grooving of the target resulted from the ablation process; when the target surface became highly irregular, it was sanded flat. The nature of the target damage was markedly different for the picosecond vs. nanosecond pulses, independent of wavelength. For the picosecond pulses, deep, undisclored grooves resulted, whereas for the nanosecond pulses, wider, blackened region resulted. Although the beam quality was not the same in both cases, this suggested a more explosive ablation from the picosecond pulses.

The ablation was performed either by a Quantel YG501 mode-locked YAG laser with a rep rate of 10 Hz and a pulse width of 25-35 psec., or by a Quantaray DCR-II, with a pulsewidth of 15-20 nsec. Films were made using the doubled (532 nm.) or quadrupled (266nm) output of the laser. Average power levels were between 60 and 90 mW in the green, and 20 mW in the UV for the picosecond pulses, and 60-70 mW in the UV and 70-125mW in the green for the nanosecond pulses. The laser power was monitored intermittently during deposition, and typically held constant to 5%. The spot size was between 0.2 and 0.5 mm for all cases.

The chamber was pumped to a base pressure of 2-5 x 10⁻⁶ Torr, then backfilled with oxygen to a pressure of 2 x 10⁻⁴ to 2 x 10⁻² Torr. The substrate was brought up to temperature before deposition commenced. Deposition times for the 532nm ablated films were typically 30 mins, corresponding to a deposition rate of 0.5 Å/pulse. For films ablated using the fourth harmonic of the mode-locked laser, deposition times were longer, and the rate was slower, roughly 0.04 Å/pulse. No accurate determinations of the deposition rate were made for the nanosecond pulses, but the rates were observed to be comparable to those obtained with psec pulses.

Films were analyzed using a variety of techniques including scanning electron and Nomarski microscopy, stylus profilometry, x-ray diffraction and Rutherford Backscattering Spectroscopy (RBS).

RESULTS AND DISCUSSION

The films that were produced using picosecond pulses showed a range of stoichiometries and crystal structures, but their larger scale structure was quite rough, which we believe to be due to the short pulse length used for the ablation. Films deposited using the nanosecond pulses were smoother, but also displayed a range of stoichiometries and crystal structures. Although the changes were larger for changes in pulselength, we observed reduced scatter and smoother films for UV depositions at each pulselength.

Morphology

All films made with picosecond pulses were comprised of small globules spattered onto the substrate. The films, as a result, were strongly scattering in the visible. We believe that this is

largely due to rapid deposition of the energy in the laser pulse. The experiments with nanosecond pulses at similar power levels yielded smooth films with finite numbers of micron-size inclusions.

Figure 2a is an SEM micrograph of a film produced with picosecond green pulses, showing a predominance of 3-5 μ globules. Figure 2b is a film produced under similar conditions, except using the fourth harmonic of the laser. The globules were smaller (0.3 - 0.8 μ) for the UV

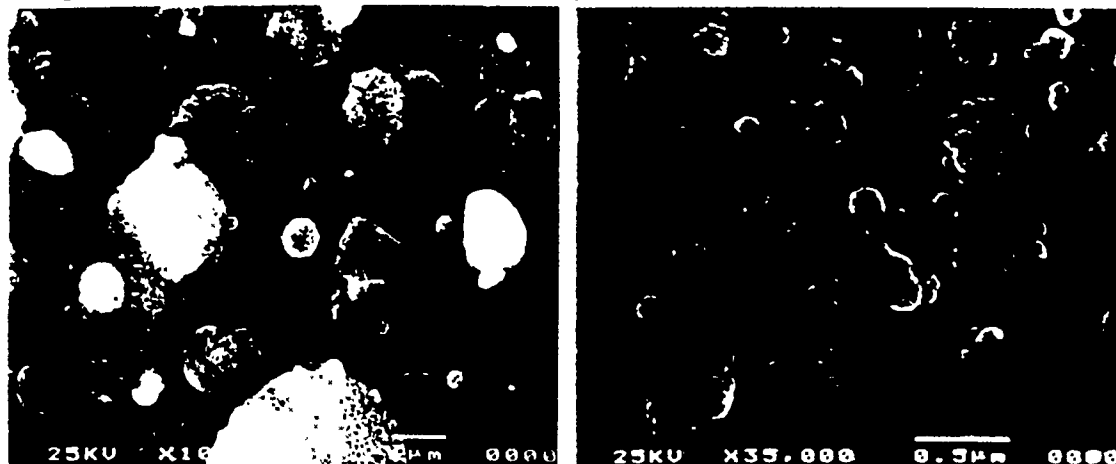


Figure 2 a) SEM micrograph of film deposited with $\lambda = 532\text{nm}$, pulselength $\approx 30\text{psec}$ onto a cleaned but not deglassed silicon wafer. Substrate temp = 450°C , and the average laser power was $\sim 75\text{mW}$.

b) SEM micrograph of a film deposited as above, but $\lambda = 266\text{nm}$, average power $\sim 20\text{mW}$.

ablated film, but the films were still strongly scattering. Reduction of the average power levels at both wavelengths did not appreciably change the morphology of the films. The apparent porosity of the films is corroborated by RBS data which indicates that the substrate is exposed in some places.

At elevated substrate temperatures ($> 600^\circ\text{C}$), this rough morphology was maintained on MgO and LiF, even though epitaxial alignment of the film with the substrate was observed. High angle SEM viewing of the films indicate that the globules are flattened, suggesting that they arrive in a molten condition. The elevated substrate temperature presumably allows them to cool slowly enough to align with the substrate as they crystallize.

Figure 3a is an SEM micrograph of a film deposited with nsec pulses at $\lambda = 532\text{nm}$. A finite number of 0.5 - 3.0 μ inclusions decorate an otherwise smooth film. Figure 3b shows a film comparable to that in Fig. 2b, but made with nanosecond UV pulses. These films were specularly reflecting, and approximately bulk density.

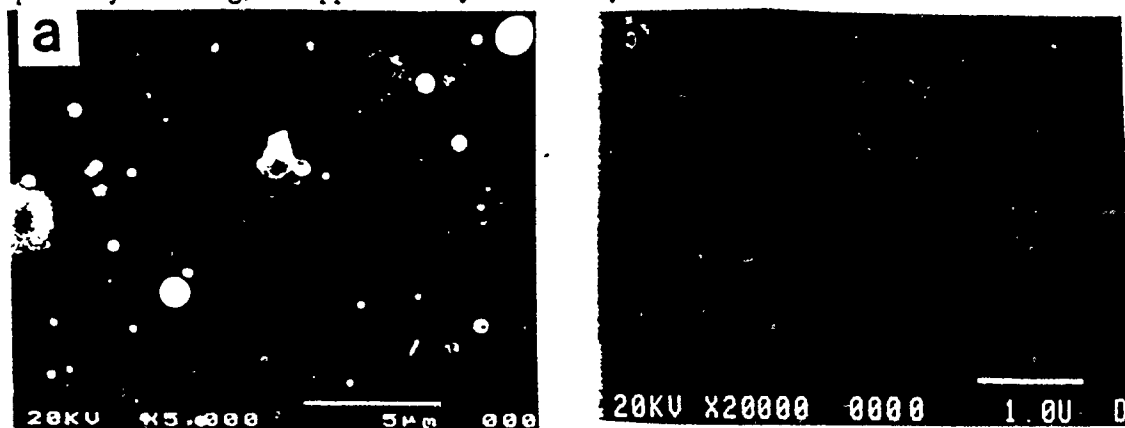


Figure 3 a) SEM micrograph of a film deposited onto MgO with nanosecond pulses at $\lambda = 532\text{nm}$ substrate; temperature $\approx 650^\circ\text{C}$, and 70mW average power.

b) SEM micrograph of film deposited with conditions the same as in Figure 3a except $\lambda = 266\text{nm}$.

Composition

The composition of the films was determined using both XPS and RBS. X-ray photoelectron spectroscopy was used to confirm that the elements in the films were in the bonding states expected for BaTiO_3 . RBS, which is more accurate for elemental composition numbers, was used for routine analysis of the films.

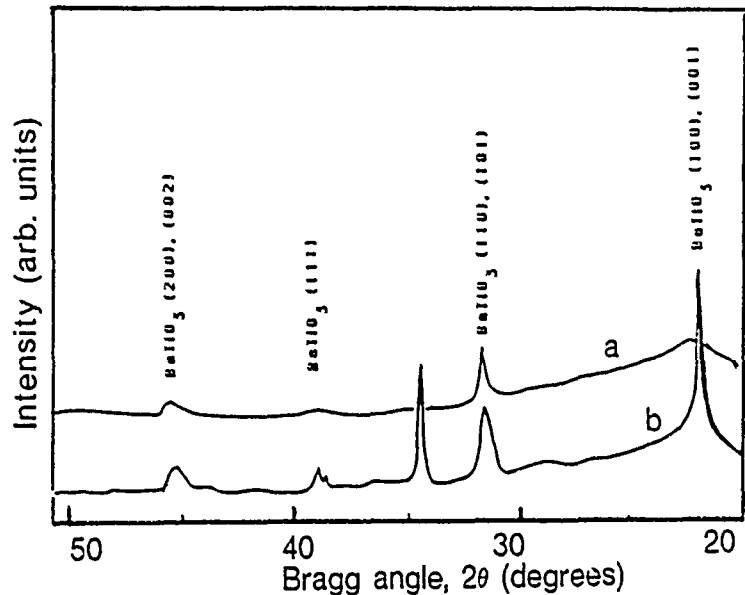
The films were, in general, Ti rich. In some cases, the excess was very small, but for films deposited in a low backpressure of oxygen, onto a hot substrate, the ratio of Ti to Ba could be as high as 2, and of Ti to O, and high as 0.5. Our process control was not sufficient to give entirely reproducible results, and we believe that the target history was responsible for some of the observed variations. However, some interesting features were observed in the spectra. Films deposited with psec pulses showed undisplaced substrate peaks indicating some regions of the substrate were exposed. The shape of the peaks also indicated a non-uniform film thickness, in accord with our other observations. For films deposited with nanosecond green pulses onto MgO the onset of the Mg peak is displaced, indicating that the film covers the substrate completely. The shapes of the peaks indicate the presence of "bumps" on the film surface, in agreement with our SEM observations.

Crystal Structure

Films were initially deposited onto silicon wafers and fused silica substrates. These films were largely amorphous, even at substrate block temperatures in excess of 450 C. When a fused silica substrate was heated with the block and simultaneously illuminated locally with CO_2 laser, to a temperature of approximately 600°C, a polycrystalline film resulted, as indicated by x-ray diffraction (XRD) data shown in Fig. 4.

Figure 4

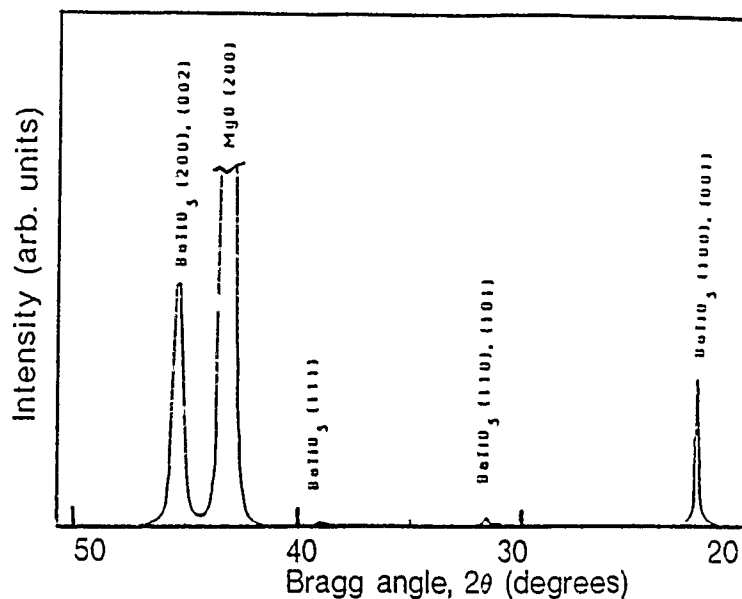
XRD traces of a film deposited onto fused silica held at 450°C and heated with the CO_2 laser. a) an area outside the laser spot, b) area heated by the laser.



LiF and NaCl substrates were also used, in part to investigate the mechanism of the CO_2 laser heating. NaCl is transparent to the CO_2 , and thus the heat was deposited directly into the BaTiO_3 . Little effect was noted, although the laser spot induced a slight local increase in roughness of the film. No enhancement of crystal growth was observed which is perhaps not surprising when one considers the lattice mismatch. The most promising results were achieved with films deposited on LiF and MgO substrates. CO_2 heating was extremely efficient with the oxide, and temperatures up to 1800 degrees C were easily reached, although they were not desirable for BaTiO_3 growth. Fig. 5 shows an x-ray scan for a 0.5μ angstrom thick BaTiO_3 film deposited with green picosecond pulses onto MgO heated to 650 C using the CO_2 laser alone. There is a strong (100)/(001) texture, but it is not possible to resolve whether the film is in the cubic or tetragonal phase.

Figure 5

XRD trace of BaTiO_3 on MgO heated to 650°C using the CO_2 laser, and ablated using psec. green pulses



Films deposited with nanosecond pulses were smoother, and exhibited equivalent crystalline growth to those deposited with the psec pulses. Fig. 6a is the XRD trace for a film deposited with nanosecond UV pulses onto MgO held at 700 degrees using CO_2 heating. Fig. 6b shows x-ray data for a film deposited onto LiF heated to approximately 650° , and using UV nsec pulses. There is almost total suppression of the (110) lines in this film. However, the lattice constant measured for this and another film deposited under similar conditions was 4.08 \AA . This is possibly due to the island morphology exhibited in Fig. 7a; some regions of the film were discontinuous. Other regions were smooth and continuous, as shown in Fig. 7b.

Figure 6a

XRD data for a film deposited on MgO at 700°C using nsec. UV pulses.

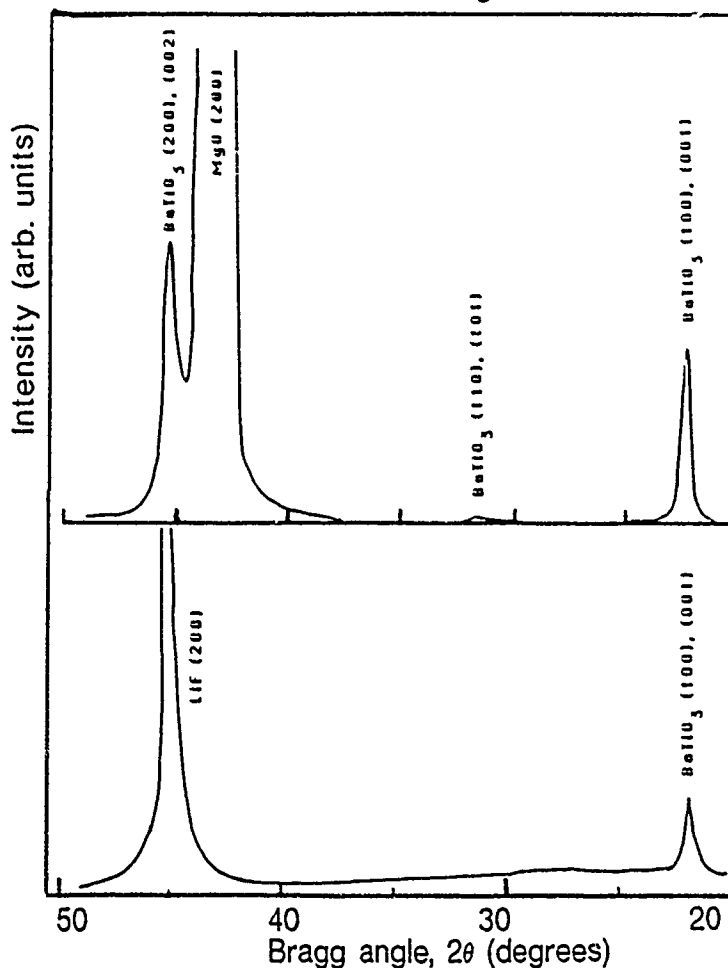


Figure 6b

XRD data for a film deposited on LiF at 650°C using nsec. pulses at 266 nm.

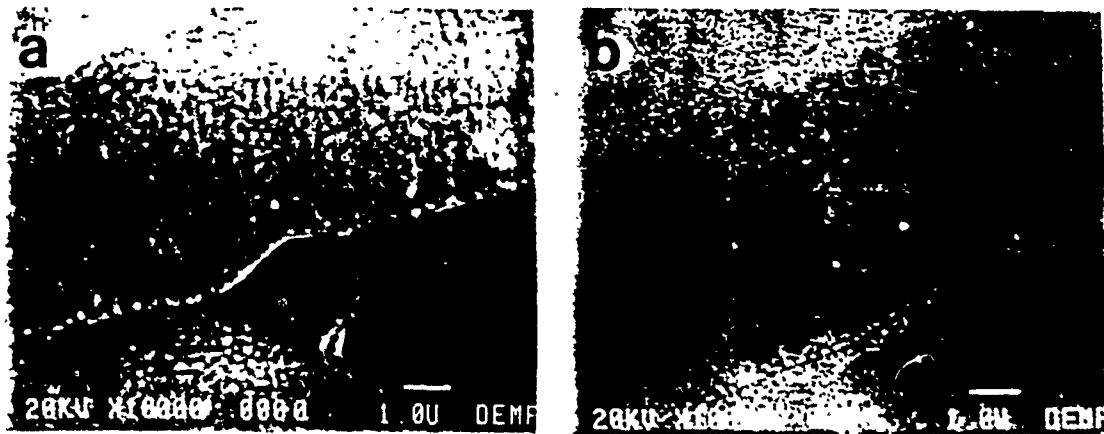


Figure 7 SEM micrograph of BaTiO₃ on LiF a) a discontinuous area b) continuous layer.

CONCLUSIONS

BaTiO₃ films were deposited with picosecond and nanosecond pulses at $\lambda = 532$ and 266 nm. Films deposited with the picosecond pulses were comprised of small molten spatters, resulting in a high degree of scattering. Despite this rough morphology, significant epitaxial alignment was observed on single crystal substrates held at high temperatures. In contrast, the nanosecond ablation resulted in specular films with improved quality for the UV vs green ablation wavelength. On each timescale, the shorter wavelengths were seen to result in smoother films with comparable or better crystal quality. A range of stoichiometries was observed for the deposition conditions used.

The use of the fourth harmonic of a Nd: YAG pulsed laser with nanosecond pulses has been shown to be a viable technique for the production of epitaxial BaTiO₃ films. CO₂ laser heating of the substrates was also shown to be a powerful technique for use in oxidizing environments.

ACKNOWLEDGEMENTS: We are indebted to L. MacIntyre and Jack Leavitt at the Physics Department at the University of Arizona for the RBS measurements, and to the Air Force Office of Scientific Research for funding through the F.J. Seiler Research Laboratory, The University Resident Research Program, and the URIP Center for Thin Film Studies.

REFERENCES:

1. D.K. Fork, J.B. Boyce, F.A. Ponce, R.I. Johnson, G.B. Anderson, G.A.N. Connel, C.B. Fom, and T.H. Greballe, *Appl. Phys. Lett.* 53 337 (1988).
2. C. Richard Guarnieri, R.A. Roy, K.L. Sacenger, S.A. Shivashankar, D.S. Yee and J.J. Cumo. *Appl. Phys. Letter* 53 632 (1988).
3. D. Dijkkamp, T. Venkatesan, X.D. Wu, S.A. Shaheen, N. Jiswari, Y.H. Min-Lee. W.L. McLean and M. Croft. *Appl. Phys. Lett.* 51 619 (1987).
4. J. Narayan, N. Biunno, R. Singh, W. Holland and O. Auciello. *Appl. Phys. Letter* 51 1845 (1987).
5. L. Lynds, B.R. Weinberger, G.G. Peterson and H.A. Krasinski. *Appl. Phys. Lett.* 52 (4) 320 (1988).
6. E.M. Vogel, E.W. Chase, J.L. Jackel and B.J. Wilkens, *Appl. Opt* 28, 649 (1989).
7. G.M. Davis and M.C. Grower, *CLEO '89*.
8. H. Sankur and J. Cheung, *Appl. Phys. A* 47, 271 (1988).
9. J. Perriere, G. Hauchecorne, F. Kerhev , F. Rochet, R.M. Defourneau, C. Simon, I. Rosenman, J.P. Enard, A. Laurent, E. Fogarassy and C. Fuchs, *J. Mater. Res.* 5, 258 (1990).

CROSS SECTIONS FOR 170.5° BACKSCATTERING OF ⁴He FROM OXYGEN FOR ⁴He ENERGIES BETWEEN 1.8 AND 5.0 MeV *

J.A. LEAVITT, L.C. McINTYRE, Jr., M.D. ASHBAUGH, J.G. ODER, Z. LIN
and B. DEZFOULY-ARJOMANDY

Department of Physics, University of Arizona, Tucson, AZ 85721, USA

Received 14 July 1989

Cross sections for 170.5° backscattering of ⁴He ions by natural oxygen atoms in target films for ⁴He laboratory energies in the range 1.8-5.0 MeV have been measured. A thick (~35 keV) Al₂O₃ target film (~850 Å), deposited on a carbon substrate and overcoated with ~200 Å of Ta, was used for cross-section measurement in nonresonant regions. A thin (~6 keV) Ta, Nb-Al target film, containing 60% oxygen, was used in strong resonance regions. In both cases, the non-Rutherford ⁴He-O cross section was determined by comparison with the nearly Rutherford ⁴He-Ta cross section at the same energy. The cross sections were measured at maximum intervals of 50 keV, with smaller intervals used in the neighborhood of resonances. Results are given in graphical and tabular form; cross sections are given as ratios to the Rutherford cross section, with typical uncertainties of ±2%, resonance energy uncertainties are typically ±5 keV. Discrepancies between these and previous measurements are discussed.

1. Introduction

Use of ⁴He analysis beams in the higher-than-usual 2-5 MeV energy region for backscattering (BS) spectrometry [1,2] of thin films containing elements lighter than Ar requires measurement of the cross sections for scattering of ⁴He by these light elements. Strong departures from Rutherford scattering are observed for these cross section in this energy region. We have begun a systematic program to measure these cross sections; we report cross section measurements for ⁴He on O here.

The ⁴He-O cross sections for ⁴He energies in the 2-5 MeV region have been measured by a number of investigators [3-6]. We have not found these published results very useful for BS analysis; most of the measurements have been reported in graphical rather than numerical form, making it difficult to extract accurate cross section values or compare results of different investigators. Furthermore, there appear to be discrepancies between the reported results regarding both energy calibration and magnitude of cross section. Smooth regions, 3.5-3.8 MeV and 4.5-4.7 MeV, have been used extensively [2,6] for non-Rutherford backscattering measurement of oxygen in thin films. The more recent cross section measurements [6] do not appear to be in agreement with earlier measurements [3,7] between 3.5 and 3.8 MeV, nor are they [6] in

agreement with others [4] in the 4.5-4.7 MeV region. The well-known 3.045 MeV resonance has been used extensively for depth profiling [8,9]; this resonance region has recently been incorporated [7,10] into simulation programs and used to analyze oxygen in high-Z oxides with impressive results, with typical accuracies of 5% [10]. The energy of this resonance has been variously reported as (3.045 ± 0.010) MeV [3], (3.042 ± 0.003) MeV [11], (3.039 ± ?) MeV [7], and (3.0359 ± ?) MeV [12]. The purpose of this report is two-fold: 1) to resolve these discrepancies and 2) to provide an accurate numerical table of ⁴He-O cross sections measured at the common BS angle of 170.5°, for the 2-5 MeV energy region.

2. Experimental

Beams of ⁴He⁺ from our 5.5 MV Van de Graaff accelerator were used with a standard backscattering setup [2] to obtain BS spectra of films containing natural oxygen, which were dc sputtered onto pyrolytic graphite substrates (see table 1). Relevant experimental parameters were: detector (Ortec BA-14-25-100) resolution = 14 keV; solid angle subtended by the detector, $\Omega = (0.78 \pm 0.02)$ msr; backscattering angle = $\theta_{\text{Lab}} = 170.5^\circ \pm 0.5^\circ$, with backscattering angles in the range $170.5^\circ \pm 0.9^\circ$ accepted by the detector. The analysis beam energy was calibrated using three resonances [13] in ²⁴Mg(α, γ)²⁸Si at (2437.4 ± 1.0) keV, (2868 ± 2) keV, (3200 ± 1) keV, one resonance [14] at (3576 ± 3) keV in ¹⁴N(α, α)¹⁴N and one resonance [15] at (5058 ± 3) keV in ¹⁶O(α, α)¹⁶O. The 90° analyzing magnet used has a

* First presented at the 9th International Conference on Ion Beam Analysis, June 26-30, 1989, Kingston, Canada.

Table 1
Characteristics of the films used for measurement of the ⁴He-O cross sections

Film	Layer	Element	(Nt) ^{a1}	Atomic %
1	1	Ta	17.9	40.5 ± 0.6
	2	Al	15.3	
	3	Al	23.2	
	1-2-3	O	82.6	
2	1	Ta	114 ± 3	100
	2	Al	387 ± 12	39.1 ± 0.4
	2	O	599 ± 19	60.4 ± 0.4
	2	Ar	5.3 ± 0.4	0.5 ± 0.1

^{a1} × 10¹⁵ atoms/cm².

particle trajectory radius of 2.3 m and $ME/Z^2 = 600$ u MeV. The beam energy is uncertain by less than 0.08%; the beam energy spread is less than 2 keV. The "thin" film target 1 (~ 6 keV), with total energy losses of 7.4 and 5.2 keV at beam energies 2 and 4 MeV, respectively, was used for scans over narrow resonances. The "thick" film target 2 (~ 35 keV), with energy losses of 12 and 9 keV in the Ta layer, and 39 and 26 keV in the Al₂O₃ layer at beam energies of 2 and 4 MeV, respectively, was used for scans over the slowly varying portions of the cross section vs energy curve.

3. Analysis and results

The ⁴He-O cross section, $\sigma^0(E_O)$, at ⁴He laboratory energy, E_O , may be expressed [16] in terms of the Rutherford cross section, $\sigma_R^0(E_O)$, at the same energy, and measured quantities by

$$\frac{\sigma^0(E_O)}{\sigma_R^0(E_O)} = \left[\frac{A_O(E_O)/A_{Ta}(E_{Ta})}{A'_O(E'_O)/A'_{Ta}(E'_{Ta})} \right] \left[\frac{E'_{Ta} E_O}{E_{Ta} E'_O} \right]^2 \times \frac{F(E_{Ta})F(E'_O)}{F(E'_{Ta})}, \tag{1}$$

where $A'_O(E'_O)$ and $A'_{Ta}(E'_{Ta})$ are integrated O and Ta BS peak counts obtained from a BS spectrum taken with incident ⁴He beam energy E' (where scattering from both elements is Rutherford; E'_O and E'_{Ta} are mean ⁴He energy in the O and Ta layers), and $A_O(E_O)$, $A_{Ta}(E_{Ta})$, E_O , and E_{Ta} are corresponding quantities for beam energy E . It is assumed that except for small corrections [17] due to electron shells (the F factors), the ⁴He-O and ⁴He-Ta cross sections are Rutherford for beam energies 1.8-2.0 MeV and 1.8-5.0, respectively. Use of eq. (1) effectively allows determination of the non-Rutherford ⁴He-O cross section by comparison with the Rutherford ⁴He-Ta cross section at the same energy.

Integrated peak counts due to O and Ta were ex-

tracted (with background subtracted) from 249 BS spectra. For data taken with the thin target 1, the mean ⁴He energies in Ta and O were taken as the mean energy in the film; for data taken with thick target 2, the mean ⁴He energies in Ta and O were taken as the mean energies in the Ta and Al₂O₃ layers, respectively. The energy loss in the C buildup on the film surface (energy loss 0-2 keV) was compensated for by increasing the mean energy uncertainty by 2 keV. These peak counts and mean energies were inserted into eq. (1) to produce the measured values of the ⁴He-O cross sections listed in table 2 and plotted in figs. 1-7.

The behavior of the cross section over the 1.8-5.0 MeV region is shown in fig. 1; not all data are plotted. Enlarged portions of this figure are compared with calculated curves in figs. 2-6. The elastic cross sections were calculated in the 2-4 MeV region using the standard dispersion theory outlined by Cameron [3]. Partial wave phase shifts up to $l = 3$ were included and the narrow resonance approximation to the resonant phase shifts was used. The five resonances below 4 MeV reported by Cameron were included in the calculation using our parameters given in table 3. The hard sphere phase shifts were obtained using Coulomb wave functions calculated using the program of Bardin, et al. [18]. An interaction radius of 4.92 fm was used (instead of Cameron's value of 5.75 fm) in the calculation in an attempt to improve the fit to the data between 3.5 and 3.8 MeV. The resulting hard sphere phase shifts were then fitted by a cubic polynomial to provide an analytic expression for use in the final calculation. Fig. 6 shows the effect on the cross section of varying the interaction radius in the nonresonant energy region 3.4-3.8 MeV.

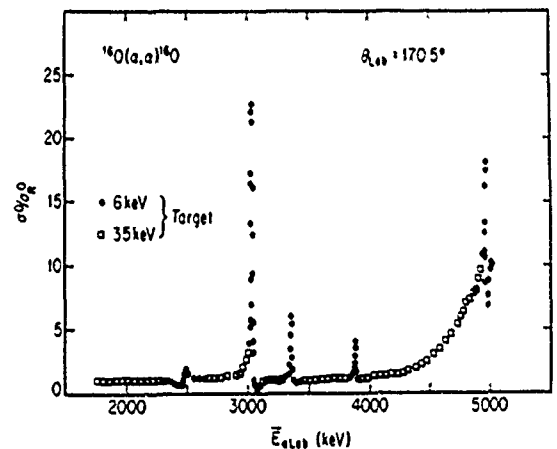


Fig. 1. Measured 170.5° laboratory elastic scattering cross sections, σ^0 , for ⁴He on O for ⁴He laboratory energies between 1.8 and 5.0 MeV, expressed in terms of the Rutherford cross sections, σ_R^0 , at the same energies. The solid circles and open squares are thin (~ 6 keV) and thick (~ 35 keV) target data, respectively. See table 2 for numerical values and uncertainties.

Table 2

Measured values of the ratio of the laboratory cross section, σ^l , to the Rutherford cross section, σ_R^l , at mean ^4He energies, \bar{E}_0 , for backscattering ($\theta_{\text{Lab}} = 170.5^\circ$) of ^4He by oxygen ($\delta =$ uncertainty in the ratio). Italics are used for values obtained with the thin target.

\bar{E}_0 (keV)	σ^l / σ_R^l	δ	\bar{E}_0 (keV)	σ^l / σ_R^l	δ
1769	1.01	0.02	2826	1.34	0.02
1819	1.00	0.02	2876	1.43	0.02
1857	1.01	0.02	2905	1.44	0.02
1870	0.99	0.02	2910	1.50	0.02
1920	1.01	0.02	2915	1.50	0.02
1970	0.98	0.02	2921	1.54	0.03
2021	0.99	0.02	2926	1.57	0.03
2071	0.99	0.02	2932	1.58	0.03
2121	1.00	0.02	2937	1.64	0.03
2172	1.00	0.02	2943	1.67	0.03
2222	1.01	0.02	2948	1.71	0.03
2272	1.00	0.01	2951	1.73	0.03
			2959	1.83	0.03
2295	0.94	0.04	2965	1.88	0.03
2317	0.93	0.04	2970	2.02	0.03
2339	0.94	0.04	2976	2.10	0.03
2361	0.90	0.04	2981	2.27	0.03
2383	0.92	0.04	2987	2.46	0.04
2405	0.87	0.04	2992	2.80	0.04
2427	0.80	0.04	2998	3.32	0.05
2449	0.67	0.03	3001	3.25	0.05
2459	0.62	0.03			
2464	0.60	0.03	3004	3.44	0.14
2469	0.58	0.03	3009	3.80	0.15
2472	0.64	0.04	3015	5.15	0.19
2474	0.67	0.03	3017	5.75	0.21
2479	0.98	0.04	3020	6.97	0.25
2484	1.48	0.05	3023	9.00	0.32
2489	1.71	0.05	3026	13.31	0.46
2494	1.90	0.05	3026	16.46	0.62
2499	1.84	0.05	3028	17.20	0.59
2504	1.74	0.05	3031	22.16	0.76
2509	1.63	0.05	3032	22.66	0.84
2514	1.59	0.05	3034	21.38	0.73
2517	1.42	0.05	3037	16.16	0.56
2519	1.51	0.05	3037	12.41	0.47
2524	1.45	0.05	3039	9.42	0.34
2529	1.50	0.05	3042	5.59	0.21
2534	1.39	0.04	3043	4.07	0.17
2539	1.39	0.05	3045	3.18	0.11
2544	1.32	0.04	3048	1.00	0.17
2549	1.33	0.04	3053	0.63	0.04
2554	1.31	0.04	3054	0.54	0.09
2559	1.26	0.04	3056	0.60	0.11
2562	1.22	0.05	3059	0.40	0.03
2585	1.25	0.05	3064	0.36	0.03
2608	1.25	0.05	3065	0.34	0.03
2631	1.24	0.05	3067	0.30	0.03
2654	1.22	0.05	3068	0.34	0.03
2675	1.27	0.02	3070	0.27	0.03
2725	1.24	0.02	3073	0.31	0.03
2775	1.27	0.02	3076	0.46	0.04

Table 2 (continued)

\bar{E}_0 (keV)	σ^l / σ_R^l	δ	\bar{E}_0 (keV)	σ^l / σ_R^l	δ
3079	0.53	0.04	3805	1.20	0.02
3081	0.70	0.05			
3084	0.75	0.04	3811	1.36	0.07
3087	0.71	0.05	3829	1.10	0.07
3090	0.70	0.04	3832	1.16	0.12
3093	0.73	0.05	3836	1.17	0.09
3098	0.64	0.04	3842	1.27	0.12
3101	0.64	0.04	3848	1.29	0.11
3104	0.64	0.04	3854	1.32	0.10
3109	0.74	0.05	3857	1.44	0.08
3112	0.75	0.04	3860	1.22	0.10
3115	0.72	0.05	3864	1.35	0.07
3121	0.79	0.05	3867	1.65	0.13
			3870	1.83	0.07
3127	0.79	0.01	3873	2.36	0.14
3152	0.85	0.01	3875	4.03	0.12
3177	0.92	0.02	3876	4.00	0.12
3202	0.95	0.02	3878	3.76	0.11
3227	1.00	0.02	3879	2.93	0.14
3252	1.07	0.02	3881	1.68	0.08
3277	1.14	0.02	3882	1.05	0.07
			3885	1.02	0.13
3297	1.21	0.06	3889	0.79	0.06
3308	1.29	0.06	3892	1.05	0.12
3320	1.34	0.06	3895	0.94	0.06
3331	1.50	0.07	3398	1.07	0.10
3343	1.81	0.08	3904	1.12	0.07
3348	2.20	0.07	3904	0.94	0.09
3354	3.40	0.10	3911	1.01	0.07
3355	3.20	0.12	3913	1.11	0.07
3357	4.50	0.12	3923	1.25	0.07
3360	6.05	0.14			
3363	5.96	0.14			
3366	5.43	0.18			
3369	2.76	0.09			
3372	1.77	0.07	3930	1.13	0.02
3378	1.00	0.06	3955	1.21	0.02
3383	0.77	0.04	3980	1.24	0.03
3389	0.80	0.04	4005	1.25	0.03
3401	0.74	0.05	4030	1.29	0.04
3413	0.82	0.05	4056	1.31	0.03
3425	0.84	0.05	4081	1.35	0.02
3436	0.86	0.05	4106	1.38	0.03
3453	0.92	0.02	4131	1.37	0.03
3478	0.95	0.02	4156	1.46	0.03
3503	0.97	0.02	4181	1.47	0.03
3529	1.00	0.02	4206	1.54	0.03
3553	1.03	0.02	4231	1.52	0.03
3579	1.04	0.02	4256	1.60	0.03
3606	1.06	0.02	4281	1.66	0.04
3629	1.07	0.02	4306	1.74	0.07
3654	1.08	0.02	4331	1.74	0.07
3679	1.10	0.02	4356	1.94	0.07
3704	1.13	0.02	4381	1.98	0.11
3729	1.10	0.02	4406	2.10	0.07
3754	1.15	0.02	4432	2.21	0.05
3779	1.16	0.02	4457	2.42	0.07

Table 2 (continued)

\bar{E}_1 (keV)	σ^0, σ_R^0	δ	\bar{E}_0 (keV)	σ^0, σ_R^0	δ
4482	2.57	0.08	4946	10.90	0.67
4482	2.54	0.06	4950	11.17	0.50
4507	2.72	0.05	4954	12.71	0.67
4532	2.97	0.05	4957	13.44	0.74
4557	3.21	0.06	4961	18.10	0.69
4582	3.44	0.06	4962	17.50	0.68
4607	3.79	0.06	4964	16.29	0.67
4631	4.08	0.07	4966	10.71	0.45
4657	4.47	0.07	4968	8.70	0.47
4682	4.70	0.08	4971	6.84	0.60
4708	5.07	0.08	4975	7.60	0.45
4732	5.53	0.09	4978	7.77	0.50
4757	5.96	0.09	4985	8.74	0.55
4782	6.29	0.09	5000	9.75	0.68
4808	7.03	0.11	5014	10.28	0.61
4833	7.21	0.11	5028	9.95	0.58
4858	7.82	0.11			
4883	8.23	0.12			
4908	8.87	0.13			
4933	9.57	0.14			

The effect of target thickness was included in the calculations by dividing the target into 10 layers, calculating the beam energy in each layer, and averaging the calculated cross section over these energies. The results of these calculations are shown as solid lines in figs. 2-6.

There is quite good agreement between our data and the calculated curves for the 2-4 MeV region. Our resonance energies average about 10 keV less than those given by Cameron (table 3), but the two sets are almost in agreement within mutual uncertainties. Our value of (3034 ± 4) keV (fig. 2) for the principal resonance energy is in agreement with the more recent measured values [7,12]. Further, the agreement between our data and the calculated curves is sufficiently good in the 2-4 MeV region to warrant cautious use of dispersion the-

Table 3

Resonance parameters l , E_r and Γ_λ associated with the resonances between 2 and 4 MeV in the ¹⁶O(α, α)¹⁶O cross section calculation. Results from this work are compared with those given by Cameron [3].

l	This work		Ref. [3]	
	E_r (keV)	Γ_λ (keV)	E_r (keV)	Γ_λ (keV)
0	2484 ± 4	24	2490 ± 10	24
3	3034 ± 4	10	3045 ± 10	10
0	3078 ± 5	5	3090 ± 10	5
2	3365 ± 5	10	3380 ± 10	10
2	3878 ± 5	2	3885 ± 10	3

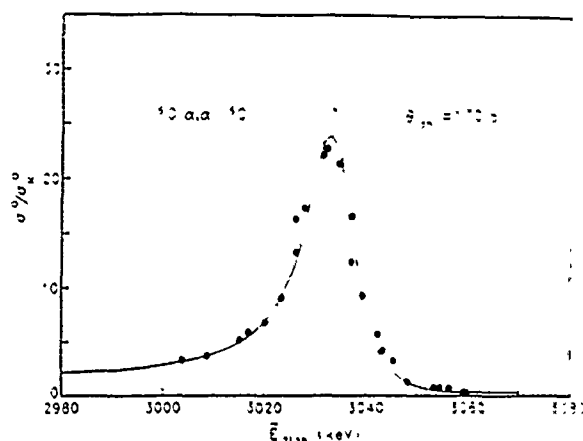


Fig. 2. Measured ⁴He-O laboratory cross sections near the strong "3045" keV resonance are compared with values (solid line) calculated using Cameron's procedures [3] and our resonance parameters listed in table 3, including the effect of target thickness. The dashed curve is the result of the calculation for infinitesimal target thickness. The data points shown were taken with the thin (6 keV) target. We obtain the resonance energy of (3034 ± 4) keV.

ory with the resonance parameters of table 3 to calculate cross sections for BS angles near 170°.

The 4-5 MeV region has not been covered by the calculations because resonances above 5 MeV must be included. However, fig. 7 shows a comparison of our current measurements with previous measurements [4,6] in the 4.7-5.0 MeV region. We attribute the ~10% disagreement between the current data and that of ref.

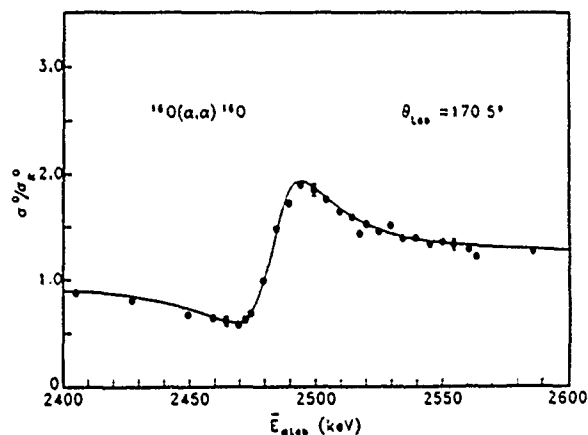


Fig. 3. Measured ⁴He-O laboratory cross sections near the (2484 ± 4) keV resonance are compared with values (solid line) calculated using Cameron's procedures [3] and our resonance parameters listed in table 3, including the effect of target thickness. In this case the effect of target thickness was negligible. The data points shown were taken with the thin (6 keV) target.

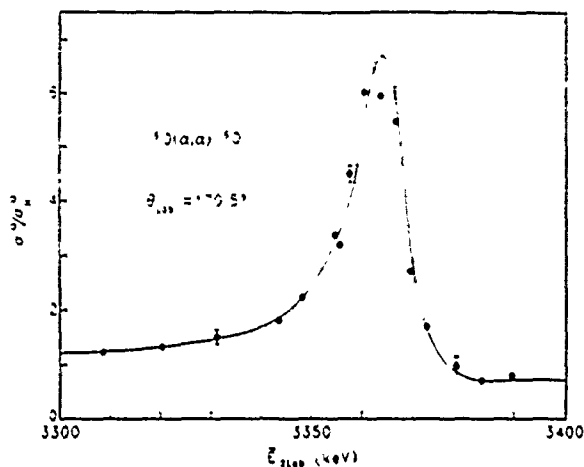


Fig. 4. Measured ^4He -O laboratory cross sections near the (3365 ± 5) keV resonance are compared with values (solid line) calculated using Cameron's procedures [3] and our resonance parameters listed in table 3, including the effect of target thickness. The dashed curve is the result of the calculation for infinitesimal target thickness. The data points shown were taken with the thin (6 keV) target.

[6] to charge normalization problems in the earlier work [6] not present in this work. Note that our current measurements agree with the earlier measurements [6] in the critical 3.5–3.8 MeV region (fig. 6). We attribute the $\sim 20\%$ disagreement between our current data and that of ref. [4] to the questionable energy calibration used in ref. [4]. The strong resonance shown at (4966 ± 6) keV in our data (fig. 7) appears at (5002 ± 5) keV in the

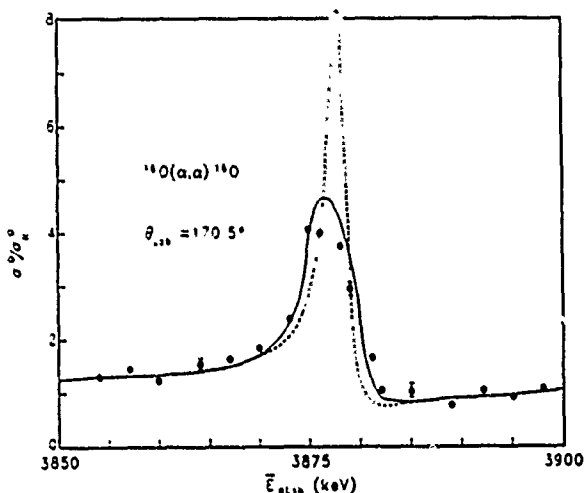


Fig. 5. Measured ^4He -O laboratory cross sections near the (3878 ± 5) keV resonance are compared with values (solid line) calculated using Cameron's procedures [3] and our resonance parameters listed in table 3, including the effect of target thickness. The dashed curve is the result of the calculation for infinitesimal target thickness. The data points shown were taken with the thin (6 keV) target.

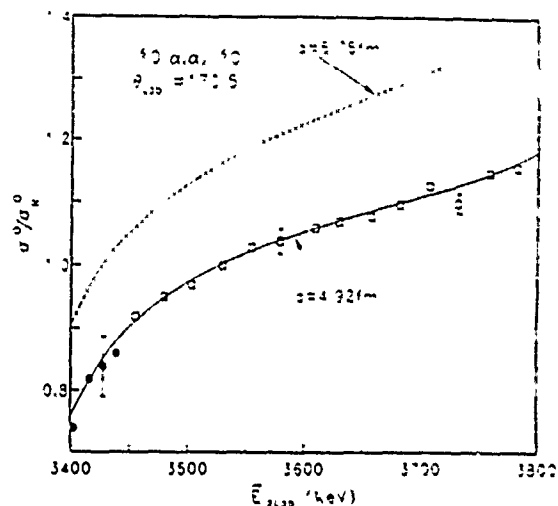


Fig. 6. Measured ^4He -O laboratory cross sections in the 3.4–3.8 MeV region are compared with values (solid line) calculated using Cameron's procedures [3] and our resonance parameters listed in table 3, neglecting the effect of target thickness which is negligible in this case. The data points shown as squares were taken with the thick (35 keV) target, those shown as dots were taken with the thin (6 keV) target. The dashed curve is a calculation with the interaction radius $a = 5.75$ fm used by Cameron [3].

ref. [4] data. Uncertainties of as much as 70 keV in the ref. [4] energy calibration have been noted by others [15,19].

Finally, the resonances at (3034 ± 4) , (3065 ± 5) , (3878 ± 5) and (4966 ± 6) keV may be used with "surface" O in a thin Al film (on C) for a quick energy calibration of the accelerator with ^4He BS.

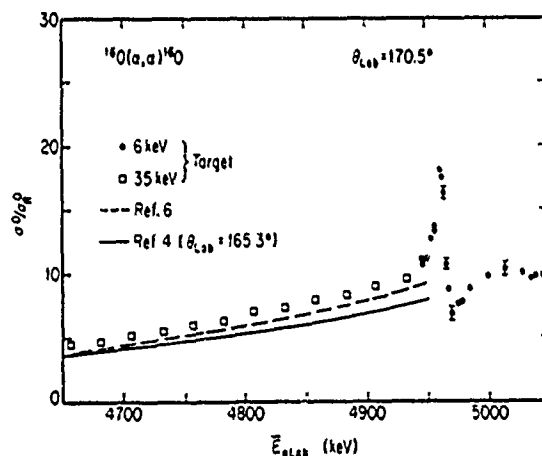


Fig. 7. Measured ^4He -O laboratory cross sections in the 4.7–5.0 MeV region are compared with results of previous measurements [4,6]. The sharp resonance at (4966 ± 6) keV is reported by ref. [4] at (5002 ± 5) keV. See the text.

In conclusion, we have measured the ^4He -O cross section for backscattering of ^4He at $\theta_{\text{Lab}} = 170.5^\circ$ for incident ^4He energies between 1.8 and 5.0 MeV. We have presented the results in a form that should be useful to those wishing to use the results for data analysis or comparison with their measured values.

We thank P. Stoss for his contributions to this research, and W. Bennett, R. Davis and C. Falco for providing the films. This work has been partially supported by IBM - Tucson, and by the Center for Thin Film Studies (AFOSR-URI) and the Optical Data Storage Center, both administered through the Optical Sciences Center, University of Arizona.

References

- [1] W.K. Chu, J.W. Mayer and M.-A. Nicolet, *Backscattering Spectrometry* (Academic Press, New York, 1978).
- [2] J.A. Leavitt, *Nucl. Instr. and Meth.* B24/25 (1987) 717.
- [3] J.R. Cameron, *Phys. Rev.* 90 (1953) 839.
- [4] L.C. McDermott, K.W. Jones, H. Smotrich and R.E. Benenson, *Phys. Rev.* 118 (1960) 175.
- [5] M.W. Buser, *Helv. Phys. Act.* 54 (1981) 339.
- [6] J.A. Leavitt, P. Stoss, D.B. Cooper, J.L. Seerveld, L.C. McIntyre, Jr., R.E. Davis, S. Gutierrez and T.M. Reith, *Nucl. Instr. and Meth.* B15 (1986) 296.
- [7] P. Berning and R.E. Benenson, *Nucl. Instr. and Meth.* B36 (1989) 335.
- [8] G. Mezey, J. Gyulai, T. Nagy, E. Kótai and A. Manuaba, *Ion Beam Surface Layer Analysis*, ed. O. Meyer, G. Linker and F. Kappeler (Plenum Press, New York, 1976), p. 303.
- [9] G. Mezey, E. Kótai, P. Révész, A. Manuaba, T. Lohner, J. Gyulai, M. Fried, Gy. Vizbeletky, F. Pasziti, G. Battistug and M. Somogyi, *Act. Phys. Hung.* 58 (1985) 39.
- [10] B. Blaspain, P. Revesy, L.R. Doolittle, K.H. Purser and J.W. Mayer, *Nucl. Instr. and Meth.* B34 (1988) 459.
- [11] Z.L. Wang, J.F.M. Westendorp and F.W. Saris, *Nucl. Instr. and Meth.* 211 (1983) 193.
- [12] S.H. Sie, D.R. McKense, G.B. Smuth and C.G. Ryan, *Nucl. Instr. and Meth.* B15 (1986) 525.
- [13] P.M. Endt and C. van der Leun, *Nucl. Phys.* A105 (1967) 1.
- [14] D.F. Herring, *Phys. Rev.* 112 (1958) 1217.
- [15] O. Häusser, A.J. Ferguson, A.B. McDonald, I.M. Szóghy, T.K. Alexander and D.L. Disdier, *Nucl. Phys.* A179 (1972) 465.
- [16] J.A. Leavitt, L.C. McIntyre, Jr., P. Stoss, J.G. Oder, M.D. Ashbaugh, B. Dezfouly-Arjomandy, Z.-M. Yang, and Z. Lin, *Nucl. Instr. and Meth.* B40/41 (1989) 776.
- [17] J. L'Ecuyer, J.A. Davies and N. Matsunami, *Nucl. Instr. and Meth.* 160 (1979) 337.
- [18] C. Bardin, Y. Dandeu, L. Gauthier, J. Gutlermin, T. Lena, J.M. Pernet, H.H. Wolter and T. Tamura, *Computer Phys. Commun.* 3 (1972) 73.
- [19] J. John, J.P. Aldridge and R.H. Davis, *Phys. Rev.* 181 (1969) 1455.

NON-RUTHERFORD ^4He CROSS SECTIONS FOR ION BEAM ANALYSIS

J. A. LEAVITT and L. C. McINTYRE, Jr.

Department of Physics, University of Arizona, Tucson, AZ 85721

Increasing use of ^4He analysis beams with energies between 2 and 10MeV for depth profiling and backscattering analysis of thin films and near-surface materials requires accurate measured values of non-Rutherford cross sections for scattering of ^4He by the lighter elements. Cross sections for scattering of ^4He through large angles deviate from Rutherford at ^4He laboratory energy $\sim 2.2\text{MeV}$ for target nuclei ^{12}C and ^{16}O ; deviations for target atomic number $Z=20$ and 40 occur at ^4He energies of about 5 and 10MeV, respectively. We review the experimental cross section data currently available for large angle scattering of ^4He from the light elements ($4 \leq Z \leq 20$) for incident ^4He laboratory energies 1.5 to 10MeV. For each target element, we indicate energy regions with smooth cross section variation suitable for use for simple backscattering analysis as well as strong narrow resonances that may be used for depth profiling light elements in heavy-element matrices.

Accepted for publication in Nuclear Instruments and Methods B - November, 1990.

1. Introduction

Rutherford backscattering spectrometry [1], utilizing ^4He analysis beams with energies in the 1.0-2.5MeV range, has been used extensively for accurate determination of stoichiometry, elemental areal density and "impurity" concentration in thin films. Increasing use of ^4He beams with energies between 2 and 10MeV for backscattering (BS) analysis requires accurate measured values of non-Rutherford cross sections for scattering of ^4He by the light elements [2]. The number of facilities capable of utilizing this higher energy region is rapidly growing [3]. Advantages associated with use of the higher energy ^4He beams, such as improved mass resolution, increased probing depth and improved accuracy in measured stoichiometric ratios, will frequently offset the inconvenience of using measured, rather than the calculated (Rutherford), cross sections. Energy analysis of the backscattered ^4He ions from a thin compound film yields a peak for each element present in the film. The elemental areal density, $(Nt)_i$, in atoms/cm², may be determined [1] for the i^{th} film element from knowledge of the detector solid angle, Ω , the cross section, σ_i , and the measured integrated peak count, A_i (for Q incident analysis ions) from:

$$(Nt)_i = \frac{A_i}{Q\Omega\sigma_i} \quad (1)$$

where t is the film thickness and N , the atomic density. The average stoichiometric ratio for film elements B and C , N_C/N_B , depends only on the ratio of integrated peak counts, A_C/A_B , and knowledge of the cross section ratio, σ_B/σ_C . Average stoichiometric ratios may be determined as accurately as a few tenths of a percent by acquisition of sufficient data if the BS peaks are well separated and if the cross section ratios are accurately known. Regarding the preferred choice of ^4He analysis energy: cross sections for BS of 2MeV ^4He on elements more massive than carbon are nearly Rutherford, so the cross section ratios may be accurately calculated at this energy. However, the resulting BS peaks frequently overlap and uncertainties in peak count ratios produced by deconvolution/simulation techniques frequently severely limit the accuracies of the measured stoichiometric ratios. Use of higher energy ^4He analysis beams usually results in desired reduction of peak overlap but may adversely affect the accuracy of the cross section ratio if the cross sections of interest are non-Rutherford. The ^4He analysis energy is usually chosen to be as high as possible to take advantage of the reduction in peak overlap, but with a value such that the relevant cross sections have accurate measured values that do not vary wildly in the energy region just below the incident ^4He energy. Cross sections for backscattering of 2-10MeV ^4He deviate

from Rutherford for all elements with $Z \lesssim 40$. The available experimental data [4-8] on energy thresholds for onset of non-Rutherford scattering for large angle BS of ${}^4\text{He}$ by light elements is in good agreement with the predictions of a recently developed theoretical model [9]. Both data and model indicate that cross sections for ${}^4\text{He}$ BS deviate from Rutherford at ${}^4\text{He}$ laboratory energy ~ 2.2 MeV for target nuclei ${}^{12}\text{C}$ and ${}^{16}\text{O}$; deviations for target atomic number $Z=20$ and 40 occur at ${}^4\text{He}$ energies of about 5 and 10 MeV, respectively. It is clear that successful exploitation of ${}^4\text{He}$ BS for energies 2 - 10 MeV requires accurate measured values of non-Rutherford cross sections over large energy regions.

2. Cross Sections

There is considerable information in the literature regarding these cross sections. Much of the data was acquired during the fifties and sixties in connection with studies of nuclear level structure; levels for the nucleus of mass number $A + 4$ were inferred from data for scattering of ${}^4\text{He}$ by the nucleus of mass number A . Excitation functions, that is, measured differential cross sections vs. incident ${}^4\text{He}$ energy, at several BS angles are usually compared with curves calculated using inferred level structure parameters (resonance energies and widths). Most experimental data are presented in graphical form only, although an unpublished compilation [10] gives tables of numerical values produced by using a computer digitizer on the graphical data for selected excitation curves.

In the remainder of this section, we review the experimental cross section data currently available for large angle scattering of ${}^4\text{He}$ by light target elements ($4 \leq Z \leq 20$). We summarize the results in table 1. For each element, we list the energy range, ΔE_{lab} , covered by the reported excitation function, the associated maximum BS angle, $\theta_{\text{lab}}^{\text{max}}$, the energy ranges, $\Delta E_{\text{lab}}^{\text{nr}}$, of smooth non-Rutherford regions appropriate for BS measurements, and the measured (calculated) value of the non-Rutherford threshold energy, $E_{\text{lab}}^{\text{nr}}$. Two isotopes are listed for B , C , N and O , since separate excitation functions are available for each. We do not list excitation functions for ${}^4\text{He}$ energies > 10 MeV. The following brief comments pertaining to narrow resonances, additional references, experimental considerations, etc., apply to the individual cases.

The measured cross section for ${}^9\text{Be}$ becomes non-Rutherford below the energy regions reported. However, the cross section is nearly Rutherford for the smooth region $\Delta E_{\text{lab}}^{\text{nr}} = 2.2 - 3.5$ MeV [11]. Additional information may be obtained from [14], which

contains angular distributions at $E_{lab} = 8.75, 9.35$ and 10.15 MeV. A strong isolated resonance at $E_{lab} = 5.1$ MeV, < 100 keV wide and 33 times Rutherford may be used for depth profiling.

The ^{10}B cross section is non-Rutherford for the entire reported region [15]. For $\theta_{lab} = 67.9^\circ$, the cross section exceeds Rutherford by about 30%, for $\Delta E_{lab}^{nr} = 1.4-2.0$ MeV; for $\theta_{lab} = 162.0^\circ$, it exceeds Rutherford by about 100%, $\Delta E_{lab}^{nr} = 2.6-2.8$ MeV. Measured angular distributions are available for $E_{lab} = 5$ and 7 MeV [16].

The ^{11}B cross section is non-Rutherford for the entire reported region [17,18]. The cross section exceeds Rutherford by about 50% for $E_{lab} = 2.1-2.5$ MeV, but is nearly Rutherford for $E_{lab} = 2.8-3.0$ and $3.3-3.5$ MeV (for $\theta_{lab} = 150.8^\circ$).

For ^{12}C , excitation functions covering individual resonances are available for $E_{lab} = 3.585$ MeV [26,27]; $E_{lab} = 5.245$ MeV [28,29]; $E_{lab} = 10.2$ MeV [30]. Measured angular distributions are available for $E_{lab} = 5$ and 6 MeV [31]. Data were taken but excitation functions of BS interest were not shown (resonance parameters were tabulated) for $\Delta E_{lab} = 2.8-6.6$ MeV, $\theta_{lab} = 165^\circ$ [32]; $\Delta E_{lab} = 1.0 - 6.6$ MeV, $\theta_{lab} = 163^\circ$ [33]; $\Delta E_{lab} = 3 - 10$ MeV, $\theta_{lab} = 90^\circ$ [34]. Calculated fits to earlier data provided resonance parameters for $\Delta E_{lab} = 2.8-3$ MeV [35-38]. The well-known strong resonance at $E_{lab} = 4.26$ MeV has been used extensively for depth profiling [39,40]. For high energy ^4He BS, ^{12}C serves as an excellent substrate; it does not generate reaction products which interfere with other BS peaks for ^4He energies < 5 MeV, at least.

A strong resonance in ^{13}C at $E_{lab} = 2.75$ MeV and ~ 20 keV wide may be used for depth profiling [41].

For ^{14}N , there are narrow, shallow resonances at $E_{lab} = 1.533, 1.620, 2.165$ MeV [43,47] that may be ignored for BS purposes, so the ^{14}N cross section is nearly Rutherford up to $E_{lab} = 2.3$ MeV. A narrow isolated resonance at $E_{lab} = 3.576$ MeV, width < 5 keV, and strength 7 times Rutherford, has been used for depth profiling [48]; this peak may also be used for energy calibration. There is a proton peak from (α, p) which appears in the BS spectra (for $E_{lab} > 4.0$ MeV) which must be subtracted [45].

The ^{15}N cross section has a large dip at $E_{lab} = 1.878$ MeV [49].

For ^{16}O , the $\Delta E_{lab} = 8.1-9.1$ MeV region has been recently used to enhance the sensitivity for detection of O in superconducting films by a factor of ~ 25 over Rutherford [4,7,59]. The well-known strong 3.045 MeV resonance has been used extensively for depth profiling [60,61]. This resonance region has even been incorporated in simulation programs [62-64] and used to analyze oxygen in high Z oxides [63]. The resonance energy has been

reported as $(3.034 \pm 0.005)\text{MeV}$ [6], $3.045 \pm 0.010\text{MeV}$ [51], $(3.042 \pm 0.003)\text{MeV}$ [65], $(3.039 \pm ?)\text{MeV}$ [62] and $(3.0359 \pm ?)\text{MeV}$ [66] and $(3.0361 \pm ?)\text{MeV}$ [67]. Measured angular distributions are available at 100keV intervals between $E_{lab} = 4.4$ and 4.9MeV [68]. Also, see [69].

For ^{18}O , there are no smooth regions suitable for BS work in the region $\Delta E_{lab}^{nr} = 2.4\text{-}5\text{MeV}$.

Our preliminary measurements indicate that the ^{19}F cross section is nearly Rutherford for $\Delta E_{lab}^{nr} = 2.9\text{-}3.05\text{MeV}$. It is unlikely that ^4He BS measurements with $E_{lab} > 4\text{MeV}$ will yield useful information; above this energy the ^{19}F BS peak splits into three separate peaks. The two extra peaks are presumably due to inelastic scattering from the two states at 110 and 198keV in excitation [73]. Measured angular distributions are also available [74].

The ^{20}Ne cross section, except for a few weak resonances between $E_{lab} = 2.5\text{-}2.7\text{MeV}$ is effectively Rutherford up to 2.8MeV .

We have found no excitation functions for ^{23}Na for $E_{lab} < 10\text{MeV}$.

The ^{24}Mg cross section is not Rutherford above $E_{lab} = 3.2\text{MeV}$, but the authors [76] state that the cross section is "smooth" below 3.2MeV . See also [81]. There is a strong (~ 5 times Rutherford), narrow ($\sim 15\text{keV}$) isolated resonance that may be used for depth profiling at $E_{lab} = 4.79\text{MeV}$ [76].

Except for a small dip near 3.6MeV , the ^{27}Al cross section is nearly Rutherford from 0.6 to 4.0MeV [52,82]. Angular distributions for $E_{lab} = 8.75$, 9.35 and 10.15MeV have also been reported [83]. We have observed that materials containing Al give spurious BS signals (probably proton peaks) in the region just below the Fe edge when $E_{lab} > 3.5\text{MeV}$. Hence, Al compounds are not good substrates for high energy ^4He BS.

The best cross section data [84] for ^{28}Si have never been published in the open literature. Also, see [85]. The higher energy data [86] are of limited value for BS use: the data were taken at 100 keV intervals in a region of high resonance density. We observe no spurious signals above the Si edge for $E_{lab} < 5\text{MeV}$. However, the rapid oscillations in the Si cross section for $E_{lab} > 4.5\text{MeV}$ may interfere with observation of signals from elements lighter than Si.

The ^{31}P excitation curves [87] are of limited use for BS because the magnitude of the cross sections are not given. Angular distributions at $E_{lab} = 4.0$, 4.75 , 5.0 , 5.2 and 5.5MeV [88] indicate that the ^{31}P cross section is Rutherford up to at least $E_{lab} = 4.0\text{MeV}$.

We have found no excitation functions for ^{32}S for $E_{\text{lab}} < 10\text{MeV}$. However, angular distributions at E_{lab} 3.3, 4.0 and 5.0MeV indicate that ^4He backscattering by ^{32}S is nearly Rutherford for $E_{\text{lab}} < 5\text{MeV}$ [89].

We have found no information on $^4\text{He} - ^{35}\text{Cl}$ or $^4\text{He} - ^{37}\text{Cl}$ scattering for $E_{\text{lab}} < 10\text{MeV}$.

The ^{40}Ar cross section is Rutherford for $E_{\text{lab}} < 4.7\text{MeV}$.

The ^{39}K cross section is non-Rutherford over the observed region [90].

The high resonance density in the ^{40}Ca cross section for $E_{\text{lab}} > 6\text{MeV}$ almost precludes the use of non-Rutherford BS for Ca analysis. For measured angular distributions and additional $^4\text{He} - ^{40}\text{Ca}$ excitation functions, see [92].

3. Conclusions

We have surveyed the experimental information on ^4He BS cross sections for light elements (^9Be to ^{40}Ca) for ^4He energies 2-10MeV. There are large variations in the extent and quality of the data for the different elements. If the goal is to produce an accurate set of measured non-Rutherford cross sections for use in ion beam analysis, considerable work remains to be done regarding cross section measurement. Much of the cross section material is available in graphical form only [10]; it is usually not possible to read accurate cross section values from the small graphs. Presumably, one should be able to calculate the cross sections of interest using the tabulated resonance parameters, but the frequent lack of agreement shown in the papers themselves, between the calculated curves and the experimental data, does not inspire confidence in this procedure. Further, some recent cross section measurements do not appear to be in agreement with earlier measurements [6]. As matters now stand, the graphical data surveyed herein is frequently used for guidance in selection of the energy region to be used; the cross section is then measured over the small region of immediate interest, but the result is never reported. Although lack of space precludes critical evaluation of the cross section data, we regard only the O and C data as presently acceptable for general use in ion beam analysis. This may be related to the fact that recent cross section data for these elements has been reported [5,6,7] in tabular form: this practice should be encouraged.

Acknowledgements

Contributions to this research by P. Stoss, M. D. Ashbaugh, B. Dezfouly-Arjomandy and Z. Lin are gratefully acknowledged; we particularly thank B. Dezfouly-Arjomandy for his assistance in gathering the references. We thank C. Dunford and S. Pearlstein for assistance in obtaining references from the National Nuclear Data Center at Brookhaven National Laboratory. This work was partially supported by the Arizona Research Laboratories, the Optical Data Storage Center and by the Air Force Office of Scientific Research (University Research Initiative Program).

References

1. W.-K. Chu, J. W. Mayer, and M.-A. Nicolet, Backscattering Spectrometry (Academic Press, New York, 1978).
2. J. A. Leavitt, Nucl. Instr. Meth. B24/25 (1987) 717; J. A. Leavitt and L. C. McIntyre, Jr., in High Energy and Heavy Ion Beams in Materials Analysis, eds. J. R. Tesmer, C. J. Maggiore, M. Nastasi, J. C. Barbour, and J. W. Mayer (Materials Research Society, Pittsburgh, 1990), p. 129.
3. J. C. Davis, Nucl. Instr. Meth. B40/41 (1989) 705; J. L. Duggan, F. D. McDaniel, S. Matteson, D. E. Golden, J. M. Anthony, B. Gnade, and J. A. Keenan, *ibid.*, B40/41 (1989) 709; C.-C. Sun, C.-R. Lu, Z.-Y. Fe, D.-S. Yuan, and F. Yang, *ibid.*, B40/41 (1989) 718; G. S. Was, and R. H. Rotberg, *ibid.*, B40/41 (1989) 722.
4. J. A. Martin, M. Nastasi, J. R. Tesmer, and C. J. Maggiore, Appl. Phys. Lett. 52 (1988) 2177.
5. J. A. Leavitt, L. C. McIntyre, Jr. P. Stoss, J. G. Oder, M. D. Ashbaugh, B. Dezfouly-Arjomandy, Z.-M. Yang, and Z. Lin, Nucl. Instr. Meth. B40/41 (1989) 776.
6. J. A. Leavitt, L. C. McIntyre, Jr., M. D. Ashbaugh, J. G. Oder, Z. Lin, and B. Dezfouly-Arjomandy, Nucl. Instr. Meth. B44 (1990) 260.
7. K. M. Hubbard, J. A. Martin, R. E. Muenchhausen, J. R. Tesmer, and M. Nastasi, in High Energy and Heavy Ion Beams in Materials Analysis, eds. J. R. Tesmer, C. J. Maggiore, M. Nastasi, J. C. Barbour, and J. W. Mayer (Materials Research Society, Pittsburgh, 1990), p. 165.
8. Results of preliminary measurements in this laboratory.
9. M. Bozoian, Bull. Am. Phys. Soc. 35 (1990) 1694.
10. R. A. Jarjis, Nuclear Cross Section Data for Surface Analysis (Department of Physics, University of Manchester, 1979), unpublished.
11. J. D. Goss, S. L. Blatt, D. R. Parsignault, C. D. Porterfield, and F. L. Riffle, Phys. Rev. C7 (1973) 1837; J. D. Goss, thesis, Ohio State University, 1970.
12. Z. A. Saleh, F. Machali, I. I. Bondouk and D. A. Darwish, Ann. Phys. (Leipzig) 31 (1974) 76.
13. R. B. Taylor, N. P. Fletcher, and R. H. Davis, Nucl. Phys. 65 (1965) 318.
14. F. P. Brady, J. A. Jungerman, and J. C. Young, Nucl. Phys. A98 (1967) 241.
15. T. Mo and H. R. Weller, Phys. Rev. C8 (1973) 972.

16. P. David, J. Debrus, H. Mommsen, and A. Riccato, Nucl. Phys. A182 (1972) 234.
17. J. J. Ramirez, R. A. Blue, and H. R. Weller, Phys. Rev. C5 (1972) 17.
18. W. R. Ott and H. R. Weller, Nucl. Phys. A198 (1972) 505.
19. R. W. Hill, Phys. Rev. 90 (1953) 845.
20. C. M. Jones, G. C. Phillips, R. W. Harris, and E. H. Beckner. Nucl. Phys. 37 (1962) 1.
21. J. W. Bittner and R. D. Moffat, Phys. Rev. 96 (1954) 374.
22. T. P. Marvin and P. P. Singh, Nucl. Phys. A180 (1972) 282; T. P. Marvin, thesis. Indiana University, 1971.
23. Z. Zhou, Y. Qiu, G. Zhao, X. Gu, L. Pan, J. Tang, and F. Yang, in High Energy and Heavy Ion Beams in Materials Analysis, eds. J. Tesmer, C. J. Maggiore, M. Nastasi, J. C. Barbour, and J. W. Mayer (Materials Research Society, Pittsburgh, 1990), p. 153.
24. J. M. Morris, G. W. Kerr, and T. R. Ophel, Nucl. Phys. 112 (1968) 97.
25. T. R. Ophel, Ph. Martin, S. D. Cloud, and J. M. Morris, Nucl. Phys. A176 (1971) 609; Ph. Martin and T. R. Ophel, Nucl. Phys. A202 (1973) 257.
26. A. D. Frawley, F. D. Fox, K. W. Kemper, and L. C. Dennis, Phys. Rev. C 25 (1982) 2935.
27. M. A. Kovash, R. W. Lourie, W. Pugh, C. E. Hyde-Wright, D. G. Machlenski, H. R. Suites, J. C. Brown, and R. G. Syler, Phys. Rev. C 31 (1985) 1065.
28. F. Brochard, P. Chevallier, D. Disdier, V. Rauch, and F. Scheibling, J. Physique 36 (1975) 113.
29. J. D. Larson and T. A. Tombrello, Phys. Rev. 147 (1966) 760.
30. J. J. Ramirez and E. M. Bernstein, Nucl. Phys. A173 (1971) 207.
31. C. W. Wang, G. C. Kiang, L. L. Kiang, G. C. Jon and E. K. Lin, J. Phys. Soc. Japan 51 (1982) 3093.
32. G. J. Clark, D. J. Sullivan, and P. B. Treacy, Nucl. Phys. A110 (1968) 431.
33. R. Plaga, H. W. Becker, A. Redder, C. Rolfs, and H. P. Trautvetter, and K. Langanke, Nucl. Phys. A465 (1987) 291.
34. M. D. Bruno, I. Massa, A. Uguzzoni, G. Vannini, E. Verondini, and A. Vitale, Il Nuovo Cimento 27 (1975) 1.
35. G. J. Clark, Aust. J. Phys. 22 (1969) 289.
36. T. Terasawa, M. Tanifuji, and O. Mikoshiba, Nucl. Phys. A203 (1973) 225.

37. N. Z. Darwisch, K. A. Gridnev, E. F. Hefter, and V. M. Smejonov, *Il Nuovo Cimento* 42A (1977) 303.
38. Y. Suzuki, T. Ando, and B. Imanishi, *Nucl. Phys.* A295 (1978) 365.
39. M. Östling, C. S. Peterson, and G. Possnet, *Nucl. Instr. Meth.* 213 (1983) 439.
40. S. H. Sie, D. R. McKenzie, G. B. Smith, and C. G. Ryan, *Nucl. Instr. Meth.* B15 (1986) 632.
41. B. K. Barnes, T. A. Belote, and J. R. Risser, *Phys. Rev.* 140 (1965) B 616.
42. G. W. Kerr, J. M. Morris and J. R. Risser, *Nucl. Phys.* A110 (1968) 637.
43. E. A. Silverstein, S. R. Salisbury, G. Hardie, and L. D. Oppliger, *Phys. Rev.* 124 (1961) 868.
44. D. F. Herring, Ren Chiba, B. R. Gasten, and H. T. Richards, *Phys. Rev.* 112 (1958) 1210.
45. D. F. Herring, *Phys. Rev.* 112 (1958) 1217.
46. E. Kashy, P. D. Miller, and J. R. Risser, *Phys. Rev.* 112 (1958) 547.
47. H. B. Mak, G. T. Ewan, H. C. Evans, J. D. MacArthur, W. McLatchie, and R. E. Azuma, *Nucl. Phys.* A343 (1980) 79; H. C. Evans, G. T. Ewan, J. R. Leslie, J. D. MacArthur, H. B. Mak, W. McLatchie, R. C. Turnock and M. B. Woods, *Nucl. Instr. and Meth.* 192 (1982) 143.
48. F. L. Freire, Jr., B. K. Patnaik, C. V. Barros Leite, J. R. Baumivol, and W. H. Schreiner, *Nucl. Instr. Meth.* B40/41 (1989) 769.
49. H. Smotrich, K. W. Jones, L. C. McDermott, and R. E. Benenson, *Phys. Rev.* 122 (1961) 232.
50. T. Mo and H. R. Weller, *Nucl. Phys.* A198 (1972) 153.
51. J. R. Cameron, *Phys. Rev.* 90 (1953) 839.
52. J. A. Leavitt, P. Stoss, D. B. Cooper, J. L. Seerveld, L. C. McIntyre, Jr., R. E. Davis, S. Gutierrez, and T. M. Reith, *Nucl. Instr. Meth.* B15 (1986) 296.
53. R. A. Jargis, *J. Radioanal. Chem.* 43 (1979) 311.
54. M. W. Buser, *Helv. Phys. Act.* 54 (1981) 339.
55. L. C. McDermott, K. W. Jones, H. Smotrich, and R. E. Benenson, *Phys. Rev.* 113 (1960) 175.
56. O. Häusser, A. J. Ferguson, A. B. McDonald, I. M. Szöghy, T. K. Alexander, and D. L. Disdier, *Nucl. Phys.* A179 (1972) 465.
57. J. John, J. P. Aldridge, and R. H. Davis, *Phys. Rev.* 181 (1969) 1455.
58. W. E. Hunt, M. K. Mehta, and R. H. Davis, *Phys. Rev.* 160 (1967) 782.

59. S. Wu, H. Cheng, C. Zhang, X. Yao, G. Zhao, F. Yang, and Z. Hua, Nucl. Instr. Meth. B45 (1990) 227.
60. G. Mezey, J. Gyulai, T. Nagy, E. Kótai, and A. Manuaba, Ion Beam Surface Layer Analysis, edited by O. Meyer, G. Linker, and F. Käppeler (Plenum Press, New York, 1976) p. 303.
61. G. Mezey, E. Kótai, P. Révész, A. Manuaba, T. Lohner, J. Gyulai, M. Fried, Gy. Vizbelethy, F. Pasziti, G. Battistig, and M. Somogyi, Act. Phys. Hung. 53 (1985) 39.
62. P. Berning and R. E. Benenson, Nucl. Phys. Meth. B36 (1989) 335.
63. B. Blaspain, P. Revesy, L. R. Doolittle, K. H. Purser, and J. W. Mayer, Nucl. Instr. Meth. B34 (1988) 459.
64. L. R. Doolittle, in High Energy and Heavy Ion Beams in Materials Analysis, eds. J. R. Tesmer, C. J. Maggiore, M. Nastasi, J. C. Barbour, J. W. Mayer (Materials Research Society, Pittsburgh, 1990), p. 175.
65. Z. L. Wang, J. F. M. Westendorp, and F. W. Saris, Nucl. Instr. Meth. 211 (1983) 193.
66. S. H. Sie, D. R. McKensie, G. B. Smith and C. G. Ryan, Nucl. Instr. Meth. B15 (1986) 525.
67. J. D. MacArthur, H. C. Evans, J. R. Leslie and H.-B. Mak, Phys. Rev. C22 (1980) 356.
68. M. W. Buser, Helv. Phys. Acta 54 (1981) 439.
69. H. T. Richards, G. Caskey, J. H. Billen, S. R. Riedhauser and D. J. Stech, Phys. Rev. C29 (1984) 2332; G. Caskey *ibid.* C31 (1985) 717.
70. D. Powers, J. K. Blair, J. L. C. Ford, Jr., and H. B. Willard, Phys. Rev. 134 (1964) B1237.
71. S. Gorodetzky, M. Port, J. Graff, J. M. Thirion, and G. Chouraqui, J. Physique 29 (1968) 271.
72. J. Cseh, E. Koltay, Z. Máté, E. Somorjai, and L. Zolnai, Nucl. Phys. A413 (1984) 311; L. Zolnai, E. Koltai, A. Mathe, I. Chekh and E. Somorjai, Izv. Akad. Nauk. SSSR, Ser. Fiz. 44 (1980) 2281.
73. F. Ajzenberg-Selove and T. Lauritsen, Nucl. Phys. 11 (1959) 1.
74. W. A. Schier, G. P. Couchell, J. J. Egan, P. Harihar, S. C. Mathur, A. Mittler, and E. Sheldon, Nucl. Phys. A266 (1976) 16.

75. E. Goldberg, W. Haberli, A. I. Galonsky, and R. A. Douglas, Phys. Rev. 93 (1954) 799.
76. C. Cseh, E. Koltay, Z. Máté, E. Somerjai, and L. Zolnai, Nucl. Phys. A385 (1982) 43.
77. J. A. Weinman, L. Meyer-Schutzmeister, and L. L. Lee, Jr., Phys. Rev. 133 (1964) B590.
78. S. Kaufmann, E. Goldberg, L. J. Koester, and F. P. Mooring, Phys. Rev. 88 (1952) 673.
79. P. G. Ikossi, K. A. Snover, J. L. Osborne, and E. G. Adelberger, Nucl. Phys. A319 (1979) 109.
80. S. S. So, C. Mayer-Boricke, and R. H. Davis, Nucl. Phys. 84 (1966) 641.
81. W. J. Thompson, G. E. Crawford, and R. H. Davis, Nucl. Phys. A98 (1967) 228; R. L. Schulte, Ph.D. dissertation, University of Kentucky, 1971; G. E. Crawford, J. P. Aldridge, and R. H. Davis, Bull. Am. Phys. Soc. 11 (1966) 333; E. A. Halprin, J. P. Aldridge, G. E. Crawford, and R. H. Davis, *ibid.*, 11 (1966) 832; J. L. Weil and R. L. Schulte, *ibid.* 18 (1973) 1397; R. E. Fauber, E. J. Ludwig, T. B. Clegg, E. R. Crosson, H. J. Karnowski, T. M. Mooney, and W. J. Thompson, *ibid.* 32 (1987) 1579.
82. J. R. MacDonald, J. A. Davies, and T. E. Jackman, J. Appl. Phys. 54 (1983) 1800.
83. F. P. Brady, J. A. Jungerman, and J. C. Young, Nucl. Phys. A98 (1967) 241.
84. M. K. Leung, Ph.D. dissertation, University of Kentucky, 1972.
85. M. M. Stautberg, M. Cosack, R. L. Schulte, M. K. Leung, J. L. Weil, and M. T. McEllistrem, Bull. Am. Phys. Soc. 13 (1968) 674; M. K. Leung, M. Cosack, M. T. McEllistrem, R. L. Schulte, M. M. Stautberg, and J. L. Weil, *ibid.* 14 (1969) 566; M. K. Leung, J. L. Weil, R. L. Schulte, and M. T. McEllistrem, *ibid.* 16 (1971) 601.
86. J. J. Lawrie, A. A. Cowley, D. M. Whittal, S. J. Mills, and W. R. McMurray, Z. Phys. A325 (1986) 175.
87. C. J. Umbarger, K. W. Kemper, J. W. Nelson, and H. S. Plendl, Phys. Rev. C2 (1990) 1378.
88. W. A. Scheier, B. K. Barnes, G. P. Couchell, J. J. Egan, P. Harihar, S. C. Mathur, A. Mittler, and E. Sheldon, Nucl. Phys. A254 (1975) 80.
89. J. P. Aldridge, G. E. Crawford, and R. H. Davis, Phys. Rev. 167 (1968) 1053.
90. D. Frekers, R. Santo and K. Langanke, Nucl. Phys. A394 (1983) 189.

91. J. John, C. P. Robinson, J. P. Aldridge, and R. H. Davis, Phys. Rev. 177 (1969) 1755.
92. A. E. Bisson and R. H. Davis, Phys. Rev. Lett. 22 (1969) 542; D. Frekers, H. Eickhoff, H. Löhner, K. Poppensieker, R. Santo and C. Wiyorek, Z. Phys. A276 (1976) 317; A. Chatterjee, S. Kailas, S. Saini, S. K. Gupta and M. K. Mehta, *ibid.* A317 (1984) 209. J. P. F. Sellschop, A. Zucchiatti, L. Mirman, M. Z. I. Gering and E. DiSalvo, J. Phys. G13 (1987) 1129.

Table 1
 Survey of measured excitation functions for backscattering of ^4He by the light elements.

Target	Ref.	Excit. Reg. $\Delta E_{\text{lab}}(\text{MeV})$	BS Angle (max) $\theta_{\text{lab}}^{\text{max}}(\text{Deg})$	Smooth Regions $\Delta E_{\text{lab}}^{\text{nr}}(\text{MeV})$	Thres. $E_{\text{lab}}^{\text{nr}}(\text{MeV})$
^9Be	11	1.7-6.3	157.3	2.2-3.5	(1.4)
	12	1.4-2.5	145.4	—	
	13	6-20	136.0	—	
^{10}B	15	2.0-4.3	162.0	2.6-2.8	(1.7)
		1.4-2.0	67.9	1.4-2.0	
^{11}B	17	2.1-3.9	150.8	2.1-2.5	(1.7)
				2.8-3.0	
				3.3-3.5	
^{12}C	18	4-8	150.0	—	2.2
	19	0.5-4.0	166.6	3.6-4.0	
	5	1.6-5.0	170.5	3.6-4.0	
	20	2.5-4.8	159.9	3.6-4.0	
				4.4-4.8	
	21	4.0-7.6	166.6	4.4-5.2	
				6.2-6.8	
	22	4.0-13.3	148.9	4.4-5.2	
				6.2-6.8,	
				8.3-8.7	
	23	5.9-6.6	165	6.2-6.5	
	24	6.6-8.5	167	—	
	25	8.5-10.5	167	—	
^{13}C	41	2.0-3.5	165.0	2.9-3.1	(2.0)
	42	3.5-6.5	165.0	—	
^{14}N	43	1.0-2.5	166.1	—	(2.2)
	44,45	2.0-3.8	167.2	3.2-3.5	
^{15}N	46	2.7-4.7	163.8	3.2-3.5	(2.2)
	49	1.75-5.5	165.2	2.7-2.8	
				3.3-3.5	
				5.35-5.45	
^{16}O	50	3.8-4.8	166.2	—	2.3
	51	1-4	164.1	3.5-3.8	
	52	1.5-5.0	170	3.5-3.8	
	6	1.8-5.0	170.5	3.5-3.8	
	53	2.8-3.6	165	—	
	54	3.5-4.9	161	3.5-3.8	
				4.0-4.8	
	55	3.7-6.5	165.3	3.5-3.8	
			4.0-4.8		
			5.6-5.9		

Table 1 (cont.)

Target	Ref.	Excit. Reg. $\Delta E_{lab}(\text{MeV})$	BS Angle (max) $\theta_{lab}^{max}(\text{Deg})$	Smooth Regions $\Delta E_{lab}^{nr}(\text{MeV})$	Thres. $E_{lab}^{nr}(\text{MeV})$	
^{16}O	56	5-11	177.4	5.6-5.9		
				8.5-8.8		
	57	5-12.5	165.6	5.6-5.9		
				8.5-8.8		
	^{18}O	23	5.5-6.5	165	5.6-5.9	
		58	5.8-10	158.6	8.5-8.8	
4,7		8.1-9.1	166	8.5-8.8		
59		8.1-9.2	160	8.5-8.8		
70		2.4-3.5	160.1	—	(2.5)	
^{19}F	72	1.5-3.7	170	2.9-3.05	2.5	
				—	(3.0)	
^{20}Ne	75	2.4-4.0	167.3	—	(3.3)	
^{23}Na	—	—	—	—	(3.5)	
^{24}Mg	76	3.2-3.9	162.5	3.6-3.75		
	76	4.2-4.9	167.5	4.35-4.45		
	77	3.2-3.9	164.6	3.6-3.8		
	78	3.2-4.0	164	3.6-3.8		
	79	5.9-6.25	165	—		
	80	8-16	143.8	—		
^{27}Al	52	1.8-5.0	170	3.6-4.0	3.6	
	82	0.6-2.2	150	—		
^{28}Si	84	2.0-6.0	165.1	2.0-3.7	3.7	
	86	5-12	168.2	—		
^{31}P	87	6.4-7	172.5	—	(4.3)	
^{32}S	—	—	—	—	(4.6)	
$^{35,37}\text{Cl}$	—	—	—	—	(4.8)	
^{40}Ar	52	1.8-4.7	170	—	(5.1)	
^{39}K	90	6.0-9.2	175.5	—	(5.3)	
^{40}Ca	7	2.2-8.8	166	—	5.7	
	90	4.4-9.1	175.0	—		
	91	5-12	175.7	—		

A - Optical and microstructural properties of hafnium dioxide thin films

J. P. Lehan, Y. Mao, B. G. Bovard, and H. A. Macleod

Summary

We have applied a variety of analytical tools to educe the compositional and morphological changes experienced by thin films of hafnium dioxide deposited under a variety of conditions. Surface analytical techniques include scanning electron microscopy, transmission electron microscopy, electron diffraction, (Rutherford) backscattering spectrometry, and x-ray photoelectron spectroscopy. The results from these measurements are correlated with the observed optical properties. Electron diffraction reveals that films deposited below 300° C are amorphous and spectrophotometry uncovers a small negative optical inhomogeneity. The refractive index and inhomogeneity are strongly influenced by the oxygen backfill present during film condensation. Ion-assisted deposition (IAD) removes the optical inhomogeneity, increases the refractive index, and eliminates the air-to-vacuum spectral shift observed in films deposited without IAD. In addition, low energy IAD is found to increase the refractive indices of the films without affecting the optical inhomogeneity. This is explained by the preferential sputtering of hydroxide from the growing film surface by the low energy ions.

Submitted to Thin Solid Films, November 1990.

A - Optical and microstructural properties of hafnium dioxide thin films

J. P. Lehan[†], Y. Mao^{*}, B. G. Bovard, and H. A. Macleod

Optical Sciences Center

University of Arizona

Tucson, AZ 85721

1. Introduction

The optical properties of HfO₂ thin films have been investigated by a number of authors.^{1,2,3,4} A number of these studies^{1,3,4} emphasize the ultraviolet transparency of HfO₂ over its sister compound ZrO₂. The differences in physical properties between these compounds make HfO₂ an attractive alternative to ZrO₂ for optical coatings in the visible and infrared as well. Hafnium dioxide's ultraviolet transparency comes without sacrificing transparency in the near to mid-infrared

[†]Dr. Lehan is presently with Optical Coating Laboratory, Inc.; 2789 Northpoint Parkway, Santa Rosa, CA 95407. ^{*} Dr. Mao is presently with OpCo, 704 River Street, Fitchburg, MA 01420. At the time the work was performed all authors were with the Optical Sciences Center.

region. The high refractive index (about 2 in the visible⁶), along with excellent chemical and thermal stability and high melting point (2900° C), make HfO₂ an attractive candidate for optical coatings.

We employed an arsenal of characterization techniques in this study including backscattering spectrometry, spectrophotometry, scanning electron microscopy (SEM), transmission electron microscopy (TEM), electron diffraction, and x-ray photoelectron spectroscopy (XPS). Each of these techniques is useful in uncovering particular aspects of the film microstructure. Together, they can build a complete understanding of the relationship between film microstructure and deposition environment.

2. Experimental Method

The films in our study were deposited at the Thin Films Laboratory of the Optical Sciences Center in a Balzers BAK 760 box coater illustrated elsewhere. The 0.81 m³ vacuum chamber is evacuated by a rotary vane pump assisted by a Roots blower to pressures of 5×10^{-2} mbar and then cryopumped to pressures as low as 4×10^{-7} mbar. Most of the work reported here was performed at base pressures of $\sim 8 \times 10^{-7}$ mbar while the work performed at 300° C had pressures in the low 10^{-6} mbar range.

Cerac evaporation grade hafnium dioxide containing 0.22-1.3% Zr by weight (0.17 to 0.99 atomic percent) was electron beam evaporated from a molybdenum crucible liner. The $\frac{1}{8}$ - $\frac{1}{2}$ inch pieces were crushed to 1-2 mm in a dedicated mortar and pestle. We found that this resulted in a smooth surface on the melt in

the crucible liner which improved the stability of the evaporation rate.

A quartz crystal oscillator monitored the condensation rate and the accumulated thickness. This oscillator is interfaced to a microprocessor-based control system which adjusts the power to the electron beams to maintain a constant condensation rate.

The chamber could be heated up to 300° C by four quartz heaters mounted above the substrate rack. A thermocouple mounted on a baffle at the rear of the chamber and below the level of the substrate rack monitored the chamber temperature. A spot check revealed that the temperature anywhere on the substrate rack varied only about 3° C from the thermocouple reading at the baffle when the quartz heaters were holding the chamber at an elevated temperature (200° C). We recognize that electron beam sources are a major source of uncontrollable chamber heating. An electron beam source can heat the chamber at a rate of about 5° C/min from room temperature up to roughly 150° C. Above 150° C this heating rate is reduced until at 300° C an equilibrium between electron beam heating and chamber losses is reached.

An undesirable side effect of this electron beam induced heating is outgassing of the chamber walls. From ambient to 100° C the base pressure initially increases by two to three orders of magnitude. This effect is transitory, however, so we outgassed the chamber for 3-4 hours prior to film deposition at a temperature exceeding the maximum expected during deposition. The base pressures quoted above are the values after this outgassing procedure and thus give a fair representation of the residual gas pressure in the chamber during deposition.

The residual gases in the chamber were analyzed by a quadrupole mass spectrometer mounted before the gate valve of our system. Between 60 and 80% of the

residual gas was comprised of water vapor, with the remainder identified as nitrogen, oxygen, and various organics, in order of abundance.

Additional gas could be added to the chamber through an automatic metering valve mounted in the side of the chamber. This valve is interfaced to the chamber's Bayard-Alpert pressure gauge and automatically adjusts the gas flow rate to maintain a constant gauge reading. The Bayard-Alpert gauge's sensitivity varies with gas species. We compensated for this effect by employing correction factors provided by the gauge manufacturer.

For ion-assisted deposition, a Commonwealth Scientific Corporation 3-cm aperture ion source was mounted in the center of the chamber on a mount with two axes of adjustment. The ion source is of a Kaufman hot-cathode design.⁷ The ion gun grid-to-substrate distance was typically 38 cm but was occasionally moved as close as 30 cm to increase the ion current density at the substrate. We employed two different extraction grid assemblies during the course of this study depending upon the beam voltage regime in which we were operating. For beam voltages above 200 V we mounted a dual pyrolytic graphite grid assembly. Below 200 V, a single, grounded nickel grid replaced the dual grid assembly. Both the cathode and neutralizer filaments were tungsten.

The ion current density striking the substrates was measured using a shielded Faraday cup arrangement which could be rotated into the sample position prior to and after deposition. A bias of -45 V repelled the neutralizing electrons and allowed measurement of the positive ions. Measurement of the ion current density before and after the deposition allowed us to estimate the uncertainty in the ion current density at the substrate.

We employed an assortment of substrates for the various post-deposition characterization techniques. Spectrosil B grade synthetic fused silica was chosen as the substrate for near-ultraviolet, visible, and near-infrared transmittance measurements because of its excellent near-ultraviolet transparency, good refractive index stability from sample to sample, and known dispersion.⁸ Graphite acted as the substrate for backscattering spectrometry and XPS samples. Silicon served as the SEM substrate. Finally, amorphous carbon mounted on copper grids performed the functions of TEM and electron diffraction substrate.

2.1 Deposition Conditions

We investigated a number of deposition techniques to produce thin films of HfO_2 that had both good optical and environmental properties. They were as follows:

2.1.1 Conventional Deposition (CD)

This deposition process consisted of electron-beam evaporation of HfO_2 in a hard vacuum (only residual gases present). The evaporant stream was approximately normally incident on the substrates in this and all subsequent work. The initial chamber temperature was about 100°C and typically rose about 40°C during deposition. We utilized electron beam voltages of 6 and 11 kV to find optimal evaporation conditions for the starting material. A summary of the CD deposition conditions is outlined in Table I. At an electron beam voltage of 11 kV, 1.1 nm/s was the only rate at which the resultant film approached optical quality. By

contrast, at 6 kV, 0.6 nm/s produced films of optical quality in the visible while all the other rates resulted in films with prohibitively large absorption.

2.1.2 Reactive Deposition (RD)

This deposition process consisted of electron-beam evaporating HfO_2 with a backfill of oxygen introduced through the side of the chamber. The oxygen backfill pressure was 2.4×10^{-4} mbar for most of the RD work, but was occasionally lowered to values as low as 7.2×10^{-5} mbar. The oxygen pressure did not seem to have much effect on the absorption of the films as long as it was kept above the outgassing rate of the starting material while it was under electron beam bombardment. As in CD, we utilized electron beam voltages of 6 and 11 kV. The deposition conditions for RD films are detailed in Table II. At 11 kV, all the deposition rates seemed to provide satisfactorily low absorption; however, the rates were rather unstable. At 6 kV, we found similar results to the 11 kV case; however, *0.6 nm/s proved to be the most stable condensation rate overall and was thus selected as the rate for further investigation because its stability should improve run-to-run repeatability.*

2.1.3 Reactive Ion-Assisted Deposition (RIAD)

This deposition process consisted of electron-beam evaporation of HfO_2 with a backfill of oxygen at 1.4×10^{-4} mbar. In addition, we introduced argon gas through a metering valve as the working gas for our ion source until we reached an argon partial pressure of 6.4×10^{-5} mbar in the chamber. The argon was ionized

and accelerated by the ion source's pyrolytic graphite grid assembly to an energy of 300 eV. The ion beam impinged upon the growing film at angles of between 15-20° from the substrate normal. As mentioned above, the evaporant stream was approximately normally incident to the stationary substrates. We varied the ion current density at the substrate from 0.8-18 $\mu\text{A}/\text{cm}^2$. Oxygen was also run through the ion source as the working gas; however, due to severely reduced cathode lifetime as well as large ion current density fluctuations, oxygen RIAD was abandoned. The initial chamber temperature for RIAD was held at 100° C.

2.1.4 Low-Energy Reactive Ion-Assisted Deposition (LERIAD)

This deposition process consisted of electron-beam evaporation of HfO_2 with a backfill of oxygen. In addition, we introduced argon or xenon gas through a metering valve as the working gas for our ion source until a partial pressure of 6.4×10^{-5} mbar (8.0×10^{-5} for xenon) in the chamber was achieved. Ion energy was chosen to be 50 eV for both argon and xenon ions. Low ion energies required replacing our pyrolytic graphite grid assembly with a single, grounded Ni grid. The ions impinged upon the growing film at angles of between 15-20° from the substrate normal. We were unable to vary the ion current density for argon at 50 eV over a significant range so we held it fixed at 12 $\mu\text{A}/\text{cm}^2$ and varied the oxygen backfill pressure between 0.62 - 1.2×10^{-4} mbar. Xenon allowed more latitude in ion current density, so we fixed the oxygen backfill pressure at 1.4×10^{-4} mbar and varied the ion current density from 7.0-26.5 $\mu\text{A}/\text{cm}^2$. The initial chamber temperature for LERIAD was 100° C.

3. Optical Measurements

We obtained transmittance versus wavelength curves from a dual-beam Cary 2415 spectrophotometer. We applied the envelope technique of Manifacier, Gasiot, and Fillard⁹ to calculate the optical constants, n and k , as well as the thickness d of the films from transmittance curves alone. To interpolate the transmittance envelopes we have assumed a Cauchy dispersion relation of the form

$$T(\lambda) = A + B/\lambda^2 + C/\lambda^4, \quad (1)$$

where $T(\lambda)$ is the transmittance at wavelength λ and the coefficients A , B , and C are determined by a least squares fit to the transmittance extrema.

Manifacier, Gasiot, and Fillard's⁹ method assumes film homogeneity. This is not normally the case for the HfO_2 films we considered, so we have added a simple extension to their method to account for inhomogeneities. Jacobsson¹⁰ has shown that for non-absorbing films, the differences between the index at the medium-film interface n_a and the index at the film-substrate interface n_b are small and change monotonically throughout the film, the transmittance at a quarterwave point is given by

$$T_{1/4} = \frac{4 \frac{n_a n_b}{n_1}}{\left[1 + \frac{n_a n_b}{n_1} \right]^2}, \quad (2)$$

and the halfwave transmittance is given by

$$T_{1/2} = \frac{4 \frac{n_a n_1}{n_b}}{\left[1 + \frac{n_a n_1}{n_b} \right]^2}, \quad (3)$$

where the incident medium is air ($n_0 = 1$). The quarterwave result [Eq. (2)] is in-

distinguishable from a *homogeneous* film with refractive index $\sqrt{n_a n_b}$. This geometric mean refractive index is the result calculated by Manifacier, Gasiot, and Fillard's⁹ method if the film is inhomogeneous. The halfwave result [Eq. (3)] has no homogeneous layer analog. This allows us to solve for n_a and n_b separately. This is only true if we neglect absorption. Thus we will only report inhomogeneity data sufficiently far from an absorption edge so that this approximation is good. For HfO_2 films under consideration, this is about a 600 nm or longer wavelength where the absorption is thought to be well below the noise in the measurements.

3.1 Optical Constants

The thickness of the optical samples varied from about 400 nm to 480 nm. For a 460 nm film, this means that the film is about three quarterwaves optically thick at 1200 nm. This allowed us to determine the optical constants for our HfO_2 films from the absorption edge at about 220 nm to about 1200 nm. We chose 550 nm as the primary wavelength with which to compare the refractive indices of films deposited under different conditions. The 550 nm wavelength was chosen because the absorption and dispersion are small given the fact we are measuring sufficiently far from the ultraviolet absorption edge. This wavelength is also a good single value comparator with the results of other researchers for other coating materials. Inhomogeneity data is compared at the longer wavelength of 800 nm because its calculation from transmittance data is sensitive to film absorption as mentioned above.

3.1.1 Conventional Deposition

Almost all CD films were of such poor optical quality that the assumption of weak absorption in Manifacier, Gasiot, and Fillard's⁸ method for the determination of the optical constants was violated. Only one film deposited at 0.6 nm/s with an electron-beam (e-beam) voltage of 6 kV was truly of optical quality. The film nearest to optical quality at 11 kV e-beam voltage condensed at a rate of 1.1 nm/s. Since only two deposition conditions resulted in films whose optical constants could be calculated, comparisons between films was not considered enlightening. As a result, no optical constants are reported for CD films.

3.1.2 Reactive Deposition

RD produced optical quality films in almost all cases. Figure 1 summarizes the results of varying the condensation rate while holding the oxygen backfill pressure constant at a value of 2.4×10^{-4} mbar. Most of the films have an index of about 2.01 regardless of the rate at which they condensed or of the e-beam voltage. The exceptions are 0.6 nm/s at an e-beam voltage of 6 kV and 1.1 nm/s at an e-beam voltage of 11 kV. Curiously, these are the same conditions that yielded the films of near optical quality by CD. The extinction coefficient of the RD films at 300 nm was 2×10^{-4} or less regardless of deposition rate or electron gun voltage.

The relative inhomogeneity $\Delta n/n$ is defined by the following equation:

$$\frac{\Delta n}{n} \equiv \frac{n_a - n_b}{\sqrt{n_a n_b}} \quad (4)$$

This definition implies that the relative inhomogeneity will be negative if the refractive index at the air-film interface n_a is less than the refractive index at the

film-substrate interface n_b . This is the usual situation for HfO_2 films and most other refractory oxides deposited by electron-beam evaporation.¹¹ Baumeister and Arnon³ observed that lowering the condensation rate increased the inhomogeneity of their HfO_2 films. We did not observe this trend for our RD films. Films deposited at an electron beam voltage of 6 kV were more homogeneous than at 11 kV. This may be due to the improved condensation rate stability observed at the lower electron beam voltage.

As stated in the experimental method section, we selected a deposition parameter of 6 kV e-beam voltage and a condensation rate of 0.6 nm/s for the subsequent work because the rate fixed by these settings was the most stable overall. We then varied the oxygen backfill pressure while holding the condensation rate constant. The results are plotted in Fig. 2. The extinction coefficient at 300 nm is below the limit detectable by our spectrophotometric measurements (1.5×10^{-4} for a 480 nm film) for all the films illustrated in figure 2 with the exception of the film deposited without an oxygen backfill. We see that increasing the oxygen backfill pressure reduces the refractive index. The relative inhomogeneity of these films is plotted as a function of the oxygen backfill pressure in figure 3. Although there is considerable oscillation in the data, the general trend is toward increased homogeneity as the oxygen pressure increases.

In summary, if we evaporate HfO_2 at 0.6 nm/s with a 6 kV e-beam, we find that increasing the backfill pressure of oxygen will decrease the *average* refractive index while the films approach homogeneity. It appears that increasing the oxygen pressure in the chamber has the drawback of producing a more porous film, but the advantage of producing a more homogeneous film.

3.1.3 Reactive Ion-Assisted Deposition

We pursued RIAD as a technique to improve the characteristics of our RD films. That is, we attempted to raise the refractive index and eliminate the inhomogeneity while not increasing the film absorption. As in the second half of the RD work above, we selected deposition parameters of 6 kV electron beam voltage and 0.6 nm/s condensation rate because the deposition rate at these settings was the most stable. In addition, the oxygen pressure was held at 1.4×10^{-4} mbar and the argon working gas pressure at 0.64×10^{-4} mbar. We also fixed the ion energy at 300 eV. The results for the refractive index at 550 nm as a function of the current density at the substrate are illustrated in figure 4. There is considerable spread in the calculated refractive index values; however, all the RIAD films have a higher index than the RD film with the same oxygen backfill pressure (shown as zero current density in the figure). In fact, the RIAD films have a higher index than all of the RD films but the films deposited in a hard vacuum (0 backfill pressure in figure 2). In addition, the RIAD films appear to be *homogeneous*. The extinction coefficients at 300 nm are comparable to RD films although the films deposited at ion current densities above $15 \mu\text{A}/\text{cm}^2$ begin to show absorption extending into the visible.

3.1.4 Low Energy Reactive Ion-Assisted Deposition

As we mentioned in the experimental section, we had very little latitude in the ion current density with which to bathe the substrate when we attempted LERIAD using argon as the working gas. We altered the oxygen backfill gas pres-

sure hoping that the combination of LERIAD and altering the oxygen partial pressure would cause a discernible change in our films. We found, however, that the films behaved optically as if we were not bombarding them at all. As we increased the oxygen backfill pressure the refractive index dropped in analogy to the conditions of figure 2.

With xenon as the working gas the situation improved considerably. xenon allowed us access to a much greater range of current densities than with argon. The refractive index at 550 nm as a function of the current density of 50 eV xenon ions is shown in figure 5. A clear monotonic increase of the refractive index with current density is in-

dicated. The problem, however, is that the low energy xenon ions do not affect the relative inhomogeneity $\Delta n/n$ which remains at about -0.05.

3.2 Spectral Air-to-Vacuum Shift

We have seen that non-absorbing, homogeneous films of HfO_2 can be deposited by either RD or RIAD. The RD films, however, suffer from a low index and are porous. The RIAD films, on the other hand, have a higher index and are relatively dense. These results are confirmed by air-to-vacuum shift measurements. Upon venting the chamber, the columnar microstructure of the films adsorbs atmospheric moisture.^{12,13,14} The adsorption of water vapor alters the optical thickness of the layer.¹² The physically adsorbed part of this vapor can be removed by again placing the film under vacuum.¹³ We employed a vacuum cell which could be placed into our spectrophotometer and evacuated to measure the

wavelength difference of an extremum at atmosphere and under vacuum. This measurement yields an approximate measure of the film packing density.¹²

For example, an RD film deposited at 2.4×10^{-4} mbar oxygen backfill and 0.6 nm/s condensation rate exhibited an air-to-vacuum shift of 3 nm while RIAD films did not exhibit detectable shifts. Films deposited at high temperature (300° C) or by LERIAD had intermediate air-to-vacuum shift values in the 1.5 to 2 nm range.

3.3 Fourier Transform Infrared (FTIR) Spectrometry

Samples for FTIR were deposited onto 0.5 mm Si wafers and measured on an Analect Instruments FX-6200 FTIR spectrometer with a resolution of 4 cm^{-1} . RD samples deposited at chamber temperatures ranging from 100 to 300° C exhibited absorption near $3 \mu\text{m}$ indicative of water trapped in the microstructure of the films.¹⁵ RIAD at an ion current density of $10 \mu\text{A}/\text{cm}^2$ nearly eliminated this absorption band. Knowing the thickness of our films, we were able to calculate a refractive index of 1.95 ± 0.03 at $3.9 \mu\text{m}$. All of the films measured were transparent to beyond $10 \mu\text{m}$.

3.4 Summary of Optical Results

We have seen that non-absorbing, homogeneous films of HfO_2 can be deposited by either RD or RIAD. The RD films, however, suffer from a low index and are porous. The RIAD films, on the other hand, have a higher index and are relatively dense. In addition, we have shown that LERIAD with xenon can increase

the refractive index of HfO_2 films. Finally, we have seen that the oxygen pressure during deposition has a strong effect on the resultant film's refractive index, extinction coefficient, and inhomogeneity.

4. Electron Microscopy, Electron Diffraction and Film Microstructure

We performed SEM measurements on several samples of ~ 450 nm optical thickness. We deposited the samples on Si wafers to reduce surface charging. The wafers were broken, leaving a sharp edge allowing a cross-sectional view of the film and substrate. We attached each sample to an aluminum holder with conductive paint and placed the specimen in a JEOL JSM 5200 SEM. The microscope is quoted to have a resolution of 6 nm; however, this number is strongly sample dependent. Edge field effects and surface charging of our dielectric HfO_2 specimens reduced our resolution considerably. Columnar microstructure was just resolvable, but was good enough to estimate the column diameter for at least one film deposited by RD at a rate of 0.6 nm/s with a substrate temperature of 100°C in a 2.4×10^{-4} mbar oxygen backfill. These are the conditions that led to the most porous films by RD. The column diameter under these conditions was measured to range between 50 and 100 nm. The columns for films deposited at higher temperatures or with ion assistance could not be imaged satisfactorily. We were, however, able to image the *surface* of a number of the films deposited at different temperatures and found them all to be smooth and devoid of sharp, high spatial frequency features. Such surface topography suggests the surface scattering losses for HfO_2 layers would be small.

We made TEM micrographs on a JEOL JEM 2000FX TEM with a quoted resolution of 0.14 nm. As with the SEM, this number is affected by several factors: 1) the sample thickness, 2) the composition of the specimen, and 3) the crystalline perfection of the sample.¹⁶

The practical limitation on the utility of using TEM for the direct observation of optical thin films is the sample thickness. For instance, the upper limit on the film thickness for our HfO₂ samples was 60 nm. Even at these thicknesses, however, changes in the film morphology with deposition conditions are evident. Figure 6(a) shows a RD film deposited at 0.6 nm/s on a 100° C substrate in a 2.4 x 10⁻⁴ mbar oxygen backfill. The vestiges of columnar growth are evident. Figure 6(b) shows a film deposited under the same nominal conditions as the previous film but with 300 eV argon ion assistance at an ion current density of 10 μA/cm². The effect of the ion assist is evident. Argon bombardment has resulted in the coalescing of the columns into larger conglomerates, thereby densifying the film.

The JEM 2000FX can be converted into an electron diffractometer by removing two apertures and shifting the observation plane. Thus both an image and diffraction pattern can be obtained from the same region of the film. Electron diffraction has an advantage over x-ray diffraction in that the wavelength is tunable via the De Broglie relation. In this way sub-Angström structure can be observed.

We obtained the camera constant for the microscope by measuring an Al reference film whose crystalline structure is well known.¹⁷ This allows us to determine crystalline plane spacing given the geometry of the microscope. Electron diffraction patterns obtained for RD films deposited at temperatures of 38° C and 200° C are illustrated in figure 7(a) and 7(b), respectively. Both films are quasi-

amorphous with a slightly larger crystallite size for the 200° C film indicated by the somewhat sharper ring structure. We measured a maximum crystallite diameter of 2.5 nm for a film deposited at 200° C. The diffraction patterns obtained from HfO₂ films deposited by RIAD were indistinguishable from those obtained for RD films. The average nearest neighbor distance found from diffraction patterns is 0.29±0.02 nm, which has been associated with the (111) plane of cubic HfO₂, the high temperature phase of HfO₂.¹⁸ The diffuse outer ring in the figures is due to the amorphous carbon substrate.

5. Backscattering Spectrometry

The power of backscattering spectrometry (or Rutherford backscattering spectrometry) as a quantitative analytic tool for determining the chemical composition of thin films is well known.¹⁹ A van de Graaff accelerator generates a high energy (1.892 - 3.776 MeV in this work) beam of ⁴He⁺ ions. The ions are scattered by the thin film sample in an evacuated chamber. A small detector collects the ⁴He⁺ ions backscattered by the target film at large angles nearly parallel to the incident beam. By measuring the number of scattered ⁴He⁺ ions per unit solid angle per incident ⁴He⁺ and comparing this with the known scattering cross sections, we can determine the absolute number per unit area (areal density) of each atomic constituent of the film. Thus we can determine the film composition with great precision.

Hafnium has a high density of electrons surrounding its nucleus as does the chief contaminant in our HfO₂ films, Zr. This high electron density screens the nuclear charge from the ⁴He⁺ probe beam, resulting in scattering which deviates

slightly from the Rutherford formula in the energy region above. As a consequence, we have applied the nuclear charge screening corrections of Andersen, et al²⁰ to the scattering cross section data.

We wished to address two questions concerning the composition of our HfO₂ films: 1) How do the deposition conditions affect the oxygen-to-metal ratio; i.e., the ratio $N^O / (N^{Hf} + N^{Zr})$?; and 2) How does the Zr contamination affect film properties?

5.1 Oxygen-to-Metal Ratio

5.1.1 Conventional Deposition

The majority of CD deposition rates produced films exhibiting broadband absorption in the visible. Backscattering spectrometry analysis revealed an oxygen-to-metal ratio of less than two for these films. The stoichiometric oxides of Hf and Zr are HfO₂ and ZrO₂, respectively, so we would expect the ratio $N^O / (N^{Hf} + N^{Zr})$ to be two in non-absorbing material. Thus it comes as no surprise that our CD films have oxygen-to-metal ratios less than two.

5.1.2 Reactive Deposition

For RD the situation was quite different from CD. The oxygen-to-metal ratio for RD films was *always* greater than two. This hyperstoichiometry is surprising considering no superoxides of Hf or Zr have been reported in the literature and the occurrence of superoxides becomes rare as one goes down a column of

the periodic table.²¹ Figure 8 illustrates the results for RD films condensing at a rate of 0.6 nm/s as a function of the oxygen backfill pressure. Results for chamber temperatures of 100, 200 and 300° C are illustrated. Note that the films deposited at 100° C have a larger oxygen-to-metal ratio than those deposited at higher temperatures. The film deposited at 100° C with an oxygen backfill pressure of 2.4×10^{-4} mbar had the highest oxygen-to-metal ratio, $N^O / (N^{Hf} + N^{Zr}) = 2.24 \pm 0.07$, of any film measured, although oxygen-to-metal ratios as high as 2.14 were not uncommon.

5.1.3 Reactive Ion-Assisted Deposition

RIAD films were similar to the high temperature RD films. The oxygen-to-metal ratios ranged from 2.08 to 2.12 which is within the error bars of the measurement. The argon concentration in these films ranged from 2.4 to 3.1 atomic percent. This information, combined with the optical and TEM studies, implies that RIAD within the investigated range of ion current densities affects the columnar microstructure of HfO_2 without adversely affecting the composition.

5.1.4 Low Energy Reactive Ion-Assisted Deposition

LERIAD-with-argon films resembled RD films in their composition. The oxygen-to-metal ratios fell within the range 2.08 to 2.14, a slightly greater range than for the RIAD films. Argon content in these films was quite small, sometimes below the detectable limit of the backscattering system. For LERIAD with xenon the situation was somewhat different, with xenon being detected when the ion cur-

rent density was high although about a factor of three less than the argon seen in 300 eV RIAD films with similar ion current densities.

5.2 Zirconium Contamination

The Zr contamination measured in the films ranged from 0.35 to 1.18 atomic percent. The maximum excursion in a *single coating run* was from 0.79 to 1.11 atomic percent; the typical Zr content was about 0.7 atomic percent. We were unable to establish a correlation between the order in which the layers were deposited and the Zr content, which would suggest a preferential evaporation of either ZrO_2 or HfO_2 .²²

This level of Zr contamination is insufficient to explain the variations seen in the refractive indices of the RIAD films. In addition, any variability in refractive index due to Zr content would fall within the uncertainties of our index measurement. For example, the difference in refractive indices for the two extrema in Zr content is only 0.003. This index variability is tolerable for most optical coating applications.

The effect of the Zr contamination on the extinction coefficient in the near ultraviolet is more uncertain. We would expect this extinction coefficient to be much more sensitive to Zr contamination than the refractive index; however, we were not able to establish a clear correlation. We attribute this to the poor sensitivity of our spectrophotometric measurements when compared to techniques such as calorimetry.²³ Zirconium contamination may, on the other hand, explain the variations in extinction coefficients seen for films deposited under the same nominal conditions.

6. X-ray Photoelectron Spectroscopy (XPS)

We undertook an XPS²⁴ investigation of our HfO₂ films to ascertain the chemical state of the extra oxygen observed in the majority of the films.

We measured three HfO₂ samples spanning the range of stoichiometries observed in our films as well as the starting material. We employed a Perkin-Elmer 5100 ESCA system in the Optical Materials Lab at the Optical Sciences Center. The samples were placed in a vacuum system and pumped down to the low 10⁻⁹ mbar range before the measurement. The samples were sputter-cleaned with an argon ion mill for 1 min at an angle of 70° from the sample normal to remove the thin carbon layer that accumulated on the samples during handling. The films were irradiated with Mg K α x-radiation (1253.6 eV) which has a natural linewidth of 0.7 eV (FWHM). No monochromator was employed. The x-rays impinged on the specimen at an angle of 30° from the film normal, the spot size was approximately 3 mm x 10 mm. The electron analyzer was operated with a constant pass energy.

Subsequent to measurement, we massaged the photoelectron spectra. First we subtracted x-ray satellite peaks. We then deconvolved the linewidth of the x-rays from the data and corrected for surface charging via the C 1s method. We assumed the binding energy value for C 1s to be 284.4 eV for this correction, which corresponds to the interplane C-C bond of graphite. This energy was chosen because all the thin film samples were deposited onto graphite substrates. This introduces an additional energy uncertainty in the peak position of the starting material sample of only ± 0.2 eV. Finally, we subtracted the background via the Shirley²⁵ method. Unresolved peaks were then fit with Gaussian lineshapes.

We examined four representative samples: 1) Starting material (monoclinic HfO_2) crushed to a powder with mortar and pestle and attached to a stainless steel mount with Dennison Glue Stic. The glue stick provided enough carbon for us to make the C 1s surface charging correction. 2) a substoichiometric film, $\text{N}^{\text{O}}/(\text{N}^{\text{Hf}} + \text{N}^{\text{Zr}}) = 1.84 \pm 0.05$ as determined by backscattering spectrometry, 3) a "typical" film with $\text{N}^{\text{O}}/(\text{N}^{\text{Hf}} + \text{N}^{\text{Zr}}) = 2.09 \pm 0.06$, and 4) an extremely hyperstoichiometric film with $\text{N}^{\text{O}}/(\text{N}^{\text{Hf}} + \text{N}^{\text{Zr}}) = 2.24 \pm 0.07$. It should be emphasized that the XPS analysis was performed on *exactly* the same films that were analyzed by backscattering spectrometry.

The XPS results for the four samples are summarized in Table III. The oxygen-to-metal ratio of the bulk starting material was not measured. We note that all the peaks for the thin film samples are shifted to higher binding energies than the bulk samples. This shift is larger than can be attributed to the choice of reference energy and is thought to arise from the differences in chemical environment between the amorphous films and the crystalline bulk material.²⁷

The chemical identity of the additional oxygen seen in the HfO_2 films is made most readily apparent by comparing the O 1s peaks for the various samples. The O 1s peaks for the four samples, along with their best fitting Gaussians, are shown in Figs. 9(a)-(d). Figure 9(a) illustrates the O 1s peak for the bulk material. We see that it is fit by a doublet spaced by 1.6 eV. This spacing is the same as the spacing reported by others²⁶ between O bonded as hafnium dioxide and O bonded as hafnium hydroxide, the hydroxide having the higher binding energy. The ratio of the heights of the oxide to hydroxide Gaussians is 2.6.

Figure 9(b) shows the O 1s peak for the film with an oxygen-to-metal ratio of 1.84 ± 0.05 . A single Gaussian fits the data. The FWHM Γ for the fitting Gaus-

been observed in anodic oxide formation of Hf and Zr²⁶ as well as in bulk ZrO₂.²⁸ We believe that this hydroxide formation occurs during film condensation because of the appearance of a hydrogen peak on our residual gas analyzer that does not exist prior to film deposition.

7. Conclusions

7.1 Conventional Deposition

CD films exhibit an amorphous, columnar structure. They tend to be oxygen deficient and thus show broadband absorption in the visible region of the spectrum. CD is, therefore, not a desirable method for depositing optical quality films of hafnium dioxide.

7.2 Reactive Deposition

RD films also exhibit an amorphous, columnar structure. They are oxygen rich which can be attributed to the presence of hydroxide. The presence of oxygen has the effect of 1) reducing optical absorption by satisfying hafnium dangling bonds, 2) lowering the average refractive index, and 3) altering the optical inhomogeneity. Increasing the oxygen backfill in the chamber lowers the average refractive index while also reducing the inhomogeneity of the films. The surface of RD HfO₂ films is quite smooth as indicated by SEM. This implies low surface scattering losses for these films.

RD films are of good optical quality although inhomogeneous. The inhomogeneity and refractive index are sensitive functions of the oxygen backfill pressure in the chamber. In addition, the porosity of these films makes the optical properties sensitive to humidity changes in the external atmosphere as the capillary voids between the columns capture and release atmospheric moisture. Therefore, HfO_2 films deposited by RD would not be suitable for coatings to be used in harsh environments.

7.3 Reactive Ion-Assisted Deposition

RIAD films exhibit an amorphous, dense columnar structure. Ion bombardment with argon densifies the films without introducing unwanted optical absorption if the ion current density is not too high. In addition, ion bombardment can remove the optical inhomogeneity while still maintaining a high refractive index and low absorption. The refractive index of RIAD films may, however, still be sensitive to the partial pressure of oxygen in the chamber.

We conclude that RIAD HfO_2 films would be suitable for optical coatings - even in harsh environments; however, the partial pressure of oxygen in the chamber should be controlled.

7.4 Low Energy Reactive Ion-Assisted Deposition

LERIAD with argon ions at low ion current densities was found to have little measurable effect upon our HfO_2 films and resulted in film behavior essentially the same as observed for RD.

LERIAD with xenon was quite different. We were able to extract relatively large ion current densities from our Kaufman ion source using xenon. As a result, we saw an increase in the average refractive index of these films with ion current density. Unlike RIAD, however, LERIAD did not alter the optical inhomogeneity in these films. This indicates the possibility of a mechanism for the observed refractive index increase other than the densification seen in RIAD and normally associated with IAD. Table V summarizes the LERIAD results. We see a clear increase in average refractive index with xenon ion current density; however, no significant changes occur in the relative inhomogeneity. If we examine the oxygen-to-metal ratio, on the other hand, a trend emerges. As we increase the xenon ion current density, the oxygen-to-metal ratio decreases. In addition, the extinction coefficient does not increase with ion current density. Therefore, we believe the xenon ion beam preferentially sputters hydroxyl groups from the surface of the growing film. Such behavior has been observed in other oxides under ion bombardment.²⁹ Additionally, the inclusion of xenon in the films may hinder the subsequent formation of hydroxide after deposition is complete. This results in a more dense structure within the columns of the film so that the average refractive index increases. An approximate calculation shows the radius of a hydroxide ion being between 0.12 and 0.16 nm. The radius of a xenon atom is 0.13 nm. We expect, therefore, that the presence of a xenon atom leaves no room in the HfO_2 matrix for hydroxyl ion inclusion.

We note a slight increase in optical absorption when compared to RD films. Because the absorption does not correlate with ion current density, we hypothesize that the increase in extinction coefficient is due to trace amounts of included nickel and tungsten from the ion gun grids and filaments, respectively. The con-

tamination, however, is below the 0.1 atomic percent detection level of our back-scattering spectrometry measurements for these elements.

8. General Conclusions

As we noted before, the behavior of the LERIAD films deposited with argon ion-assistance exhibited behavior analogous to RD films as we varied the oxygen backfill pressure. In fact, if we plot the LERIAD films with the lowest ion current density together with the RD films illustrated in Fig. 2 as a function of backfill oxygen pressure, Fig. 10 results. The data fall remarkably well on the line $n = 2.042 - 267.1p$, where n is the average refractive index at 550 nm and p is the oxygen backfill pressure in mbar. This suggests that the low argon ion current density coupled with the low energy (50 eV) does not measurably affect the film properties. More remarkably, the partial pressure of the argon does not seem to affect the film properties.

Thorton³⁰ has shown that the argon gas pressure in a sputtering chamber influences the microstructure of the metal films produced. Higher argon pressures resulted in more porous films. He attributed this effect to a reduction of the condensate mobility by argon adsorbed on the growing film and substrate. Such a mechanism involving oxygen may explain the trend we see in Fig. 10. The number of oxygen molecules incident on the growing film surface per unit time is given by³¹

$$3.411 \times 10^{22} p \text{ cm}^{-2} \text{ s}^{-1}, \quad (5)$$

where p is the pressure in mbar. Some fraction of these impinging oxygen molecules will stick to the surface of the growing film. If these oxygen atoms act to

limit the mobility of the condensate proportional to their number then we would expect, from Eq. (5), the mobility to be reduced with pressure. This simple model explains why the films become more porous with increasing oxygen backfill pressure. In addition, this model, along with Fig. 10, would indicate that argon has a low sticking coefficient on the HfO_2 surface of the growing film and thus does not affect the film growth. The assumption of little adsorption of argon on the growing film surface is reinforced by the fact that the largest amount of argon detected by backscattering spectrometry in any of the LERIAD films with argon bombardment was 0.05 atomic percent.

The implied linear dependence of HfO_2 's refractive index on oxygen backfill pressure has an interesting consequence. We can envision the production of an inhomogeneous refractive index profile layer by merely altering the oxygen backfill pressure in the chamber. The problem with such an approach is that the porous films which result would shift their spectral characteristics in a humid environment, as mentioned above.

We feel that HfO_2 is a promising high-index dielectric material that can be used in the near ultraviolet through the mid infrared. The surface of a HfO_2 film appears to be quite smooth and does not exhibit the polycrystalline grains seen in ZrO_2 films. This implies that the scattering losses of a HfO_2 layer should be much less than a comparable ZrO_2 layer. In addition, ion bombardment does not induce the undesirable recrystallization of the films as is seen in ZrO_2 .³² The refractive index and inhomogeneity, however, are sensitive functions of the oxygen backfill pressure and so this must be controlled carefully.

9. Acknowledgements

The authors would like to thank T.-J. Zhao and D. Olinger for their help and enlightening discussions. R. Potoff and S. Rana provided excellent technical assistance. We would also like to thank Dr. U. Gibson for access to her XPS facility and J. Watanabe and K. Cornett for their assistance with the equipment. V. Lindley greatly assisted in obtaining the TEM micrographs. In addition, Drs. J. A. Leavitt & L. C. McIntyre and their colleagues at the Ion Beam Analysis Facility at the University of Arizona provided invaluable backscattering spectrometry measurements. Finally, we wish to acknowledge the support of United Technologies Optical Systems and the Air Force Office of Scientific Research through the University Research Initiative Program.

10. References

- 1) D. Smith and P. Baumeister, *Appl. Opt.*, 18 (1979) 111.
- 2) J. P. Borgogno, B. Lazarides, and E. Pelletier, *Appl. Opt.*, 22 (1982) 4020.
- 3) P. W. Baumeister and O. Arnon, *Appl. Opt.*, 16 (1977) 439.
- 4) R. S. Sokolova, *Sov. J. Opt. Technol.*, 41 (1974) 454.
- 5) H. A. Macleod, *Thin Film Optical Filters*, Macmillan, New York, 2nd edn., 1986 p. 505.
- 6) C.-K. Hwangbo, L. J. Lingg, J. P. Lehan, H. A. Macleod, J. L. Makous, and S.-Y. Kim, *Appl. Opt.*, 28 (1989) 2779.
- 7) H. R. Kaufman and R. S. Robinson, *Operation of Broad-Beam Ion Sources*, Commonwealth Scientific Corp., Alexandria, Virginia (1984).
- 8) I. H. Malitson, *J. Opt. Soc. Amer.*, 55 (1965) 1205.
- 9) J. C. Manificier, J. Gasiot, and J. P. Fillard, *J. Phys. E: Sci. Instrum.*, 9 (1976) 1002.

- 10) R. Jacobsson in G. Haas, M. H. Francombe, and R. W. Hoffman (eds.), *Physics of Thin Films*, Vol.8, Academic Press, New York, 1975, p. 51.
- 11) J. P. Borgogno, B. Lazarides, and E. Pelletier, *Appl. Opt.*, 22 (1982) 4020.
- 12) K. Kinosita and M. Nishibori, *J. Vac. Sci. Technol.*, 6 (1960) 730.
- 13) H. K. Pulker and E. Jung, *Thin Solid Films*, 9 (1971) 57.
- 14) H. A. Macleod and D. Richmond, *Thin Solid Films*, 37 (1976) 163.
- 15) A. P. Bradford, G. Haas, and M. McFarland, *Appl. Opt.*, 11 (1972) 2242.
- 16) A. Howie in P. Busek, J. Cowley, and L. Eyring (eds.), *High-Resolution Electron Microscopy and Associated Techniques*, Oxford University Press, New York, 1988 p. 607.
- 17) R. D. Heidenreich, *Fundamentals of Transmission Electron Microscopy*, Wiley, New York, 1964.
- 18) I. A. El-Shanshoury, V. A. Rudenko, and I. A. Ibrahim, *J. Am. Ceram. Soc.*, 53 (1970) 264.

- 19) W.-K. Chu, J. W. Mayer and M. A. Nicolet, *Backscattering Spectrometry*, Academic Press, New York, 1978.
- 20) H. H. Andersen, F. Besenbacher, P. Loftager, and W. Möller, *Phys. Rev. A* 21 (1980) 1891.
- 21) F. A. Cotton, and G. Wilkinson, *Advanced Inorganic Chemistry*, 5th edn., Wiley, New York, 1988 p. 777.
- 22) M. Friz, E. Amadori, F. König, and S. M. McNally, *Proc. of the 32nd Ann. Conf. Soc. of Vac. Coaters*, St. Louis (1989) 264.
- 23) T. H. Allen, J. H. Apfel, and C. K. Carniglia, *NBS Special Publ. 541*, 1979.
- 24) K. Siegbahn, et al, *ESCA - Atomic, Molecular, and Solid State Structure Studied by Means of Electron Spectroscopy*, Uppsala, 1967.
- 25) D. A. Shirley, *Phys. Rev B*. 5 (1972) 4709.
- 26) S. Hofmann, and J. M. Sanz, *J. Trace and Micro. Tech.. 1*, (1982-83) 213.
- 27) see, for example, R. Zallen, *The Physics of Amorphous Solids*, Wiley, New York, 1983 p. 292.

- 28) H. F. Holmes, E. L. Fuller, Jr., and R. B. Gammage, *J. Phys. Chem.*, 76 (1972) 1497.
- 29) T. J. Chuang, C. R. Brundle, and K. Wandelt, *Thin Solid Films*, 53 (1978) 19.
- 30) J. A. Thornton, *J. Vac. Sci. Technol.*, 11 (1974) 666.
- 31) L. I. Maissel, and R. Glang, *Handbook of Thin Film Technology*, McGraw Hill, New York, 1983 p. I-21.
- 32) P. J. Martin, R. P. Netterfield, and W. G. Saintry, *J. Appl. Phys.*, 55 (1984) 235.

Table I: Deposition condition for conventionally deposited (CD) films.

Rate (nm/s)	T _{initial} (° C)	E-beam Voltage (kV)
0.6	100	6
1.1	100	6
1.3	100	6
0.6	100	11
0.9	100	11
1.1	100	11
1.5	100	11
2.1	100	11

Table II: Deposition condition for reactively deposited (RD) films.

Rate (nm/s)	T _{initial} (° C)	O ₂ press. (mbar)	E-beam Voltage (kV)
0.6	100	7.2x10 ⁻⁶	6
0.6	100	1.2x10 ⁻⁴	6
0.6	100	2.4x10 ⁻⁴	6
0.6	200	1.2x10 ⁻⁴	6
0.6	200	2.4x10 ⁻⁴	6
0.6	300	1.2x10 ⁻⁴	6
0.6	300	2.4x10 ⁻⁴	6
1.1	100	2.4x10 ⁻⁴	6
1.3	100	2.4x10 ⁻⁴	6
0.9	100	2.4x10 ⁻⁴	11
1.1	100	2.4x10 ⁻⁴	11
1.5	100	2.4x10 ⁻⁴	11
2.1	100	2.4x10 ⁻⁴	11

Table III: Summary of XPS data for comparisons between hafnia films with varying composition. The anion-to-cation ratios were determined by backscattering spectrometry. We have not included the Hf 3d lines because the energy differences seen in this composition range were small. We have included the binding energies of Hofmann and Sanz²⁶ as reference.

$\frac{N^O}{N^{Hf} + N^{Zr}}$	Transition	E_b (eV)	Γ (eV)	E_b^\dagger (H & S)
Bulk (anion-to-cation ratio not measured)				
	O 1s	529.6±0.4	2.2±0.3	531.0±0.2
	O 1s (OH)	531.2±0.4	2.6±0.3	532.6±0.4
	Hf 4f _{7/2}	16.2±0.4	2.1±0.3	17.6±0.2
	Hf 4f _{5/2}	17.8±0.4	2.0±0.3	19.2±0.2
1.84±0.05	O 1s	530.8±0.2	3.13±0.3	
	O 1s (OH)	-----	-----	
	Hf 4f _{7/2}	17.4±0.2	2.1±0.3	
	Hf 4f _{5/2}	19.1±0.2	2.3±0.3	
2.09±0.06	O 1s	532.2±0.2	2.2±0.3	
	O 1s (OH)	533.3±0.2	3.0±0.3	
	Hf 4f _{7/2}	19.0±0.2	2.1±0.3	
	Hf 4f _{5/2}	20.6±0.2	2.1±0.3	
2.24±0.07	O 1s	531.7±0.2	2.2±0.3	
	O 1s (OH)	532.4±0.2	3.2±0.3	
	Hf 4f _{7/2}	18.4±0.2	2.3±0.3	
	Hf 4f _{5/2}	20.1±0.2	2.2±0.3	

Reference Energy: E_b (C 1s) = 284.4 eV
 $^\dagger E_b$ (C 1s) = 285.0 eV

Table IV: Summary of XPS data for comparisons between hafnia films with varying composition where ΔE is the energy separation between the oxide and hydroxide peaks; Γ^{O} and Γ^{OH} are the FWHM's of the oxide and hydroxide peaks, respectively; and Y^{O} and Y^{OH} are the heights of the oxide and hydroxide peaks, respectively.

$\frac{N^{\text{O}}}{N^{\text{Hf}} + N^{\text{Zr}}}$	ΔE (eV)	Γ^{O} (eV)	Γ^{OH} (eV)	$\frac{Y^{\text{O}}}{Y^{\text{OH}}}$
Bulk	1.6	2.18	2.60	2.6
1.84	---	3.13	----	---
2.09	1.1	2.16	3.01	2.4
2.24	0.7	2.20	3.17	1.6

FIGURE CAPTIONS

Figure 1: *Refractive index of RD HfO₂ films versus condensation rate. The oxygen backfill in the chamber has been held at 2.4×10^{-4} mbar.*

Figure 2: *Refractive index of RD HfO₂ films at 550 nm and 300 nm versus backfill oxygen pressure. The condensation rate was held at 0.6 nm/sec. The film made without an oxygen backfill exhibits an extinction coefficient of 0.01 at 300 nm whereas the other films show negligible absorption at this wavelength. The refractive indices at 300 nm compare well with those given by Baumeister and Arnon.†*

Figure 3: *Relative inhomogeneity at a wavelength of 800 nm versus oxygen backfill pressure for RD HfO₂ films. The condensation rate was held at 0.6 nm/sec.*

Figure 4: *Refractive index of RIAD HfO₂ films versus argon ion current density. The ion energy was 300 eV. The oxygen backfill in the chamber has been held at 1.4×10^{-4} mbar and the argon working gas at 6.4×10^{-5} mbar. In addition, the condensation rate has been held at 0.6 nm/sec.*

Figure 5: *Refractive index of LERIAD HfO₂ films versus xenon ion current density. The ion energy is 50 eV. The oxygen backfill in the chamber has been held at 1.4×10^{-4} mbar and the xenon working gas at 8.0×10^{-5} mbar. The condensation rate has been held at 0.6 nm/sec.*

Figure 6: *Transmission electron micrograph of (a) a RD HfO₂ film and (b) a RIAD film exhibiting a denser structure. The scale at the bottom of each photo-*

graph is 20 nm in length.

Figure 7: *Electron diffraction patterns of RD films deposited at chamber temperatures of (a) 38° C and (b) 200° C. The diffraction pattern in (b) is slightly overexposed.*

Figure 8: *Oxygen-to-metal ratio for RD films versus the oxygen backfill pressure. The condensation rate has been fixed at 0.6 nm/sec. Note that films deposited at higher temperature are closer to the ideal oxygen-to-metal ratio of two.*

Figure 9: *O 1s unresolved doublets and curve fits for HfO₂ source material and films. The solid line is the data after data massaging. The Gaussian at lower binding energy is oxygen bonded to Hf⁴⁺ while the higher energy Gaussian is the hydroxide peak. The oxygen-to-metal ratios corresponding to the O1s peaks are as follows: (a) Starting material, oxygen-to-metal ratio not measured (estimated to be 2.05), (b) 1.84±0.05, (c) 2.09±0.06, (d) 2.24±0.07.*

Figure 10: *Refractive index of RD and LERIAD HfO₂ films versus oxygen backfill pressure. The squares indicate only O₂ backfill in the chamber while the circles indicate both O₂ backfill and argon working gas. The solid line is a least squares linear fit to the data ($\rho^2=0.953$).*

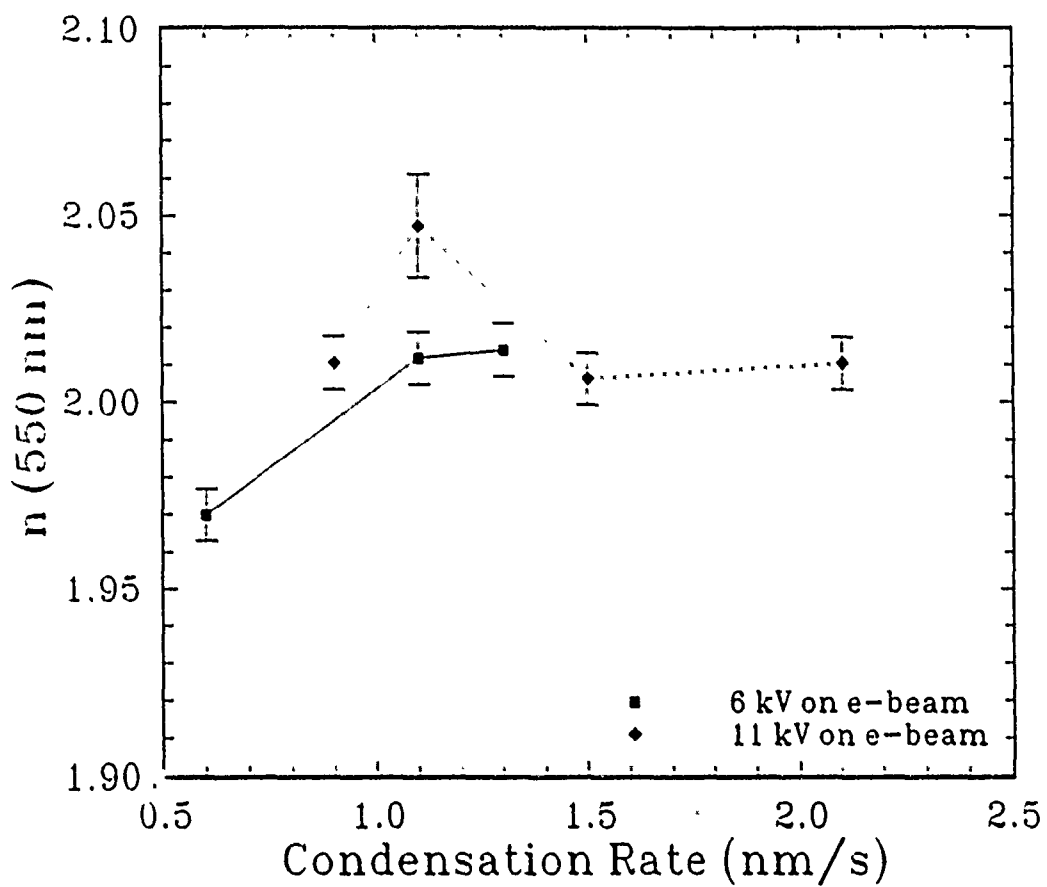


Figure 1

A. Optical and microstructural properties of hafnium dioxide thin films

J.P. Lohman, et al

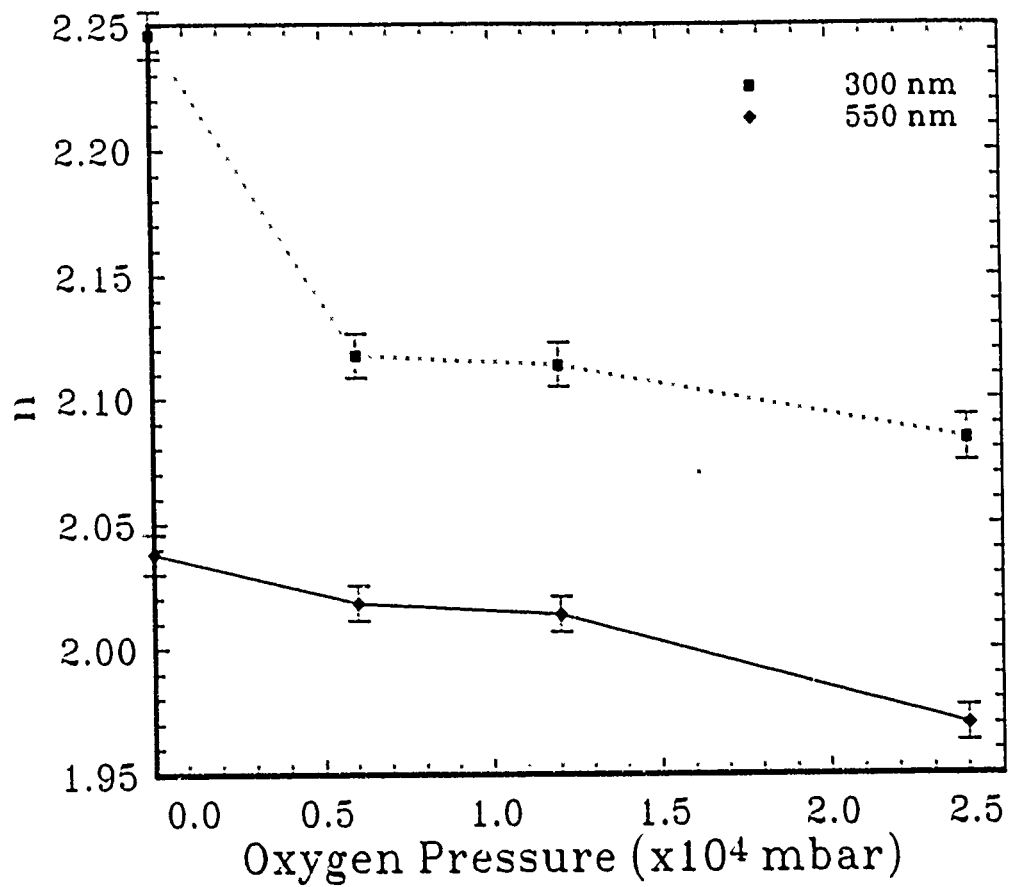


Figure 2

A. Optical and microstructural properties of hafnium dioxide thin films

J. P. Kehun, et al

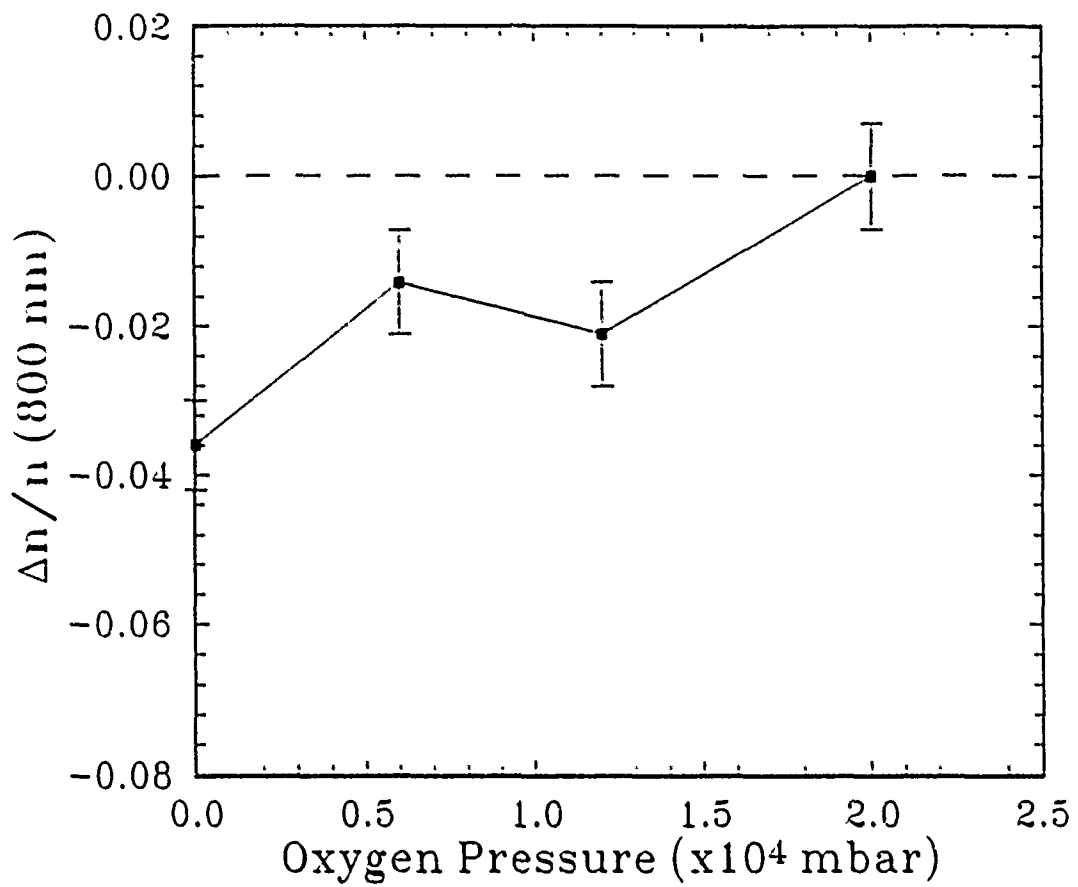


Figure 3
 Δ Optical and microstructural properties of hafnium dioxide thin films
J. P. Kehhan, et al

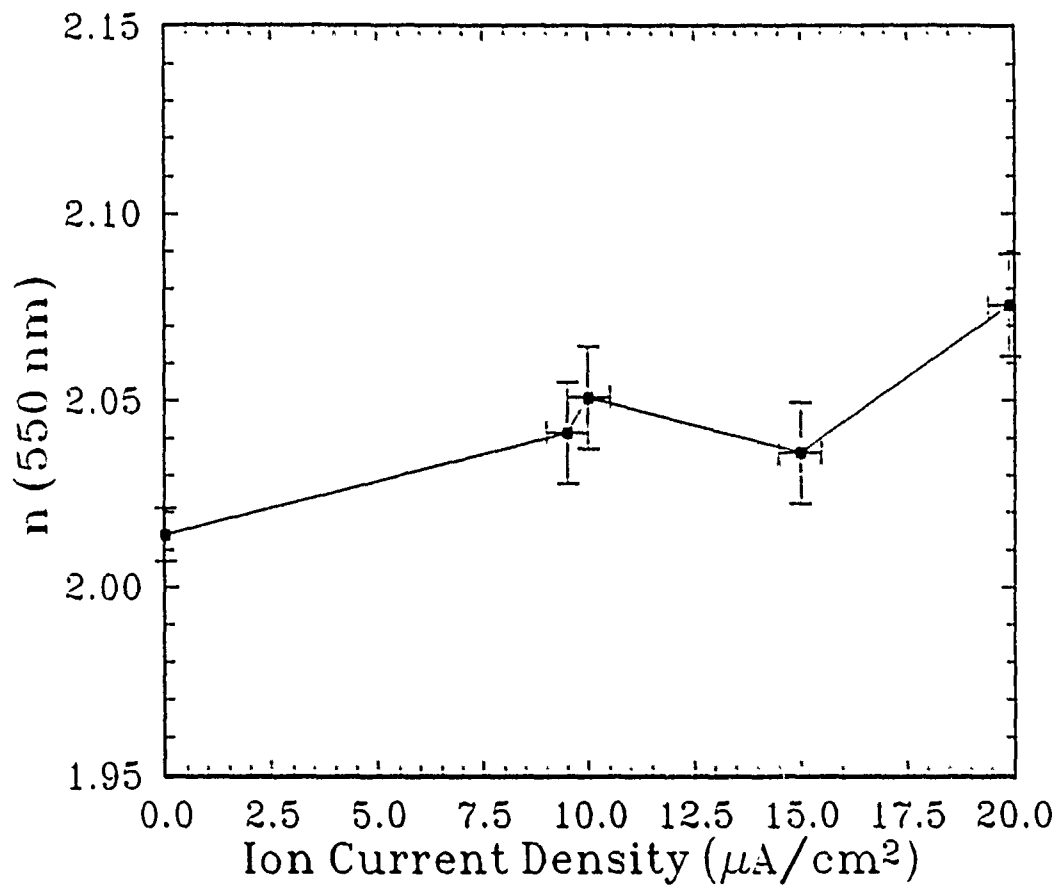


Figure 4

A. Optical and microstructural properties of hafnium dioxide thin films

J.P. Lehan, et al

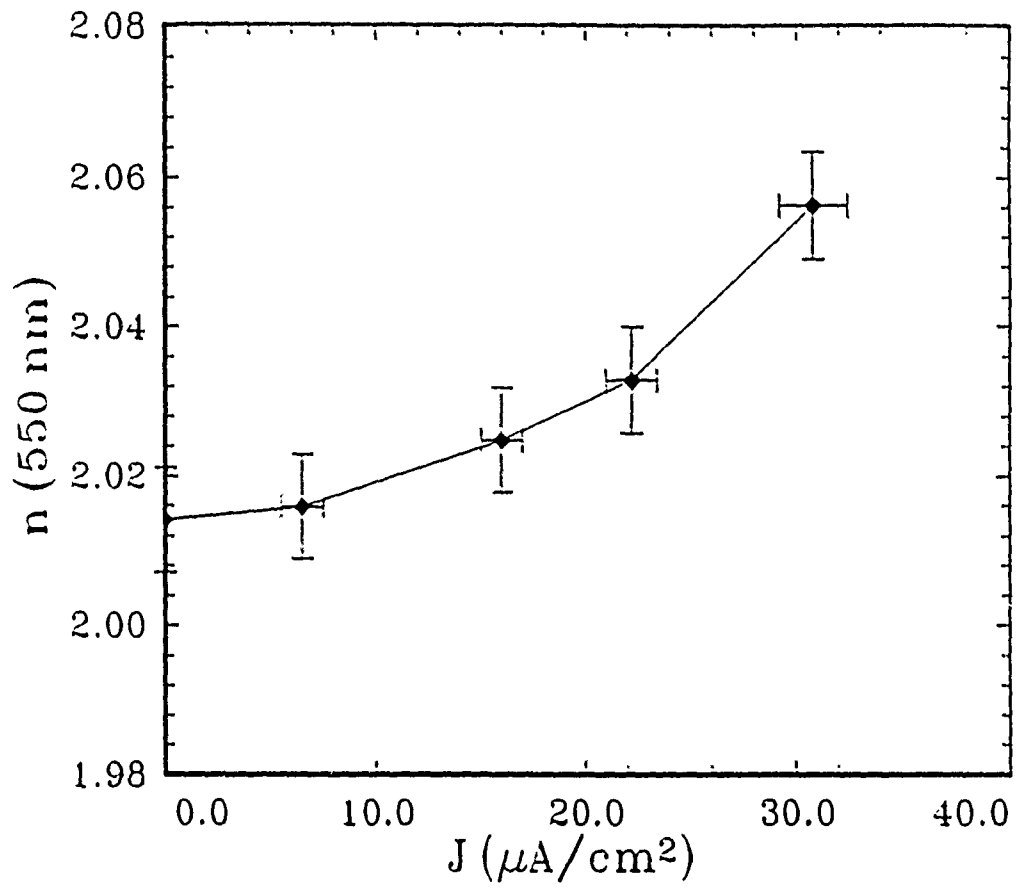
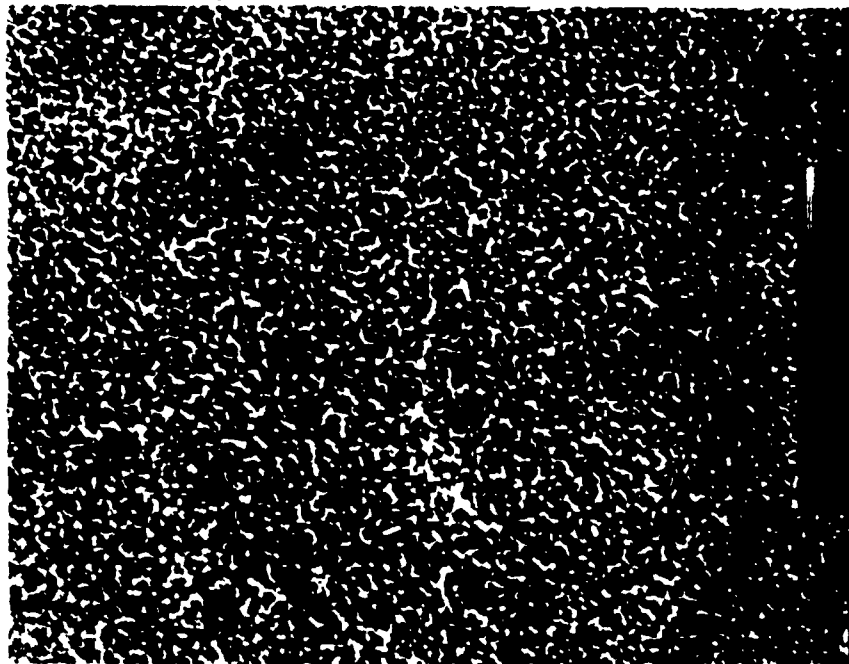


Figure 5

A - Optical and microstructural properties of hafnium dioxide thin films

J P Kellan, et al



(a)

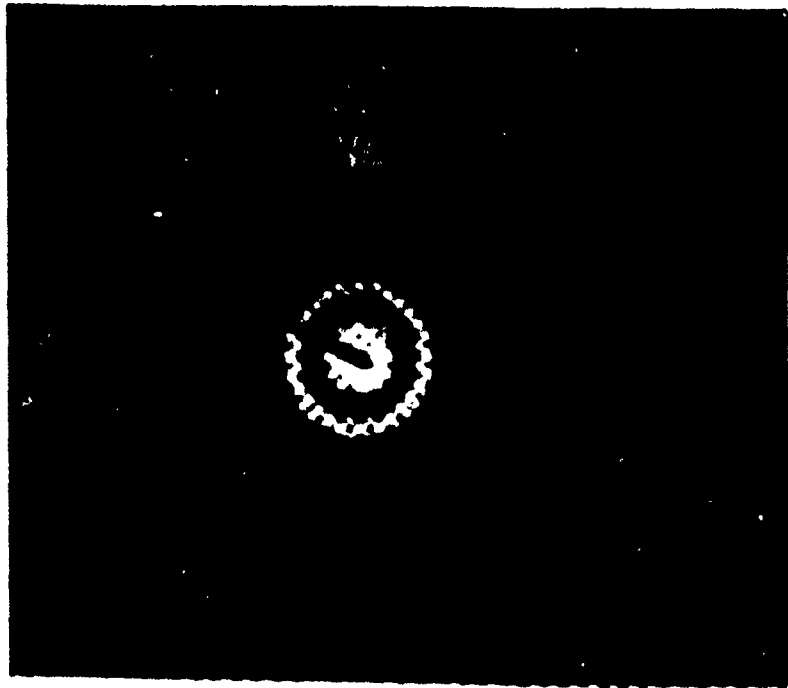


(b)

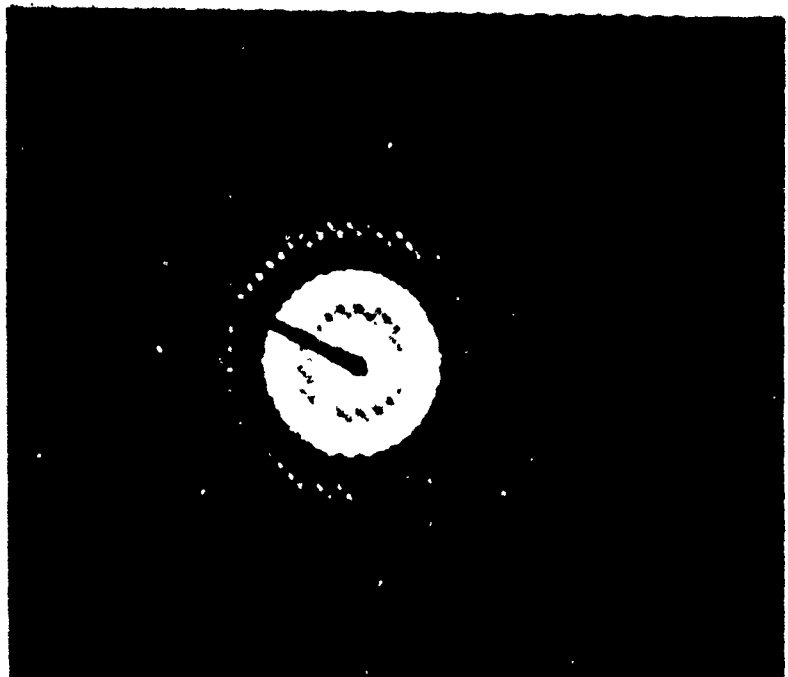
Figure 6

A - Optical and microstructural properties of hafnium oxide

J.P. Lehan, et al



(a)



(b)

7

Figure 7
A. Optical and microstructural properties of titanium dioxide thin films

J. J. Liou, et al

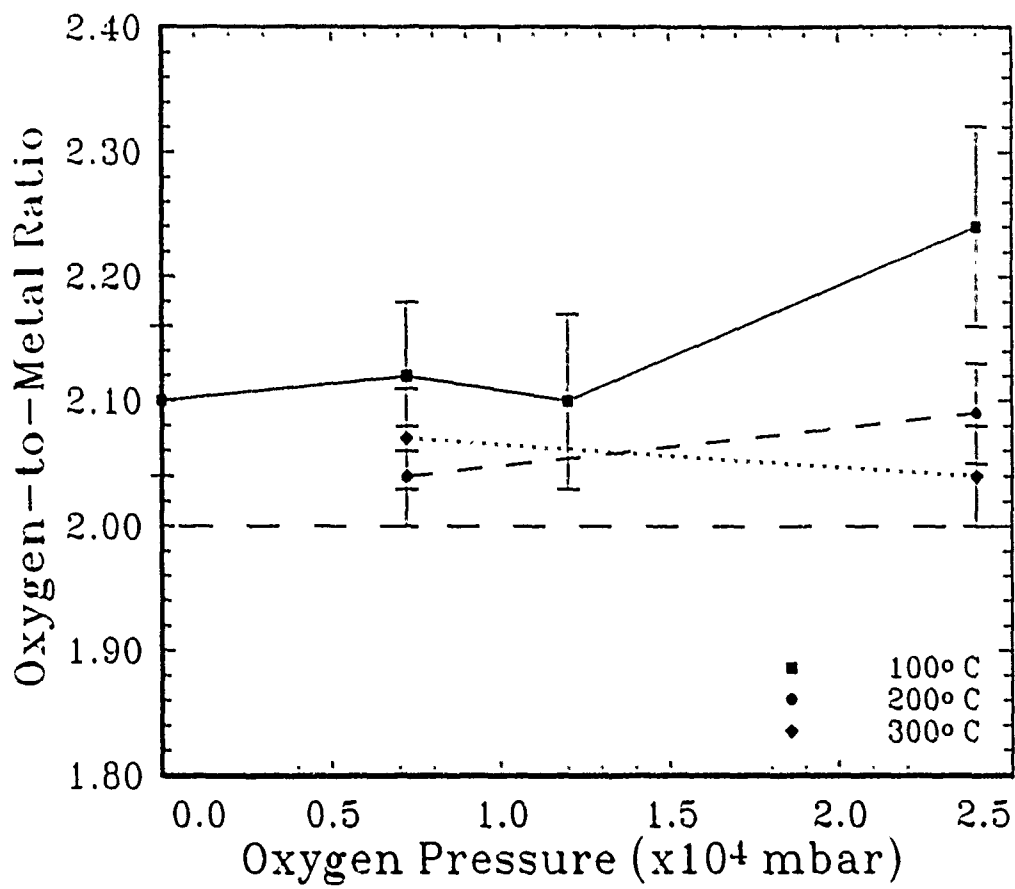


Figure 8

A-Optical and microstructural properties of barium dioxide thin films

J.P. Lehman, et al

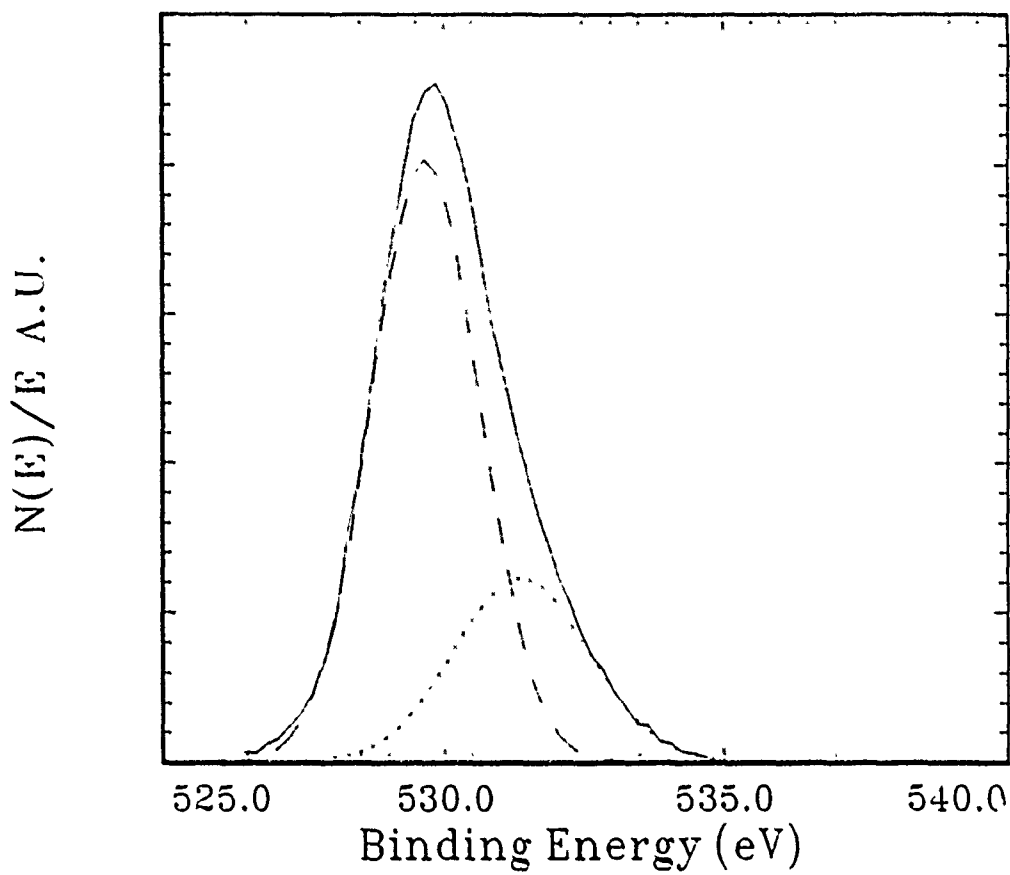


Figure 9(a)
A - Optical and microstructural properties of hafnium dioxide thin films
J.P. Lelien, et al

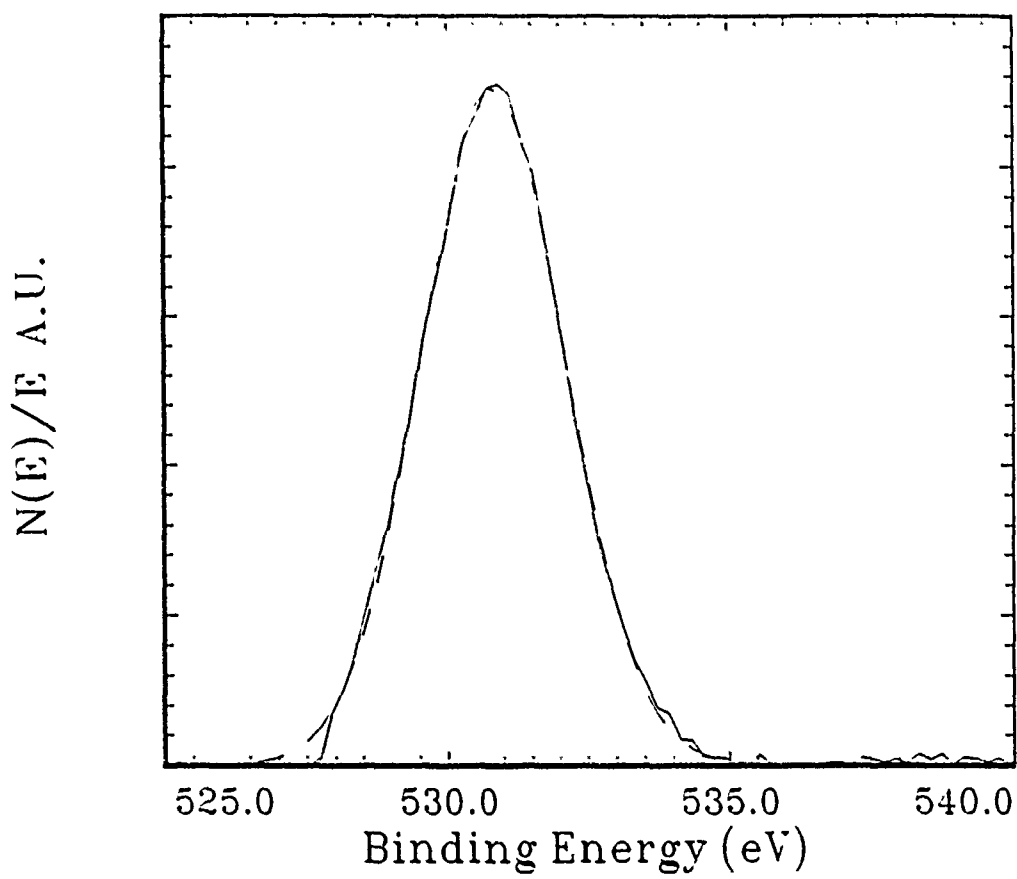


Figure 9(b)
A- Optical and microstructural properties of hafnium dioxide thin films
J.P. Lelien, et al

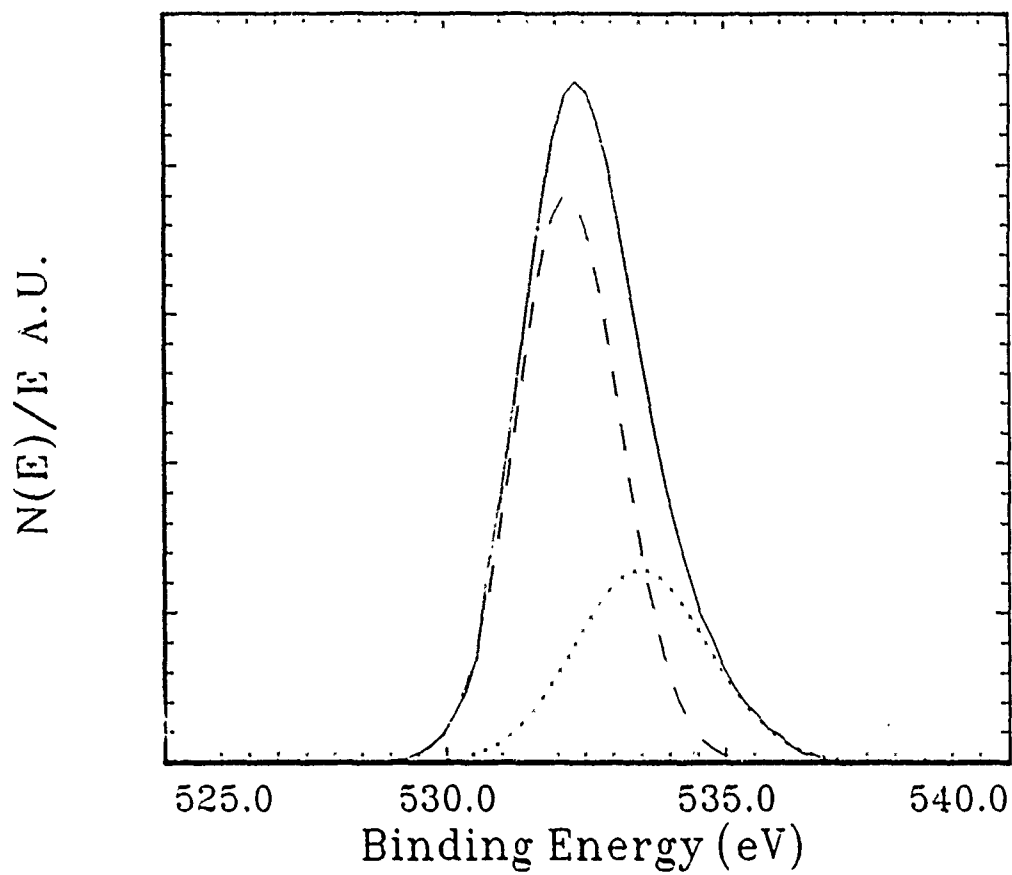


Figure 9(c)

A - Optical and microstructural properties of titanium dioxide thin films

J.P. Lehun, et al

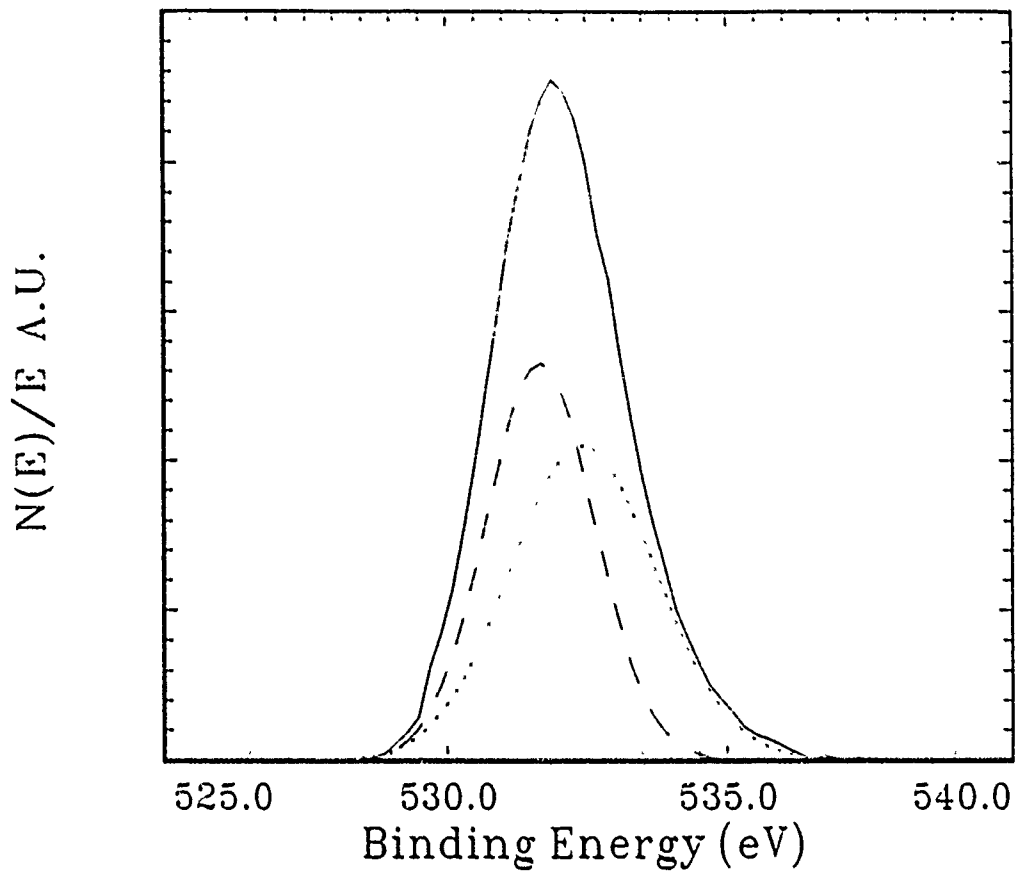


Figure 9(d)

A. Optical and microstructural properties of hafnium dioxide thin films
J.P. Lehan, et al

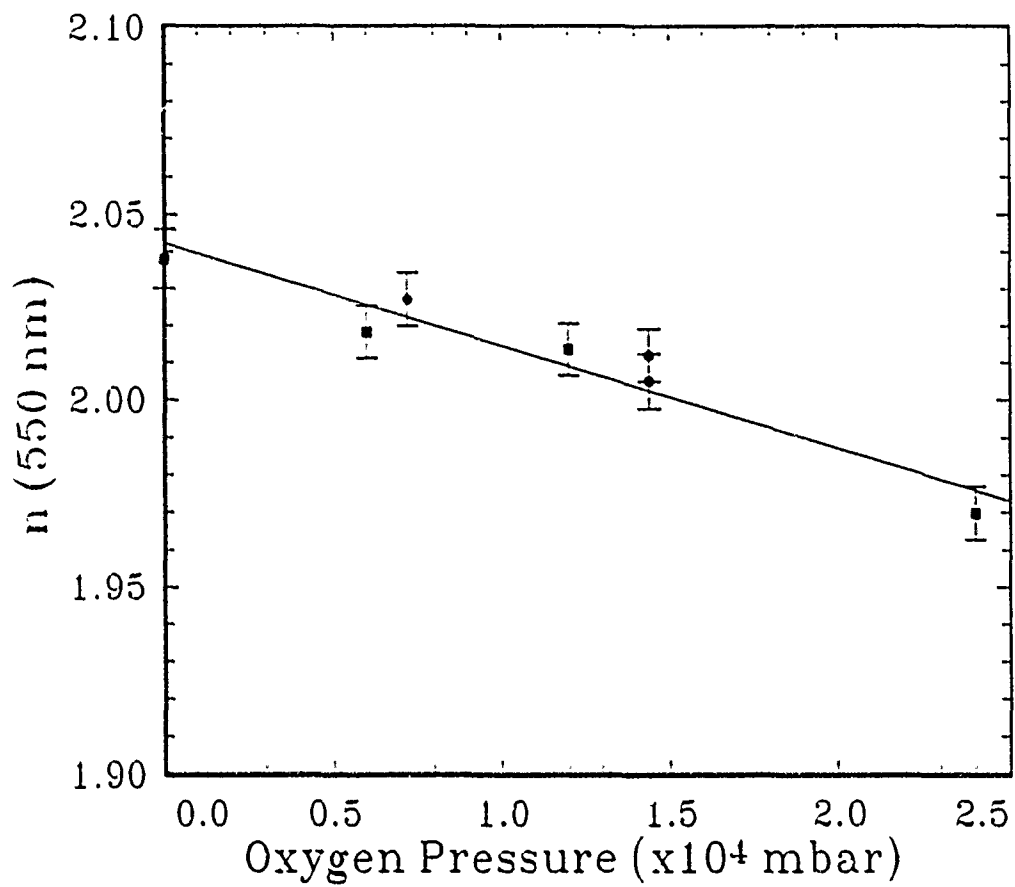


Figure 10

A - Optical and microstructural properties of hafnium dioxide thin films
J P Lohm, et al

PREPARATION OF YBaCuO THIN FILMS BY MULTILAYER DEPOSITION

Valentín García-Vázquez, Kim D. Powers,
J. A. Leavitt, L. McIntyre and Charles M. Falco

Department of Physics, Optical Science Center
and Arizona Research Laboratories
University of Arizona
Tucson, AZ 85721

Abstract

We report the fabrication of $\text{YBa}_2\text{Cu}_3\text{O}_{7-x}$ thin films by a combination of dc triode sputtering from Y and Cu targets, and simultaneous thermal evaporation from a BaF_2 source. A composition near the ideal 1:2:3 stoichiometry, with a resistive transition onset at 92 K and zero resistance at 80 K have been obtained by deposition on SrTiO_3 substrates, followed by furnace annealing.

1. Introduction

Some variation of sputtering is commonly used for the fabrication of YBaCuO superconducting thin films.¹ Successful variations of this technique include use of single stoichiometric targets,² co-deposition from multiple targets,³ and multilayer deposition from separate targets.⁴ In previous work,⁵ for example, we demonstrated that a sputtering system with two sources can produce superconducting thin films using separate metal targets of Y and Ba₂Cu₃ alloy, followed by an *ex situ* post-annealing in dry O₂. In this paper we report an improved process to produce YBa₂Cu₃O_{7-x} superconducting thin films.

We have replaced the Ba₂Cu₃ sputtering target previously used⁵ with pure metallic Cu, and added a BaF₂ evaporation source.⁶ Our system allows sequential deposition from the two sputtering targets (Y and Cu) and the thermal (BaF₂) source. Our post-deposition procedure now includes addition of water vapor during a portion of the anneal to reduce the annealing time.⁷ These two modifications have allowed better control in our preparation of stable films, and a more reproducible⁶ process for the fabrication of YBaCuO superconducting thin films.

2. Sample Preparation

As described above, a sputtering system with two magnetically-enhanced dc triode sputtering guns⁸ has been augmented with a thermal evaporation source. All three sources operate simultaneously as the substrate is sequentially rotated above each, allowing independent sequential deposition of Y, BaF₂, and Cu. Yttrium and copper are sputtered from the two separate metal targets, and the barium fluoride is evaporated from the thermal source. This combination of sputtering and evaporation is done in a pure Argon environment, without oxygen, at a pressure of 5.3 mTorr.

The BaF₂ evaporation rate is monitored using a quartz oscillator located 14 cm from the resistively heated source. Manual feedback to the power supply occasionally is used

to keep the evaporation rate constant to within approximately 1%. The two sputtering sources are electronically regulated to maintain sputtering rates from each constant to better than 0.5%.⁸

Single crystal (100) SrTiO₃ substrates are attached to the underside of a substrate holder and rotated by a servo-controlled motor over each of the three sources at different angular velocities to adjust the stoichiometry. A deposition consists of alternately passing the substrates over each source a number of times, resulting in layers of Y, BaF₂, and Cu. As is described below, the corresponding deposited Ba:Y and Cu:Y ratios are measured by Rutherford Backscattering Spectroscopy (RBS), from which corrections to the angular velocity ratios are calculated to give the desired 1:2:3 stoichiometry in subsequent depositions. Deposition rates and number of passes are kept constant from run to run. Sample thickness are roughly 4000 Å. Carbon substrates are used for each RBS analysis, which always show a 1:2 ratio for the Ba:F₂ in unannealed samples, suggesting a molecular BaF₂ evaporation.

In Figure 1, a partial RBS spectrum¹⁰ shows the depth profiles of Y, Ba and Cu in a typical Y(BaF₂)CuO film. Carbon substrates were used for the RBS samples because the Sr RBS signal from SrTiO₃ substrates overlaps the Cu RBS peak. The higher-than-usual ⁴He analysis energy of 3.8 MeV was required to separate the Y, Ba and Cu peaks. Cross sections for backscattering of ⁴He from Y, Ba and Cu are Rutherford at this energy and are accurately known.¹¹ Uncertainties in the stoichiometric ratios are determined by the counting statistics, and are at the level of a few tenths of a percent. The peak shapes in Fig. 1 indicate a slightly enhanced concentration of Ba in the mid-region of the film.

After deposition, films are transferred for annealing in oxygen in a conventional furnace. Our annealing procedure consists of heating the sample from room temperature to a maximum (typically 850 °C) in approximately 12 minutes, a 20-60 minutes soak at this temperature, a 60 minutes ramp down to 550 °C, a 30-120 minutes soak at this

temperature, and a slow cooling over several hours to room temperature. Oxygen is bubbled through water and introduced to the furnace during the heating and initial 20 minutes of the higher temperature soak cycle. Following this, the water is removed from the gas line and only dry oxygen is used. Similar annealing schedules have been used by others to promote the complete removal of fluorine, the growth of the perovskite phase, the proper diffusion of oxygen into the lattice, and to avoid harmful condensation.⁹

3. Rutherford BackScattering (RBS) Determination of Stoichiometry

Average stoichiometric ratios Y:Ba:Cu may be accurately measured using ⁴He RBS.¹¹ Energy analysis of backscattered ⁴He ions from a film of uniform composition yields a nearly flat-topped peak for each element present in the film. The areal density, $(Nt)_i$, for the *i*-th film element is given by $(Nt)_i = A_i / (Q\Omega\sigma_i)$, where *t* is the film thickness, N_i is atomic density, A_i is integrated peak count for *Q* incident ⁴He ions, Ω is the detector solid angle, and σ_i is the cross section for scattering of ⁴He by the *i*-th element. The average stoichiometric ratios $N_Y:N_{Ba}:N_{Cu}$ depend only on integrated peak count ratios $A_Y:A_{Ba}:A_{Cu}$ and cross section ratios $\sigma_Y:\sigma_{Ba}:\sigma_{Cu}$.

4. Results and Discussion

Resistance measurements are made by the usual four-point probe method using a closed cycle refrigerator instrumented for transport properties measurements. Electrical contacts were made using silver paint. Contact resistances of samples were found to vary from a few ohms to several hundred ohms. The contact resistance was decreased in a few cases when silver contact pads were sputtered on the samples and the leads soldered with indium. Figure 1 is a plot of the resistance vs temperature for a typical sample produced using this technique, showing an onset temperature of 92 K and a zero resistance transition temperature of 80 K.

In summary, we have fabricated superconducting thin films by sequential deposition of Y, BaF₂ and Cu multilayers on SrTiO₃ substrates, followed by annealing in oxygen. The Y and Cu are sputtered and BaF₂ is thermally evaporated. Reproducible transition temperature onsets of 92 K are obtained with this procedure.

Acknowledgements

The authors gratefully acknowledge Robert van Leeuwen and Dan Anderson for technical assistance and Dr. John L. Makous for helpful discussions. One of us (V. G.-V.) has benefited from a CONACyT-México fellowship. This work was supported by the U. S. Department of Energy under contract No. DE-FG02-87ER45297. The Ion Beam Analysis Facility is partially supported by the Center for Thin Film Studies (AFOSR-URI). We thank P. Stoss, M. Ashbaugh, B. Dezfouly-Arjomandy, Z. Lin and J. Oder for assistance with data acquisition and analysis.

References

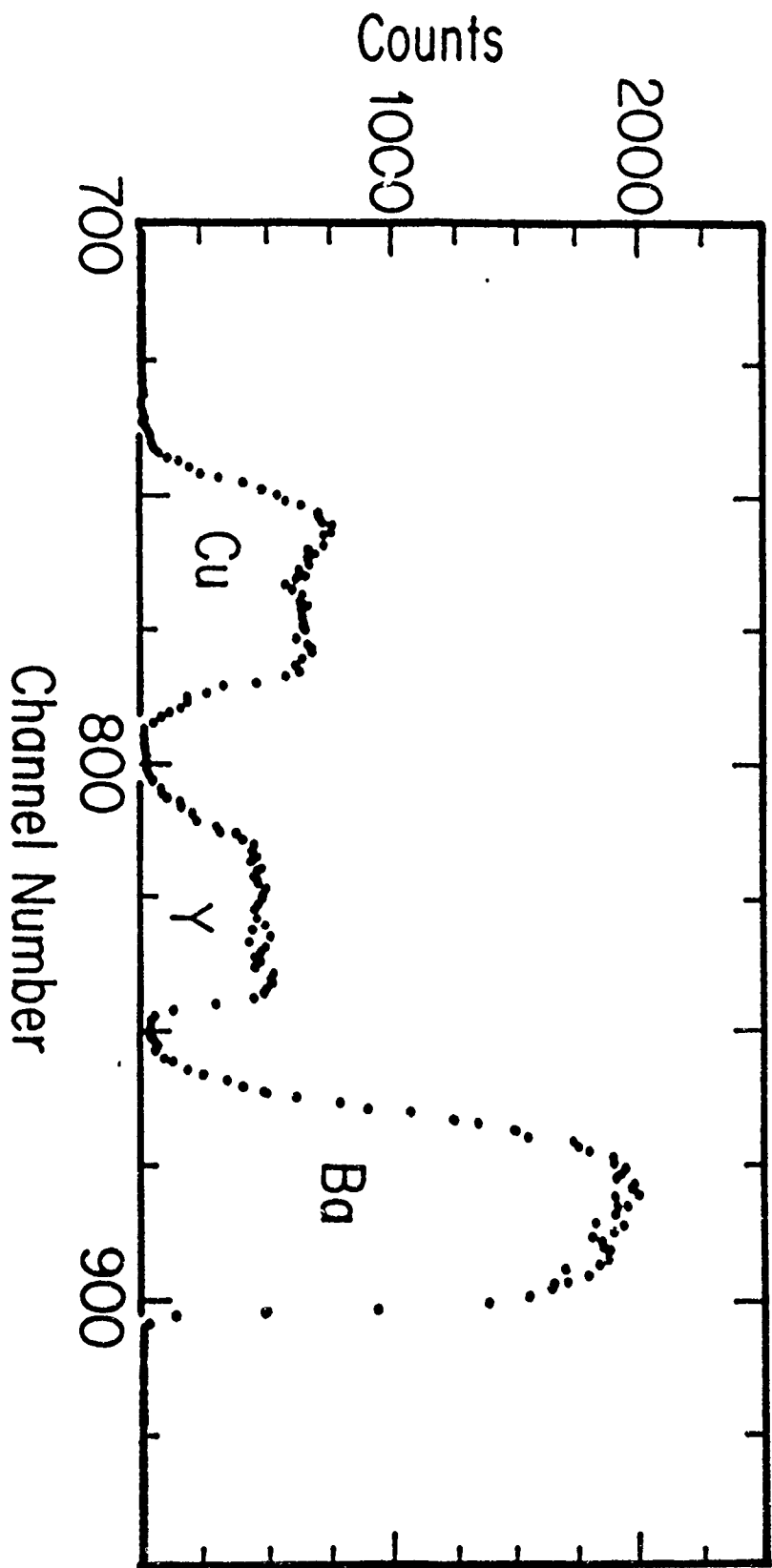
1. For an extensive bibliography on sputtering of high T_c superconductors see, for example, "Sputtering of High-Temperature Superconductors: A Bibliography," edited by P. Berdahl and R. B. Buckius, Lawrence Berkeley Laboratory, 1988.
2. S.H. Liou, M. Hong, J. Kwo, A. Davison, H.S. Chen., S. Nakahara, T. Boone and R.J. Felder, *Appl. Phys. Lett.*, **52**, (1988) 1735.
3. K. Char, A. D. Kent, A. Kapitulnik, M. R. Beasley and T. H. Geballe, *Appl. Phys. Lett.* **51** (1987) 1370.
4. S. Witanachchi, H.S. Kwok, D.T. Shaw and X.W. Wang, *Appl. Phys. Lett.* **53** (1988) 234.
5. J. L. Makous, L. Maritato and Charles M. Falco, *Appl. Phys. Lett.* **51** (1987) 2164.

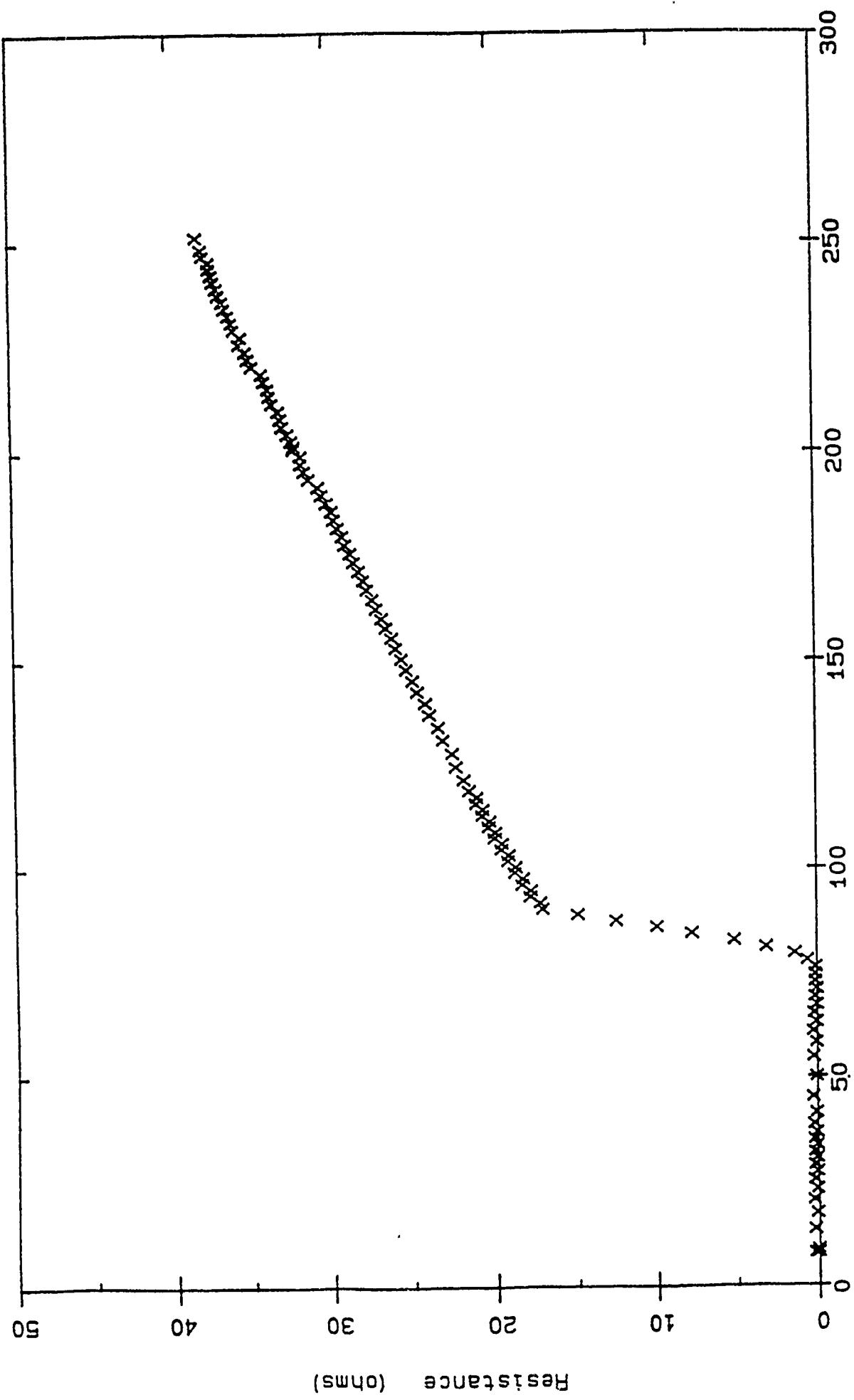
6. P. M. Mankiewich, J. H. Scofield, W. J. Skocpol, R. E. Howard A. H. Dayem and E. Good, *Appl. Phys. Lett.* 51 (1987) 1753.
7. P. M. Mankiewich, R. E. Howard, W. J. Skocpol, A. H. Dayem, A. Ourmazd, M. G. Young and E. Good, *Mat. Res. Symp.* 99 (1988) 119.
8. C.M. Falco, *Advances in Solid State Physics*, Volume XXV, 535, P. Grosse (ed.), Vieweg, Braunschweig, 1985.
9. Siu-Wai Chan, B.G. Bagley, L.H. Greene, M. Giroud, W.L. Feldmann, K.R. Jenkin II and B.J. Wilkins, *Appl. Phys. Lett.* 53 (1988) 1443.
10. J. A. Leavitt, *Nucl. Instr. and Meth.* B24/25 (1987) 717.
11. W. K. Chu, J. A. Mayer, and M. A. Nicolet, *Backscattering Spectrometry* (Academic Press, New York, 1978).

FIGURE CAPTIONS

Fig. 1 Portion of the 170° backscattering spectrum for 3.8 MeV ^4He incident on a 4000 Å $\text{Y}(\text{BaF}_z)\text{CuO}$ film on a carbon substrate. Analysis of these data indicates average stoichiometry $(\text{Y}_x\text{Ba}_y\text{Cu}_z)$ with $x = 1.03 \pm 0.01$, $y = 2.03 \pm 0.01$, and $z = 2.94 \pm 0.01$.

Fig. 2. Resistance transition of a typical film deposited on (100) SrTiO_3 .





Multilayer mirrors for 182Å

J.M. Slaughter, Mike K. Burkland, Patrick A. Kearney, A.R. Lampis,
Zoran Milanovic, Dean W. Schulze, and Charles M. Falco

University of Arizona, Optical Sciences Center, Laboratory for X-ray Optics
and Department of Physics
Tucson, Arizona 85721

James Roberts, Jonathan Kerner, and E.B. Saloman

National Institute of Standards and Technology
Gaithersburg, MD 20899

ABSTRACT

Multilayer coatings have been designed for peak reflectivity at 182.2Å and 45° angle of incidence. An optimizing computer code was used to find the best layer thicknesses and total number of layers in the structure. Silicon was chosen as the spacer material and molybdenum for the absorber. Mirrors were produced both by sputtering and by electron-beam evaporation in ultra-high vacuum (UHV). The mirrors fabricated by sputtering were made from high-purity source materials by moving a substrate table over the sources. The UHV evaporated samples were produced in a silicon/metals MBE system with a base pressure of 5×10^{-11} torr. The layers were formed by alternately opening shutters over the two electron-beam evaporators. The deposition rates were feedback stabilized and the shutter timing was computer controlled. The substrate was rotated to produce uniform layers and heated to 200°C for one sample. Rutherford Backscattering Spectroscopy (RBS), x-ray diffraction (XRD), and scanning tunneling microscopy (STM) were used for characterization. Synchrotron radiation from SURF-II was used to measure the reflectivity as a function of wavelength in the design region. All of the mirrors have amorphous Si layers and polycrystalline Mo layers. The measured reflectivity at 45°, scaled for 100% S-polarized light, ranges from 29% for a sputter-deposited mirror to 47% for the mirror produced in the MBE system at a substrate temperature of 200°C.

1. INTRODUCTION

Multilayer coatings with peak reflectivity at 182.2 Å are of interest in soft x-ray laser experiments using C as the amplifying medium. This wavelength corresponds to spontaneous emission between levels 3 and 2 in hydrogen-like carbon (C VI).¹ Mirrors are needed at normal incidence as cavity mirrors and at 45° as polarizers and beam manipulators. Since the Brewster angle for soft x-rays is near 45° for almost all materials, mirrors can be fabricated with high reflectivity for S-polarized and very low reflectivity for P-polarized light. Such mirrors have immediate applications in soft x-ray laser microscopy.²

Mo and Si were chosen as the most promising material pair due to their favorable optical constants in this wavelength region. Following the usual convention, we refer to the Si layer as the spacer and to the Mo layer as the absorber material. Consider the complex index of refraction $\tilde{n} = n + ik$, where we refer to n (the real part) as the index and k (the imaginary part) as the extinction coefficient. Ideally, both materials should have a small k to reduce absorption. To get the most reflectivity, we seek materials with the greatest difference in their indices. The extinction coefficient of

silicon at this wavelength is lower than that of carbon and n is closer to unity. Recent measurements of the optical constants of molybdenum indicate that it is better than tungsten for the absorber material since its extinction coefficient is lower, and n is farther from unity³. Ideal multilayers of silicon and molybdenum have peak reflectivities near 50%. Previous studies of sputter-deposited multilayers containing Si and Mo show that this combination can form stable and smooth layers.^{4,5}

The mirrors were fabricated by sputter deposition as well as electron-beam deposition in a UHV silicon/metals MBE system. Many other workers have produced Mo/Si mirrors by sputtering but few mirrors have been produced in a UHV environment. Ogura et al. have recently reported characterization results for Mo/Si mirrors produced by e-beam evaporation in UHV at temperatures from -155°C to 400°C and compared them to similar mirrors produced by three sputtering techniques⁶. They found that the UHV-deposited mirrors had completely amorphous layers, high interface roughness and the lowest reflectivity of the techniques used. In contrast, we find that the UHV deposited mirrors have polycrystalline Mo layers and very high reflectivity when produced at 200°C .

We report here results obtained with Mo/Si mirrors designed for peak reflectivity at 45° for 182.2\AA radiation: one mirror produced by sputtering and two in the MBE system.

2. MIRROR DESIGN

Two optimizing computer codes were used to find the best layer thicknesses and total number of layers in the structure. One program, named BEST, maximizes the reflectivity of a periodic structure made of a repeated bilayer with total number of layers N_T . BEST finds the structural period which gives peak reflectivity at the desired wavelength then adjusts the ratio of the layer thicknesses to find the maximum reflectivity. Mirrors have also been designed for an optimized aperiodic structure using the method of Yamamoto et al.¹. A graph of reflectivity versus N_T is used to determine which structure to fabricate. Figure 1 shows such a plot for ideal 45° mirrors.

The optical constants used for the calculations were interpolated from the data of Windt (see reference 3). For Si we have $(n,k) = (0.9791, 0.00652)$; for Mo, $(n,k) = (0.8221, 0.0540)$; and for W, $(n,k) = (0.8865, 0.1411)$.

Table I Predicted reflectivities for structures with 21 layers.

	<u>R (Mo/Si)</u>	<u>R (W/Si)</u>
APERIODIC	0.512	0.286
PERIODIC	0.511 (45.8/96.2) \AA	0.286 (35.6/103.) \AA

The reflectivity of the aperiodic design rises faster than the optimized periodic structure but both saturate quickly and at the same reflectivity. Based on this calculation, we chose to fabricate periodic multilayers with $N_T=21$. Table I is a comparison of the reflectivities for this case. The predicted increase in reflectivity of the aperiodic structure over the periodic one was too small to offset the additional difficulties in characterizing of such mirrors. Mo/Si has a much higher ideal

reflectivity than W/Si.

The "ideal" reflectivities were calculated for structures which are made of perfectly flat and smooth layers of homogeneous material. The real structures may have grain boundaries, interdiffusion and faceting which cause the interfaces to deviate from the ideal. The reflectivity of a multilayer is reduced from its ideal value by these effects which we consider collectively as "roughness," denoted by σ , where σ is treated theoretically as the rms deviation from a perfect interface. Detailed descriptions of the theory, can be found elsewhere⁸. Typical values for σ of multilayer coatings are 5 to 20Å, inferred from models via fits to reflectivity data.

3. FABRICATION AND CHARACTERIZATION

3.1 Sputtering

The sputtered mirror was deposited on a Si substrate and a pyrolytic graphite substrate was simultaneously coated for the purpose of Rutherford Backscattering Spectroscopy (RBS) studies. The RBS yields accurate information about the levels of contaminants in the samples and can also be used to determine deviations from bulk density in the film when independent measurements of the film thickness are available. The specific deposition technique was dc-sputtering onto moving substrates. The substrates were initially at room temperature and no effort was made to control their temperature during deposition. The sputtering guns are magnetically-confined-plasma type. Our system has been described elsewhere.⁹ The 2.25 inch diameter targets were 99.9999% pure Si and 99.95% Mo. The base pressure of the deposition chamber was 3×10^{-7} torr. The argon pressure was 5.5 mtorr during sputtering and was held constant to within ± 0.01 mtorr by means of gas flow controllers and a micrometer-adjustable variable-orifice valve in the main pump line. Sputtering rates on gun axes were approximately 3 Å/s for each gun. The substrates rotated in a plane 12 cm above the guns. The substrate table is driven by a computer-controlled servo motor. Each layer was deposited in a single pass over the corresponding gun.

3.2 UHV deposition by electron-beam evaporation

The MBE system is a Perkin-Elmer 433-S¹⁰ which is specifically designed for epitaxial growth of Si and refractory metals. The current configuration includes two 40cc electron-beam evaporators with a 99.9999% Si charge in one crucible and MRC marz-grade Mo pellets¹¹ in the other. During growth the 3-inch Si (100) substrates were rotated at 30 RPM to achieve uniform layer thicknesses. The two samples discussed here were produced in the same day. The system has a load lock to allow removing and inserting substrates without compromising the vacuum in the growth chamber. Sample 37 was made without any substrate heating, resulting in a growth temperature of approximately 40°C. Sample 38 was made with the substrate temperature controlled at 200°C. The base pressure was 5×10^{-11} torr and the pressure during deposition was 1×10^{-9} torr with H₂ making up 70% of that total. The layers were formed by alternately opening shutters, by computer control, over the two evaporators. Deposition rates are held constant by active feedback from an Inficon Sentinel III deposition controller¹² which uses an electron impact emission spectroscopy flux monitor to monitor the flux. The deposition rates were; 1.0Å/s for Si and 0.50Å/s for Mo.

3.3 X-ray diffraction

The samples were characterized with three types of XRD, low-angle θ -2 θ , high-angle θ -2 θ , and Seemann-Bohlin (S-B). All utilized the Cu K α line at 1.542Å. The θ -2 θ

spectra were obtained from standard powder diffractometers. The low-angle spectra allow one to determine the period of the multilayer structure. The S-B spectra were obtained with a specialized diffractometer made for this geometry. In the S-B geometry, the incident beam is held at a fixed, small grazing angle while the detector sweeps. This geometry enhances the signal from the thin film at the expense of the substrate signal. For the spectra taken from these samples a 6° grazing angle was used. Such spectra are useful in determining phases and coherence lengths in polycrystalline samples. The high-angle spectra yield the same type of information as the S-B except that the coherence length probed is perpendicular to the film plane rather than having an in-plane component as in S-B.

The S-B and high-angle spectra show that the Mo layers are polycrystalline and the Si layers amorphous in all of the samples. Mo-layer coherence lengths determined from S-B are: 40Å for sample 38, 100Å for sample 37, and 32Å for the sputtered sample. The coherence lengths determined from the high-angle spectra are approximately 60Å for all three samples. The fact the high-angle coherence lengths are all the same and approximately equal to the Mo layer thickness implies that the crystallite size in the perpendicular direction is limited by the Mo layer thickness. The S-B coherence lengths indicate that there is an in-plane structural difference between the two MBE samples. In sample 37 the crystallites are larger in-plane than perpendicular to the film plane whereas in 38 they are similar. The sputtered sample is the most disordered.

Low-angle θ - 2θ spectra yield the following periods: 140Å for sample 37, 130Å for sample 38, and 136Å for the sputtered sample. The relative intensities of the successive orders of Bragg peaks for sample 38 are higher than for 37 or for the sputtered sample, indicating that 38 has the lowest interface roughness. Sample 38 has seven detectable Bragg peaks, as shown in Figure 2, while the others have four to five. In addition, the sample 38 spectrum shows clear subsidiary maxima throughout the entire spectrum. Fast damping of the higher order peaks implies high interface roughness. Although it is difficult to quantitatively analyze the peak intensities from a simple powder diffractometer, we can make the qualitative conclusion that sample 38 has the lowest interface roughness of the three. The important quantitative information obtained from these spectra are the multilayer periods. The synchrotron reflectivity measurements are used to determine σ .

3.4 Scanning tunneling microscopy

The scanning tunneling microscope (STM) measures the electron tunneling current across the small gap between a fine tungsten tip and the surface being scanned. The particular STM used was a Nanoscope II made by Digital Instruments¹³. This particular instrument has a vertical resolution of less than 1Å and a lateral resolution of approximately 1Å. This high resolution makes the STM ideal for studying the surface roughness of x-ray mirrors. Since this STM operates in air, one must keep in mind that the surface has been modified to some extent by oxidation and contamination and therefore may not be representative of the internal interfaces on an Ångström length scale.

Scans were taken over a broad range of horizontal length scales. One scan consists of an array of 400 X 400 points taken over a square on the sample surface. One can then calculate the rms roughness over the entire scan or a part of it. The roughness was measured on the two MBE samples for square areas ranging from 10Å to 6µm on a side. For the smaller areas, many samples were taken and the roughnesses averaged to get a statistically significant sample of the surface. For both samples, the

roughness varied from $(1 \pm 0.3) \text{ \AA}$ for the smallest area to a saturation value of $(7 \pm 0.3) \text{ \AA}$ for squares larger than 800 \AA on a side. A possible interpretation for this behavior is as follows. When the scan size is much greater than the crystallite size, the roughness is calculated over grain boundaries and facets. However, when the scan size is much less than the crystallites, most of the samples are taken on a single crystal surface thus yielding an atomic level roughness.

4. CHARACTERIZATION USING SYNCHROTRON RADIATION

Synchrotron radiation from SURF-II was used to measure the reflectivity as a function of wavelength in the design region. A detailed description of the apparatus can be found elsewhere¹⁴. The polarization of the beam impinging upon the sample is $89 \pm 2\%$ S in the region of interest. Since the measurements were performed at 45° , the contribution to the measured signal from the P-polarized component of the beam is negligible. Therefore we can calculate the reflectivity for pure S-polarized light by scaling the measured reflectivity by a factor of $1 / 0.89$. The relative error in the measured reflectivity is estimated to be $\leq 10\%$.

Figures 3 and 4 show the measured reflectivity vs. wavelength of MBE samples 37 and 38 respectively. Figure 5 is the reflectivity of the sputter-deposited sample. Sample 38, deposited at $T=200^\circ\text{C}$, has the highest peak reflectivity at 47%. The other MBE mirror, sample 37, has a much lower reflectivity (33%) and the sputter-deposited sample has the lowest of the three at 29%.

The data can be fit fairly well by including an interface roughness parameter σ in the reflectivity calculation and adjusting it to fit the peak reflectivity. The optical constants of reference 3 were used for all calculations unless otherwise noted. This procedure yields the following values of σ : 7.5 \AA for sample 38, 20 \AA for sample 37, and 22 \AA for the sputtered sample. For the sputtered sample, the poor fit to the peak width indicates that the reduction in peak reflectivity is not simply due to high interface roughness. The actual optical constants appear to be significantly different than those in reference 3. We attribute this difference to oxygen contamination of the sample. The RBS characterization of the sputtered sample made on a carbon substrate shows that the sample has a high oxygen content (13 atomic %), which may change the optical constants of the materials. In particular, the extinction coefficient of SiO_2 is much greater than that of Si ¹⁵ implying that oxygen contamination makes Si a poorer spacer.

To model the effect of this contamination on the reflectivity of the sputtered sample, a fit was performed using optical constants which were determined by Windt et al. for a Si film with known oxygen contamination¹⁶. In this case the roughness parameter needed to fit the peak reflectivity is 7 \AA . Comparing the two fits, shown in Figure 5, we see that the calculated peak width is greater than the experimental width for the contaminated case but less than experiment for the uncontaminated case. Increasing peak width arises from increasing absorption since the number of layers participating is reduced and the width is inversely proportional to the number of layers participating. The fact that the high-absorption optical constants yield a calculated peak that is too wide implies that the absorption in our sample is not quite as high as in the model. Clearly we must know the optical constants very well in order to determine a physically meaningful value for σ . In the present case we can conclude only that the real interface roughness of this sample is slightly greater than 7 \AA and much less than 22 \AA .

5. DISCUSSION

Table II summarizes the properties of the three mirrors as determined from the various characterization methods used. The low-angle XRD and the synchrotron reflectivity measurements are in good agreement as to the structure and quality of the samples. The XRD spectrum of sample 38 indicates that it has the most ideal structure and it also has, by far, the highest reflectivity. For samples 37 and 38, there is good agreement between the multilayer period (D) as measured by XRD and the D determined from fitting the synchrotron reflectivity data. Since we were unable to find optical constants which yield a good fit to the reflectivity curve of the sputtered sample, those fitting parameters are not shown in the table.

Table II Characterization results.

sample	XRD	Reflectivity (SURF-II)			
	D (Å)	R _{peak} (%)	wavelength (Å)	D (Å)	σ (Å)
37	140	33	177.5	142	20
38	130	47	168.0	129	7.5
sputtered	136	29	177.5	---	---

The STM characterization was able to determine the surface roughness over a range of horizontal length scales covering more than three orders of magnitude. Possible future improvements include, in-situ passivation of the sample surface or in-situ measurement. If an uncontaminated surface can be studied, the measurements may also reflect the properties of the internal interfaces.

There is an apparent disagreement between the present results and the results of Ogura, et al. as described in the introduction. We have clearly shown that e-beam evaporation in UHV can produce high quality soft x-ray coatings. The differences may be due to the use of slightly different deposition conditions (the present mirrors were made with higher deposition rates and better vacuum) or that fact that the mirrors made by Ogura had somewhat thinner Mo layers than the present samples.

6. ACKNOWLEDGEMENTS

The authors wish to thank David Windt for supplying optical constants, John Leavitt for making RBS measurements, and Charles Skinner for motivating the work on 182.2Å mirrors. This work is supported by the Air Force Office of Scientific Research under contract AFOSR-88-0010 and by the Joint Services Optics Program under contract F-49620-88-C-0009. The NIST component is supported by the Aerospace Guidance and Metrology Center, Newark AFB, under contract SDIO-WPD-B238.

7. REFERENCES

1. S. Suckewer, C.H. Skinner, D. Kim, E. Valeo, D. Voorhees, and A. Wouters, Phys. Rev. Lett., 57, 1004 (1986).
2. C.H. Skinner, D. Diccico, D. Kim, L. Meixler, C.H. Nam, W. Tighe, and S. Suckewer, IEEE Trans. on Plasma Science, 16, 512 (1988).

3. D.L. Windt and J.B. Kortright, these proceedings.
4. Felix E. Fernandez, C. Riedel, A. Smith, B. Edwards, B. Lai, F. Cerrina, M. G. Lagally, Martin J. Carr, A. D. Romig, Jr., J. Corno, L. Nevot, B. Pardo, J. M. Slaughter and Charles M. Falco, "Monolithic Fabry-Perot structure for soft x-rays," X-Ray Multilayers for Diffractometers, Monochromators, and Spectrometers, Finn E. Christensen, Editor, Proc. SPIE 984, 256-262 (1988).
5. A. K. Petford-Long et al., J. Appl. Phys., 61, 1422 (1987).
6. S. Ogura, M. Niibe, Y. Watanabe, M. Hayashida and T. Iizuka, "Comparison among multilayer soft x-ray mirrors fabricated by electron beam, DC-, RF-magnetron sputtering and ion beam sputtering deposition," X-Ray Multilayers for Diffractometers, Monochromators, and Spectrometers, Finn E. Christensen, Editor, Proc. SPIE 984, 140-148 (1988).
7. M. Yamamoto, S. Nakayama and T. Namioka, "Optimum design method of multilayer elements," X-Ray Multilayers for Diffractometers, Monochromators, and Spectrometers, Finn E. Christensen, Editor, Proc. SPIE 984, 160-165 (1988).
8. See for example: H.E. Bennett and J.O. Porteus, J. Opt. Soc. America, 51, 123 (1961). Also B. Vidal and P. Vincent, Applied Optics, 23, 1794 (1984).
9. C. M. Falco, J. de Physique 45, C-5, 499 (1984).
10. Perkin Elmer Physical Electronics, Eden Prairie, MN, USA.
11. Materials Research Corporation, Orangeburg, NY, USA.
12. Inficon Leybold-Heraeus, Inc., East Syracuse, NY, USA.
13. Digital Instruments, Inc., Santa Barbara, CA.
14. J. Rife and J. Osantowski, Nuclear Instrum. and Methods, 172, 297 (1980).
15. H.R. Philipp, Handbook of Optical Constants of Solids, Edward D. Palik Editor, pp. 749-763, Academic Press, Orlando, Florida (1985).
16. David L. Windt, Webster C. Cash, Jr., M. Scott, P. Arendt, Brian Newnam, F.F. Fisher, A.B. Swartzlander, P.Z. Takacs, and J.M. Pinneo, Applied Optics, 27, 279 (1988).

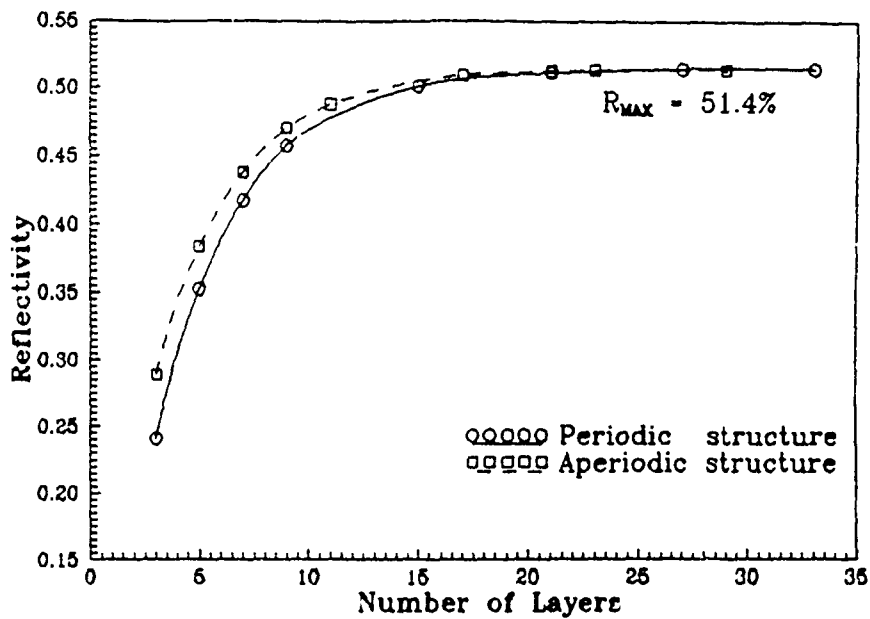


Figure 1. Calculated reflectivity of ideal optimized Mo/Si multilayers at 182.2Å and 45°. The lines are only a guide to the eye.

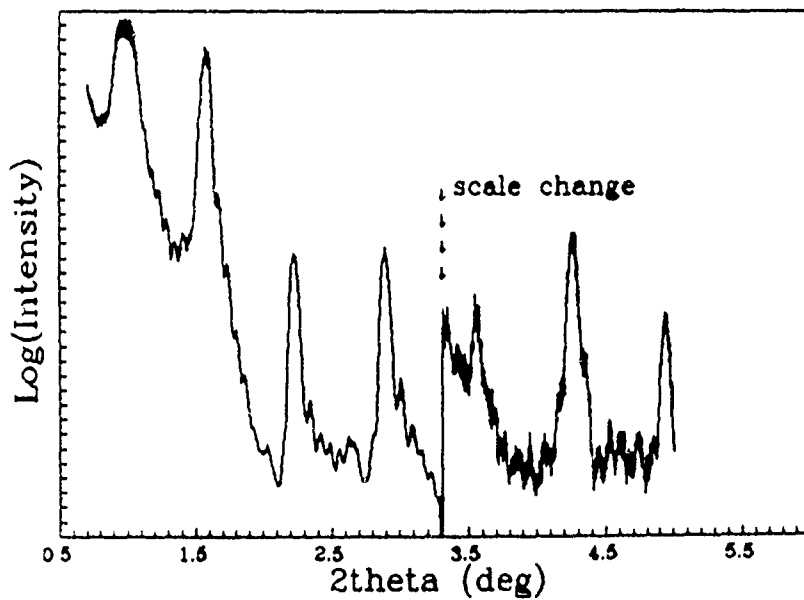


Figure 2. Low-angle θ - 2θ diffraction spectrum for sample 38.

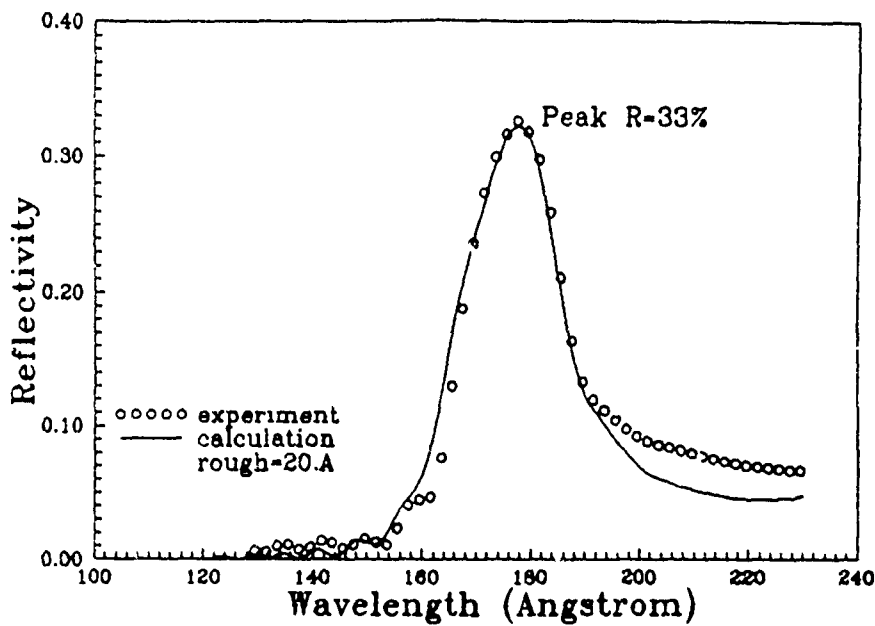


Figure 3. Reflectivity of MBE sample 37: Mo/Si mirror deposited on a near room temperature substrate. The symbols are the measured data, scaled to 100% S-polarization, and the line is a calculation using $\sigma=20\text{\AA}$.

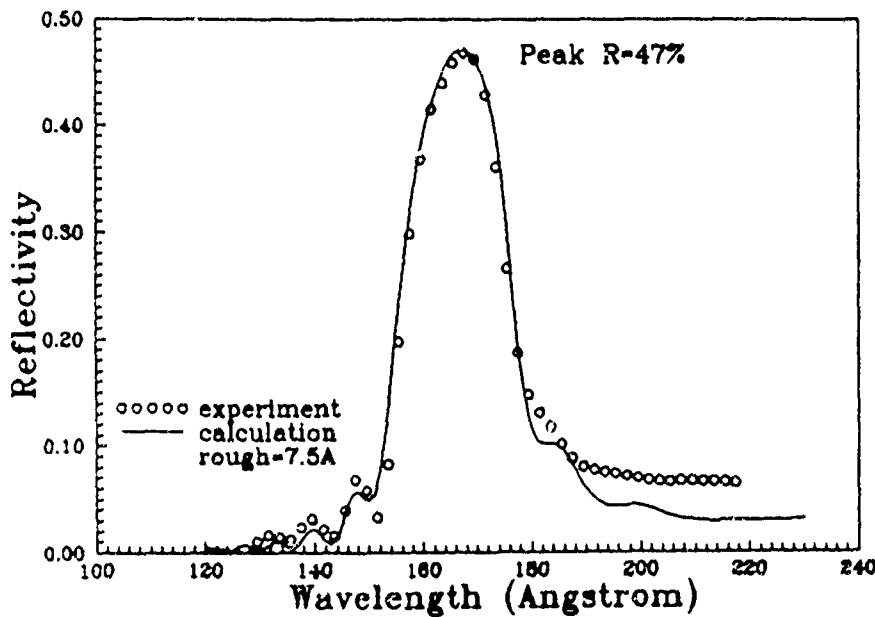


Figure 4. Reflectivity of MBE sample 38: Mo/Si mirror deposited on a 200°C Si substrate. The symbols are the measured data, scaled to 100% S-polarization, and the line is a calculation using $\sigma=7.5\text{\AA}$.

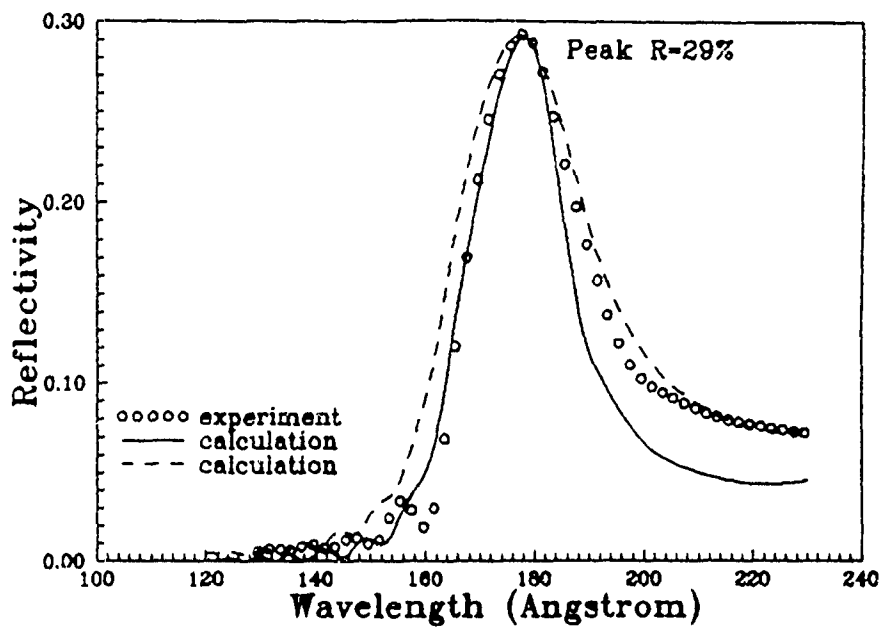


Figure 5. Reflectivity of the sputtered sample. The symbols are measured data, scaled to 100% S-pol. The solid line is a calculation with $\sigma=22\text{\AA}$ and the dashed is with constants for contaminated Si and $\sigma=7\text{\AA}$.